



Government of **Western Australia**  
Department of **Mines, Industry Regulation and Safety**

**REPORT 176**

# **TECTONO-MAGMATIC EVOLUTION OF THE NEOARCHEAN YALGOO DOME (YILGARN CRATON): DIAPIRISM IN A PRE-OROGENIC SETTING**

by

**I Zibra, M Peterneil<sup>1</sup>, M Schiller<sup>1</sup>, MTD Wingate, Y Lu and F Clos<sup>2</sup>**

1 Institute of Geoscience, University of Mainz, J.-J.-Becher-Weg 21, 55128 Mainz, Germany

2 School of Earth, Atmosphere and Environment, Monash University, Clayton, VIC 3800, Australia

**PERTH 2018**



**Geological Survey of  
Western Australia**

**MINISTER FOR MINES AND PETROLEUM**  
**Hon Bill Johnston MLA**

**DIRECTOR GENERAL, DEPARTMENT OF MINES, INDUSTRY REGULATION AND SAFETY**  
**David Smith**

**EXECUTIVE DIRECTOR, GEOSCIENCE AND RESOURCE STRATEGY**  
**Jeff Haworth**

#### **REFERENCE**

**The recommended reference for this publication is:**

Zibra, I, Peternell, M, Schiller, M, Wingate, MTD, Lu, Y and Clos, F 2017, Tectono-magmatic evolution of the Neoproterozoic Yalgoo dome (Yilgarn Craton): diapirism in a pre-orogenic setting: Geological Survey of Western Australia, Report 176, 43p.

ISBN 978-1-74168-771-2 (PDF); 978-1-74168-799-6 (print)



A catalogue record for this  
book is available from the  
National Library of Australia

Grid references in this publication refer to the Geocentric Datum of Australia 1994 (GDA94). Locations mentioned in the text are referenced using Map Grid Australia (MGA) coordinates, Zone 50. All locations are quoted to at least the nearest 100 m.

U–Pb measurements were conducted using the SHRIMP II ion microprobes at the John de Laeter Centre, Curtin University, with the financial support of the Australian Research Council and Auscope NCRIS.



#### **Disclaimer**

This product was produced using information from various sources. The Department of Mines, Industry Regulation and Safety (DMIRS) and the State cannot guarantee the accuracy, currency or completeness of the information. Neither the department nor the State of Western Australia nor any employee or agent of the department shall be responsible or liable for any loss, damage or injury arising from the use of or reliance on any information, data or advice (including incomplete, out of date, incorrect, inaccurate or misleading information, data or advice) expressed or implied in, or coming from, this publication or incorporated into it by reference, by any person whatsoever.

#### **Published 2018 by the Geological Survey of Western Australia**

This Report is published in digital format (PDF) and is available online at <[www.dmp.wa.gov.au/GSWApublications](http://www.dmp.wa.gov.au/GSWApublications)>.



© State of Western Australia (Department of Mines, Industry Regulation and Safety) 2018

With the exception of the Western Australian Coat of Arms and other logos, and where otherwise noted, these data are provided under a Creative Commons Attribution 4.0 International Licence. (<http://creativecommons.org/licenses/by/4.0/legalcode>)

#### **Further details of geological publications and maps produced by the Geological Survey of Western Australia are available from:**

Information Centre  
Department of Mines, Industry Regulation and Safety  
100 Plain Street  
EAST PERTH WESTERN AUSTRALIA 6004  
Telephone: +61 8 9222 3459 Facsimile: +61 8 9222 3444  
[www.dmp.wa.gov.au/GSWApublications](http://www.dmp.wa.gov.au/GSWApublications)

**Cover photograph:** View of the Yalgoo dome from the Edamurta Range, looking southeast. Rock cliffs in the foreground include weathering-resistant, silicified metasediments that are part of the greenstone sequence enveloping the Yalgoo dome.

# Contents

Abstract .....	1
Introduction .....	1
Geological setting .....	2
Lithostructural domains in the Yalgoo dome .....	4
The Kynea Tonalite .....	4
Granitic domain .....	9
Orthogneiss domain .....	9
The greenstones domain .....	9
The unconformity in the greenstone sequence .....	10
Superposed structures in the greenstone cover .....	14
Geometry of the main structural elements in the greenstone cover .....	14
The Yalgoo dome area: summary of geometry and kinematics .....	16
The dome-forming fabric .....	16
Outline of finite strain distribution .....	18
Kynea Tonalite .....	18
Badja decollement .....	18
Outline of the structures flanking the Yalgoo dome .....	19
Regional tectonic fabric .....	19
Microstructures .....	24
Kynea Tonalite and the granitic domain .....	24
Orthogneiss domain and greenstone domain .....	25
Main gneissic fabric .....	25
Relics of high-temperature microfabric .....	25
The Mt Mulgine dome and the regional tectonic fabric .....	25
Quartz Crystallographic Preferred Orientation (CPO) .....	28
Geochronology .....	28
Analytical methods .....	28
Geochronology results .....	28
GSWA 209689: metatonalite .....	28
GSWA 214324: metamonzogranite dyke .....	29
GSWA 214315: metamonzogranite dyke .....	29
GSWA 155858: metamonzogranite .....	29
GSWA 214101: monzogranite gneiss .....	29
GSWA 214138: granodiorite gneiss .....	29
GSWA 214139: monzogranite gneiss .....	38
GSWA 211101: volcaniclastic metasiltstone .....	38
Discussion and conclusion .....	38
Caveats and future studies .....	41
Acknowledgements .....	41
References .....	41

# Figures

1. Simplified geological map of the western portion of the Yilgarn Craton .....	3
2. Geological map of the study area, centred on the Yalgoo dome .....	4
3. Geological map with subdivision into main lithostructural domains of the Yalgoo dome .....	5
4. Comparison between two generations of geological maps centred on the Kynea Tonalite .....	6, 7
5. Main outcrop-scale structures in the Kynea Tonalite .....	8, 9
6. Primary magmatic features in Group 2 granites .....	10
7. Tectonic foliation in orthogneiss along the Badja decollement .....	11
8. Spatial distribution and chief outcrop-scale features of the unconformity preserved within the greenstone cover .....	12, 13
9. Superposed structures in the greenstone cover .....	15, 16
10. Equal-angle projection plots for each structural domain identified within the greenstone cover .....	17
11. Simplified geological map showing distribution of L>S to L tectonites .....	18
12. Geological map and three-dimensional sketch of the Gnows Nest keel .....	20, 21
13. East-trending gneissic foliation in the Cagacaroo Syenogranite .....	22
14. The regional tectonic fabric .....	23
15. North-trending retrograde shear zones in areas of well-developed regional tectonic fabric .....	24
16. Typical microstructure of S <sub>1-2</sub> from tonalite gneiss (Kynea Tonalite) and from the Orthogneiss Domain .....	26
17. Relics of high-temperature microfabric preserved in S <sub>G</sub> .....	27
18. Typical microstructures from the regional tectonic fabric (S <sub>R</sub> ) .....	27

19.	Simplified sketch map of the study area showing location of the samples selected for quartz CPO investigation .....	30, 31
20.	U–Pb analytical data for zircons from Yalgoo dome samples .....	37
21.	Probability density diagram and histogram for sample 211101 .....	40

## Tables

1.	Ion microprobe analytical results for zircons from geochronology samples .....	32
2.	Geochronology samples and results .....	36



# TECTONO-MAGMATIC EVOLUTION OF THE NEOARCHEAN YALGOO DOME (YILGARN CRATON): DIAPIRISM IN A PRE-OROGENIC SETTING

by

I Zibra, M Peternell<sup>1</sup>, M Schiller<sup>1</sup>, MTD Wingate, Y Lu and F Clos<sup>2</sup>

## Abstract

Gneiss domes occur in any orogenic and anorogenic domain of the continental crust, from Precambrian cratons to present-day active orogens. They commonly contain a core of granitic rocks and/or high-grade metamorphic rocks, overlain by a mantle of lower-grade rocks. Evolutionary models of many gneiss domes are controversial.

We use new structural and geochronological data to constrain the tectono-magmatic evolution of the Yalgoo dome in the Yilgarn Craton of Western Australia. The granite–migmatite core of the dome shows an overall domal foliation pattern, associated with radial and outwards-plunging lineations. A high-strain zone with top-outwards sense of shear (the Badja decollement) occurs along the granite–greenstone boundary. The greenstone sequence contains an angular unconformity that likely developed during doming.

We show that doming, associated with outward flow of supracrustal material, was accompanied by the emplacement of large volumes of granitic magma at 2760–2750 Ma. The dome-scale finite strain pattern resulted from diapiric granite emplacement into the greenstone cover, with negligible background regional stress. Granitic plutons flanking the Yalgoo dome show a similar, first-order structural architecture. The dome-forming fabric is locally overprinted by a discordant, north-trending foliation caused by folding that likely developed at c. 2700 Ma, during the Neoarchean Yilgarn orogeny.

**KEYWORDS:** geochronology, microstructures, preferred orientation, structural geology, tectonics, quartz crystallographic

## Introduction

Gneiss domes and gneiss dome systems (Yin, 2004) are striking geological features and occur in a variety of geological settings within the continental crust, from Precambrian cratons to present-day active orogens. Gneiss domes play a major role in lithosphere dynamics because they allow vertical transfer of heat and material towards upper crustal levels, thus contributing to the stabilization of the continental crust (Whitney et al., 2004). Gneiss domes offer a wide variety of rock types and structures, but have some general first-order features common to most — if not all — gneiss domes. These include: i) domal pattern of foliation and/or lithological boundaries; ii) dome core made of granites and/or high-grade metamorphic rocks, commonly migmatitic; and iii) a mantle of metasedimentary, lower-grade rocks wrapping around the dome core. Even though the overall, first-order geometry of gneiss domes is relatively simple, the literature offers a wide variety of mechanisms for dome

formation, and evolutionary models of many gneiss domes are still controversial. Early, classic studies emphasized the role of Rayleigh–Taylor instabilities and diapirism (Ramsay, 1967; Ramberg, 1972) and therefore stressed the role of lower-crustal viscous flow in shaping upper crustal geometries and kinematics. These models were also tested from a conceptual viewpoint (Cruden, 1988; Weinberg and Podladchikov, 1995).

More recent contributions focused on the role of tectonic activity in the strong upper crust in triggering and/or controlling the pattern of lower-crustal flow. In various tectonic settings, the development of gneiss domes has been related to orthogonal superposed folding events (Ramsay, 1967), duplex development in thrust systems, decollement faults in extensional environments, forming metamorphic core complexes, and fold culminations in strike-slip systems. Different mechanisms may have cooperated/competed in variable amounts and/or at different stages of dome formation, so that a superficially simple domal architecture may in fact represent the end product of a complex tectono-magmatic and metamorphic evolution. In principle, different processes of dome formation should be associated with typical dome-scale finite strain patterns and so structural analysis represents a fundamental tool for unravelling their evolution.

---

<sup>1</sup> Institute of Geoscience, University of Mainz, J.-J.-Becher-Weg 21, 55128 Mainz, Germany

<sup>2</sup> School of Earth, Atmosphere and Environment, Monash University, Clayton, VIC 3800, Australia

However, the high-grade, often melt-present metamorphic conditions associated with dome formation commonly induce pervasive reworking and recrystallization of early structures, so that the structural memory of exposed domes is often limited, and a multidisciplinary approach is required for a better understanding of the processes involved in dome formation.

With this contribution, we are concerned with the evolution of the Yalgoo dome, from the Archean Yilgarn Craton, Western Australia. In 2012 the Geological Survey of Western Australia (GSWA) started a new mapping project in the Yalgoo area, in collaboration with the China Geological Survey. Together with mapping, GSWA has been conducting detailed mesostructural and microstructural analysis on the Yalgoo dome, in collaboration with Mainz (Germany), Macquarie and Monash Universities. Honours and Masters students focused their work on particular aspects of the tectono-metamorphic evolution of the Yalgoo dome, such as the structural evolution of the migmatitic core (Fenwick, 2014), on the occurrence of L-tectonites along some portions of the sheared granite–greenstones boundary (Tomkins, 2015), and with detailed mapping of different structural domains (Caudery, 2014).

The Yalgoo dome developed in a typical granite–greenstones terrain, and it has been previously interpreted as the result of superposed folds (Myers and Watkins, 1985). In contrast, the possible role of diapirism in creating the observed structural pattern of the Yalgoo area was emphasized by Foley (1997).

Here we use our new mesostructural and microstructural data, in conjunction with new geochemical and geochronology datasets, to reassess the tectono-magmatic evolution of the Yalgoo dome. We show that the previous model overlooked the role of magmatism, and that a model that invokes upright superposed folds is inadequate because it contradicts several first-order structural and kinematic constraints, from thin section to dome scale. We show that the patterns of foliation, lineation and folds that developed at various stages in both the granite–migmatite core and in the greenstone cover, and the kinematics of the main high-strain zones, are best explained by diapiric, vertical ascent and emplacement of high-grade, partially molten rocks into the supracrustal cover sequence. Moreover, geochemical and geochronological data suggest that dome construction occurred through discrete events within a 300 Ma time span, and that uplift of the dome core can be spatially and temporally related to angular unconformities in the greenstone cover.

## Geological setting

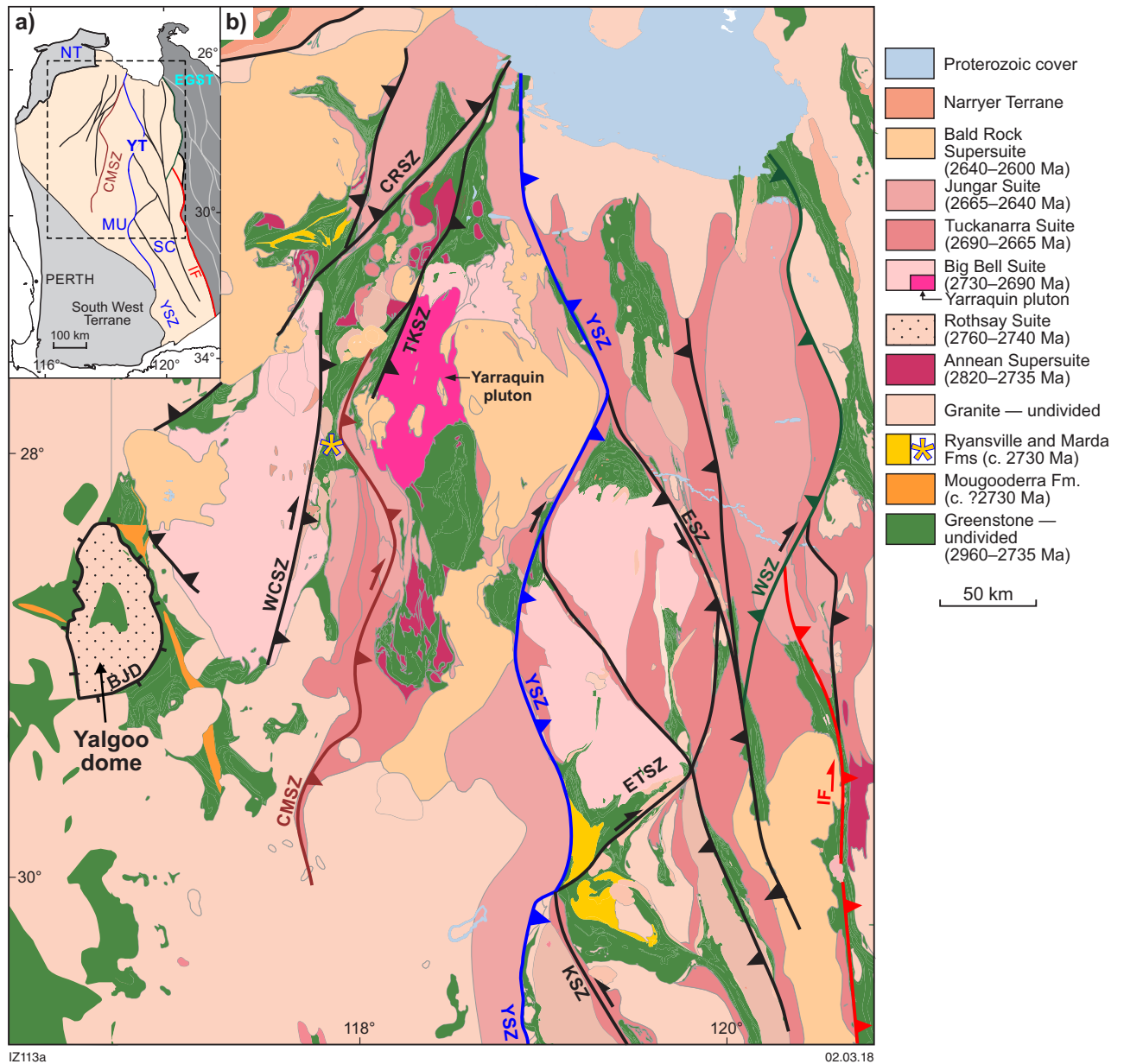
The Youanmi Terrane forms most of the western half of the Archean Yilgarn Craton (inset in Fig. 1; terrane nomenclature after Cassidy, 2006) and includes 2960–2720 Ma greenstone successions intruded by 2815–2600 Ma granitic rocks (Van Kranendonk et al., 2013). The 2960–2750 Ma greenstone stratigraphy mainly includes mafic–ultramafic rocks associated with banded iron-formation (Van Kranendonk et al., 2013). This

sequence is therefore indicative of greenstone development in a deep-marine environment, in a time span that was likely dominated by lithospheric extension (as suggested by the voluminous mantle-derived magmatism), alternating with periods of tectonic quiescence. In contrast, the 2730–2710 Ma succession consists of clastic sedimentary rocks interlayered with felsic volcanic rocks. This younger succession rests above a regional-scale unconformity that reflects a period of uplift and erosion of the older greenstone succession (Chen et al., 2003; Morris et al., 2007). The development of the c. 2730 Ma regional unconformity likely reflects the onset of the Neoproterozoic orogeny in the Yilgarn Craton (Zibra et al., 2017).

Seismic and field data indicate that the whole craton includes a series of east-dipping, crustal-scale shear zones (Wilde et al., 1996; Drummond et al., 2000; Zibra et al., 2014a), juxtaposing terranes with contrasting stratigraphy (Wyche et al., 2012). At least some of these large-scale structures represent long-lived, transpressional shear zones that were active during the emplacement of syntectonic plutons in the 2730–2660 Ma time span (Zibra et al., 2014b). In map view (Fig. 1), these shear zones are broadly north trending and can be followed for hundreds of kilometres along strike (Vearncombe, 1998). Greenstone belts flanking the shear zones typically form north-trending, high-strain belts, subparallel to the shear zone trend.

The Yalgoo dome is located in the western portion of the Youanmi Terrane of the Yilgarn Craton (Fig. 1). In the Yalgoo area, greenstone successions include 2960–2945 Ma felsic and intermediate volcanic, and felsic volcanoclastic and chemical sedimentary rocks, overlain by c. 2810 Ma mafic and felsic volcanic rocks interlayered with banded iron-formation (Van Kranendonk et al., 2013). These sequences are overlain by the 2800–2760 Ma, approximately 8 km-thick Yalgoo Formation, which mainly consists of pyroxene spinifex-textured basalt interlayered with olivine spinifex-textured komatiite (Ivanic et al., 2015). The volcano-sedimentary pile is intruded by thick, layered mafic–ultramafic intrusions of inferred c. 2790 Ma crystallization age, collectively assigned to the Warriedar Suite (Ivanic et al., 2015). All of the greenstones mentioned above are unconformably overlain by the 2–3 km-thick Mougooderra Formation (Fig. 2), a siliciclastic sequence of as-yet unknown age (Watkins and Hickman, 1990). The core of the dome includes c. 2950 Ma tonalite gneiss that has intruded banded iron-formation and amphibolite (Wiedenbeck and Watkins, 1993). Later granitic intrusion and deformation make it difficult to estimate the total thickness of the greenstones in the Yalgoo area; however, the preserved thickness of about 8 km for the Yalgoo Formation (Ivanic et al., 2015) represents a minimum thickness of the greenstone pile.

There is no field or geophysical evidence in the Yalgoo region for the occurrence of the large-scale transpressional shear zones that characterize most of the Yilgarn Craton. Instead, the granite–greenstone lithological boundaries define dome-and-keel patterns that closely resemble the granite–greenstone pattern of the east Pilbara Terrane (Van Kranendonk et al., 2004).



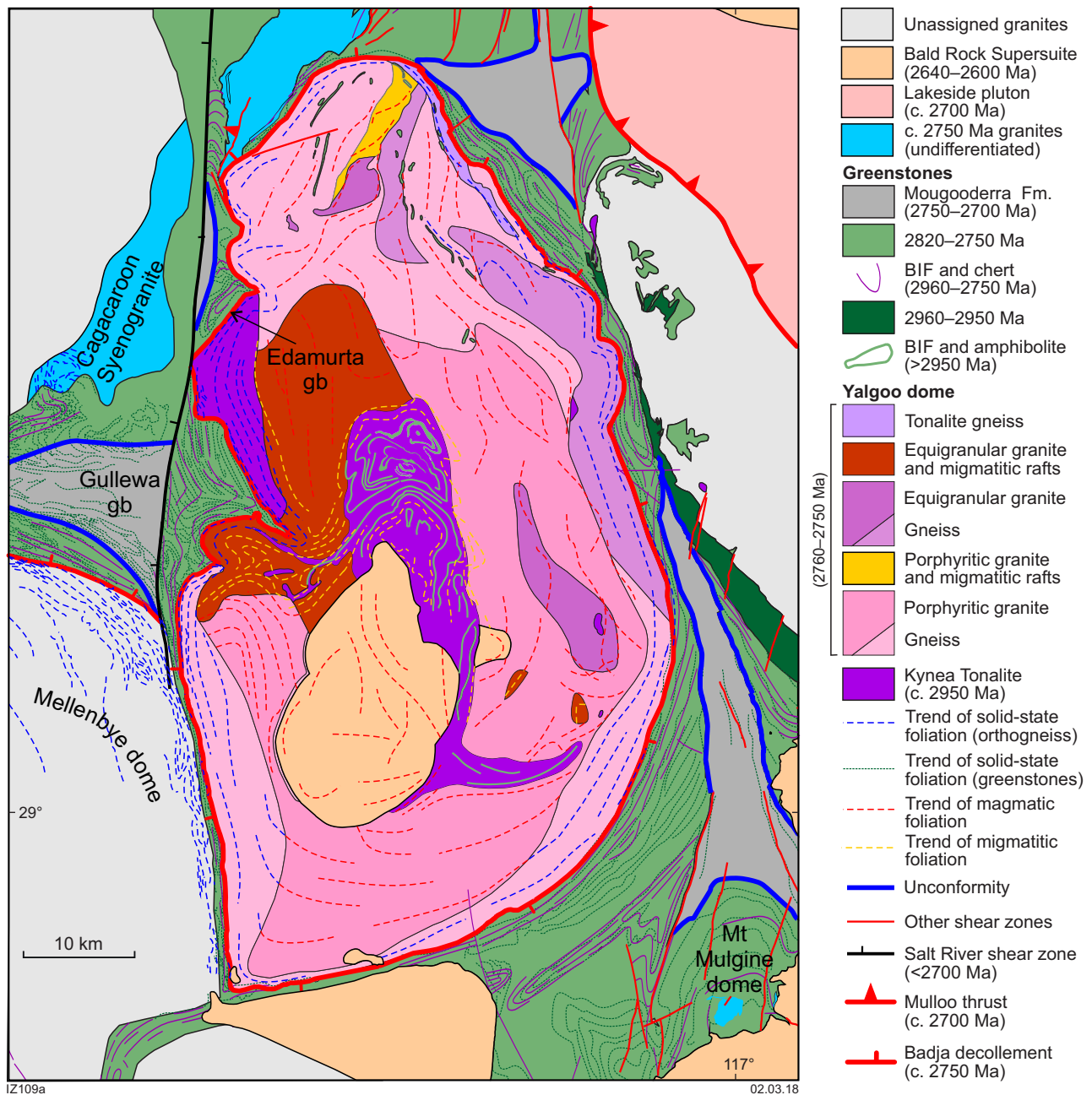


**Figure 2.** Geological map of the study area, centred on the Yalgoo dome, showing the different types of granitic rocks within the dome and the keel pattern defined by the geometry and foliations in the greenstone sequences

## Lithostructural domains in the Yalgoo dome

The Yalgoo dome can be subdivided into four distinct domains (Fig. 3) based on lithological associations and style of deformation. In the core of the dome, the Kynea Tonalite consists of 2960–2950 Ma layered tonalitic gneiss containing older slivers of banded iron-formation and amphibolites. The Kynea Tonalite is surrounded by a second domain with several types of granitic rocks showing magmatic fabric. The third domain occurs in the proximity of the granite–greenstones boundaries, and contains strongly deformed granitic gneiss similar in composition to the undeformed granites of the second domain. The fourth domain includes the greenstone units that form the cover of

the granite–migmatite dome. In the following subsections, we detail the main meso- and microstructural features of each domain.

## The Kynea Tonalite

The Kynea Tonalite includes metatonalite intruded into older greenstones, represented by banded iron-formation and amphibolites. The magmatic crystallization of the tonalite was dated at  $2919 \pm 12$  Ma (Wiedenbeck and Watkins, 1993). More recent geochronology investigations provided crystallization ages of  $2956 \pm 58$  Ma (Wingate et al., 2015) and  $2960 \pm 10$  Ma (Caudery, 2014). In map view, the tonalite–greenstone lithological boundaries show a complex geometry that superficially resemble patterns



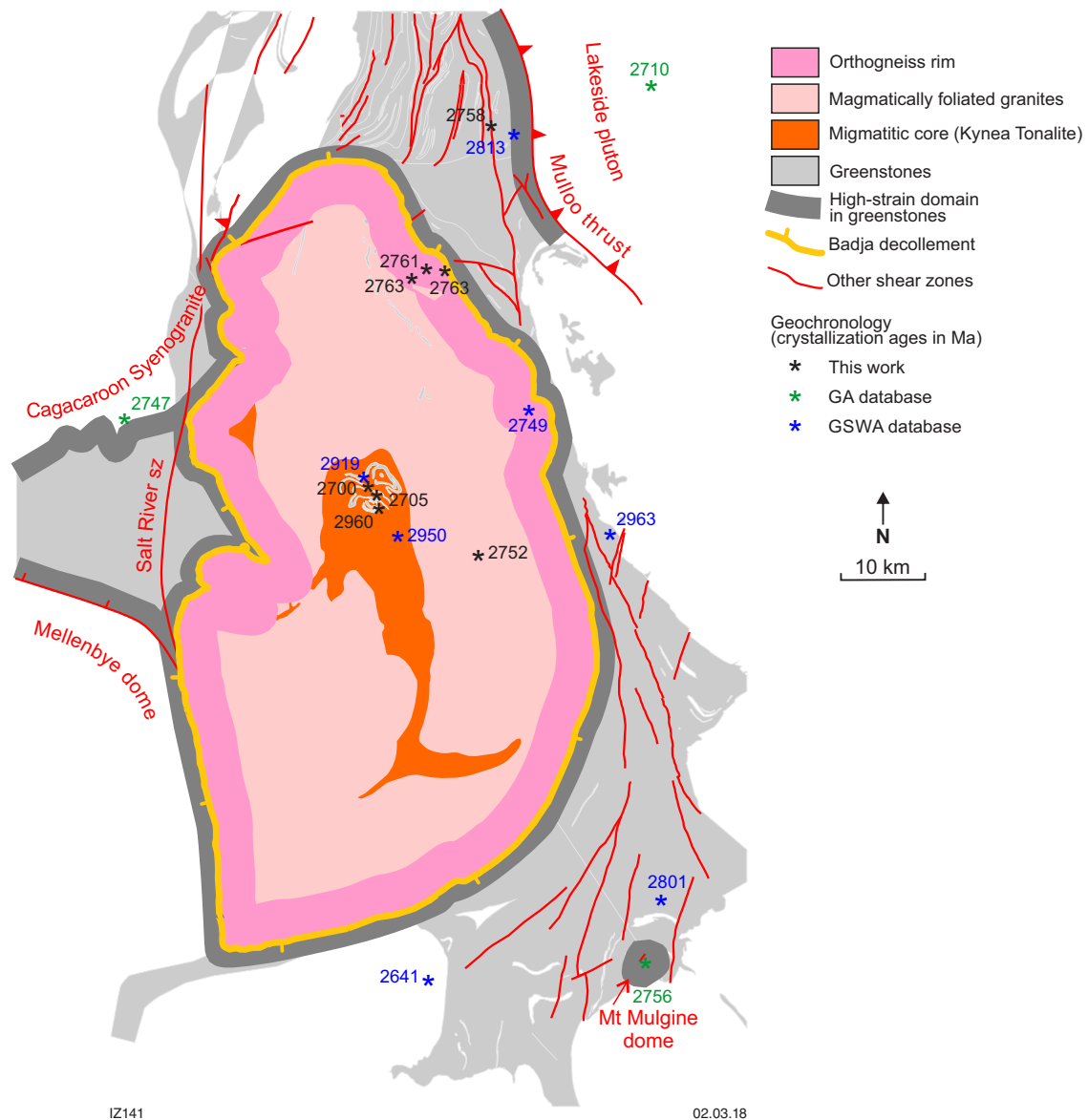


**Figure 3.** Simplified geological sketch map of the study area, showing the subdivision into main lithostructural domains. The map also shows the location of the geochronology samples analysed in this work and other samples from the available literature

generated by superposed folding events (Ramsay and Huber, 1987). Myers and Watkins (1985) proposed that such map pattern — and also the geometry of the whole Yalgoo dome — resulted from north-trending upright folds, superimposed on east-trending upright folds (Fig. 4a). The detailed mapping conducted during this work (Fig. 4b) demonstrates that such interpretation is at odds with the available structural data, as we examine more widely in the discussion section.

Fenwick (2014) identified four distinct generations of fabrics within the Kynea Tonalite. The  $S_{1-2}$  composite foliation is the most penetrative fabric and is invariably parallel to tonalite–greenstone contacts (Fig. 4b).  $S_{1-2}$  shows variable orientation but it is always steeply dipping (plot [i] in Fig. 4c).  $S_{1-2}$  bears an  $L_1$  stretching and mineral lineation, highlighted by elongated quartz and feldspar

aggregates and amphibole porphyroblasts, in metatonalite and amphibolite, respectively.  $L_1$  is subvertical in both metatonalite and host greenstones, and subparallel to the axes of mesoscale folds ([ii] in Fig. 4c). On subvertical exposures, perpendicular to  $S_{1-2}$  and parallel to  $L_1$  (Fig. 5a, XZ sections of the finite strain ellipsoid), mantled porphyroclasts, S–C and C' subfabrics provide core-up shear sense. Observations on horizontal exposures (YZ sections of the finite strain ellipsoid) indicate that, at least at the current exposure level, the development of  $S_{1-2}$  was associated with a second component of stretching in the horizontal plane (Fig. 5b). Along the tonalite–greenstone interface, boudinaging of the more competent amphibolite layers was accompanied by in situ partial melting of amphibolite (Fig. 5b), indicating that the  $D_{1-2}$  phase occurred under migmatitic conditions.

$D_{1-2}$  pervasive fabric is post-dated by a north-trending, spaced axial planar foliation ( $S_3$ , plot [iii] in Fig. 4c), manifested by thin, subvertical leucosomes developed in both metatonalite and amphibolite (Fig. 5c,d).  $S_3$  is axial planar to outcrop- and map-scale, subvertical  $F_3$  folds (Fig. 5c), and overprints circular (in map view) structures at both outcrop and map scales (Fig. 5e). Given its delicate nature,  $S_3$  is best visible in smooth, pavement-type outcrops (Fig. 5c,e), which generally do not offer three-dimensional exposures. Therefore, we were unable to collect a statistically valid dataset of  $L_3$  linear fabric. However, several lines of evidence, such as the subvertical attitude of  $F_3$  folds and the observation that higher finite strain seems to be recorded along subvertical exposures, suggest that  $L_3$  is steeply plunging. Field observations therefore indicate that the  $D_3$  event reflects an episode of east–west shortening (Fig. 5h) that occurred — as for the  $D_{1-2}$  event — under migmatitic conditions, and distorted and rotated pre-existing sheath folds (Fig. 5c,d).  $S_3$  is

in turn post-dated by a network of north-northwesterly trending, equigranular and porphyritic granite dykes, developed at a low angle from the northerly trending  $S_3$  (Figs 4b, 5f). Equigranular granite dykes commonly show a pronounced irregular and diffuse schlieren layering broadly subparallel to dyke boundaries, and contain decimetre-sized xenoliths of host tonalite gneiss (Fig. 5g). Most of these dykes were reactivated as shear zones, showing relatively narrow bands of a subvertical gneissic to mylonitic foliation ( $S_4$ ) that is subparallel to dyke boundaries and not visible in host rocks, and they contain a steeply plunging stretching lineation ( $L_4$ ).  $S_4$  is either steeply east- or steeply west-dipping (Fig. 4c). In both cases, kinematic indicators exposed along XZ sections of the finite strain ellipsoid point to top-to-west kinematics for  $D_4$  shear zones. Therefore, by analogy with the  $D_3$  event, the  $D_4$  event reflects a deformation episode associated with bulk east–west shortening.

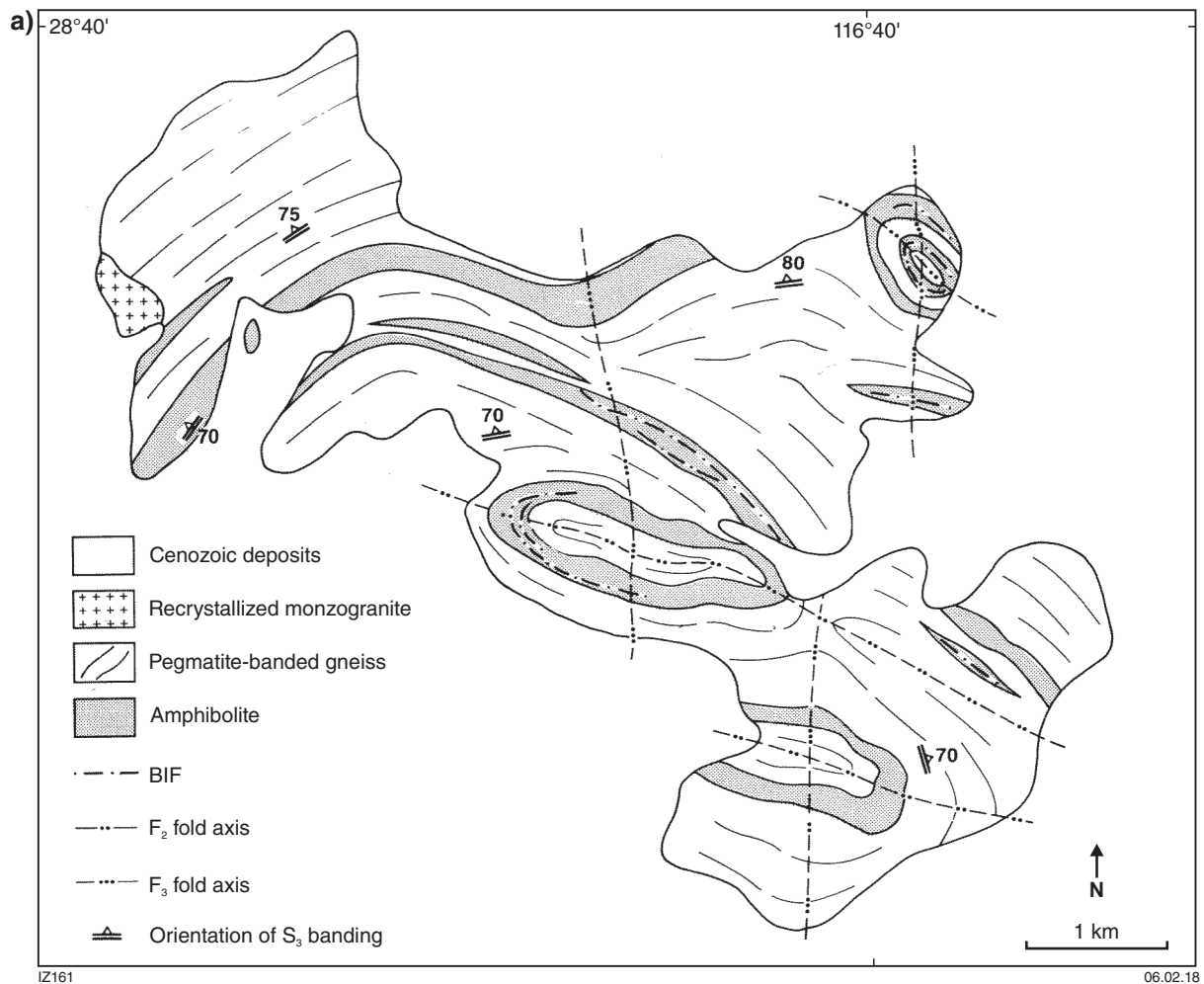
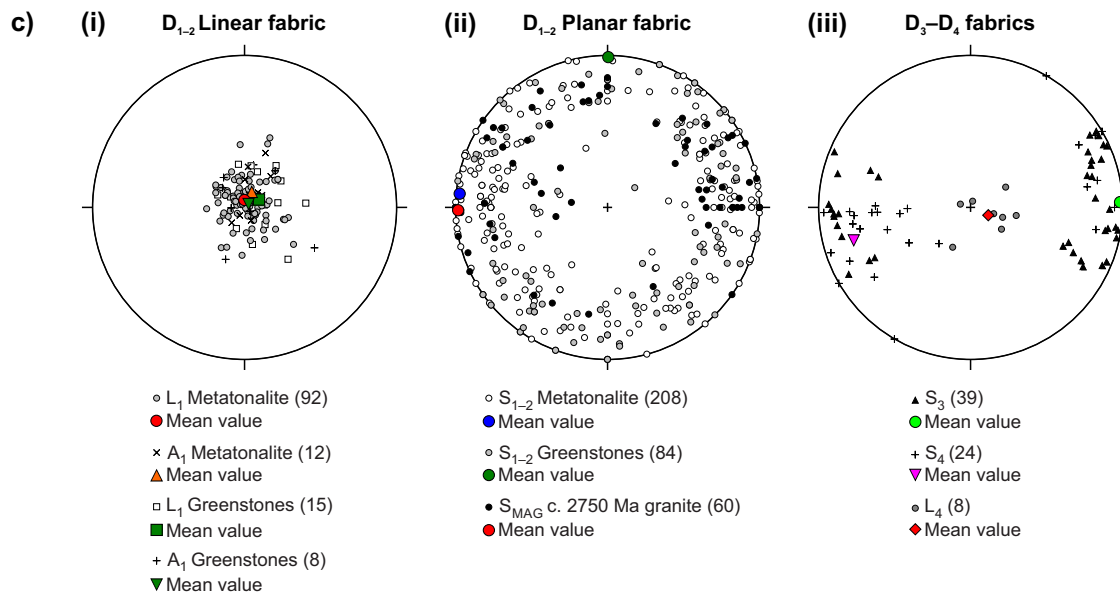
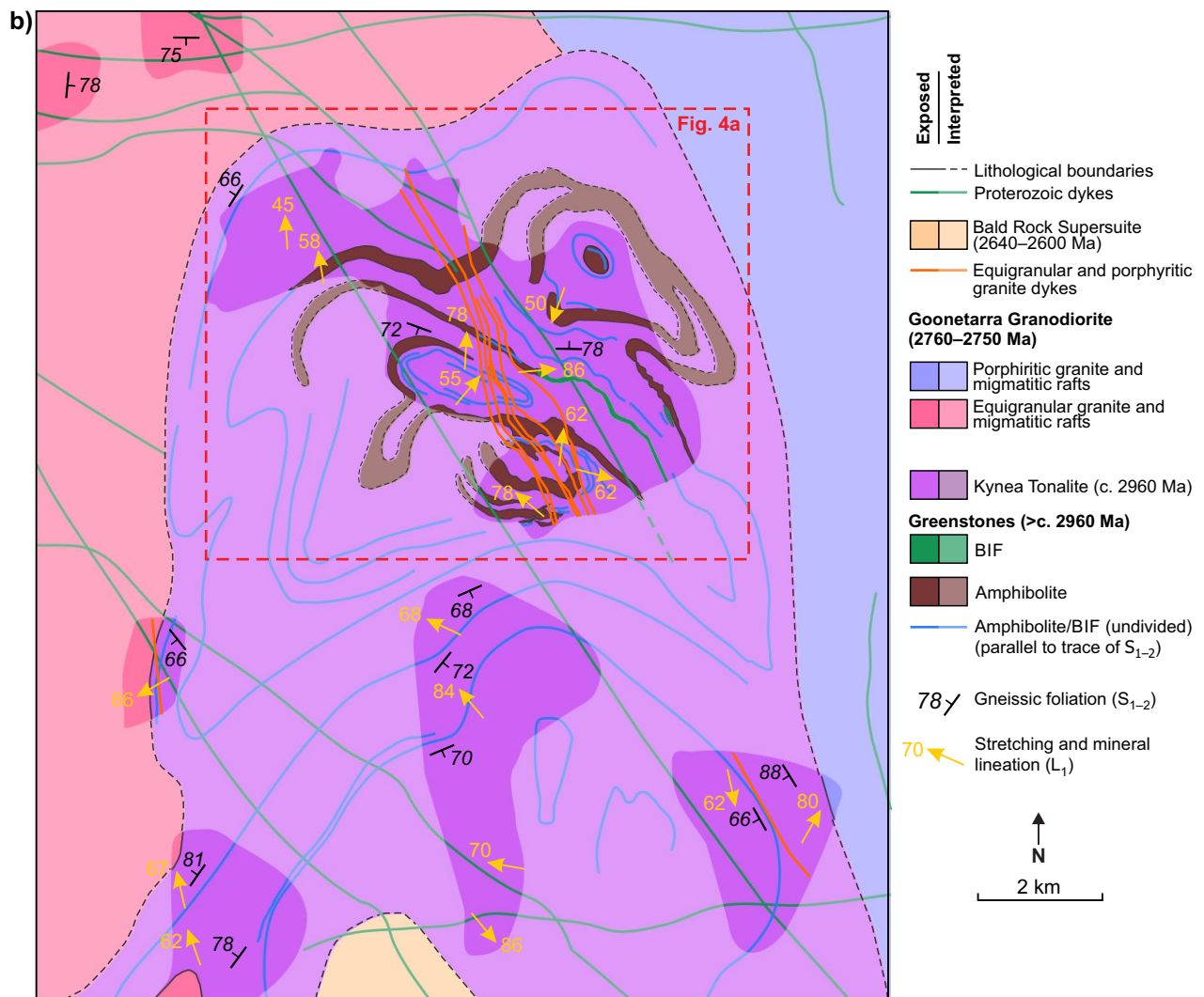


**Figure 4.** Comparison between two generations of geological maps centred on the Kynea Tonalite: a) geological map from Myers and Watkins, 1985; b) geological map produced during this study; c) equal-angle projection plots (lower hemisphere) of main planar and linear structures of the Kynea Tonalite. Number of measurements is reported in brackets



IZ142

27.02.18

Figure 4. continued



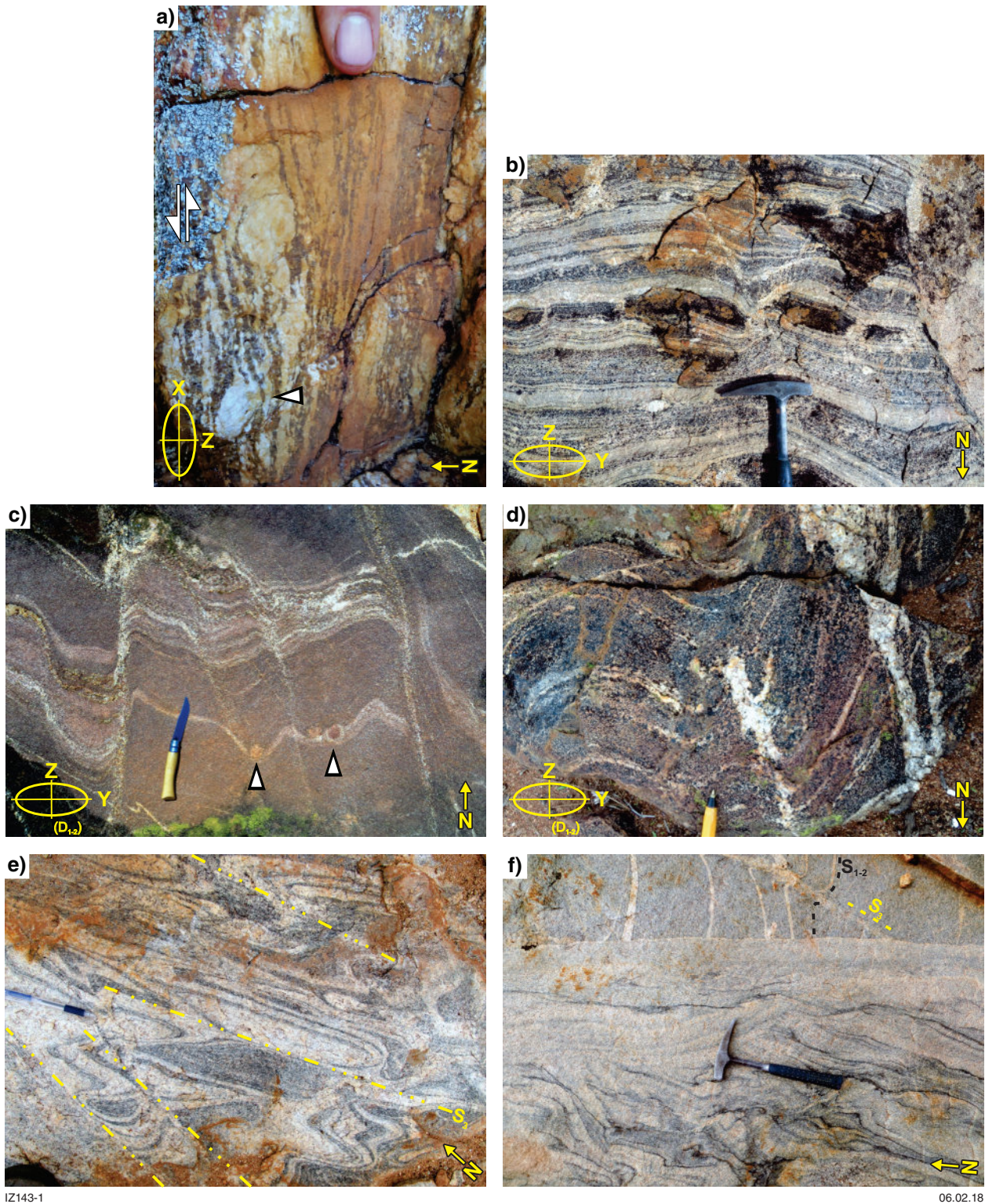


**Figure 5.** Main outcrop-scale structures in the Kynea Tonalite. All field photographs are from subhorizontal exposures, unless otherwise indicated: a) subvertical exposure of coarse-grained, gneissic leucotonalite. Sigma-type mantled plagioclase porphyroclasts indicate south-side-up (i.e. Kynea Tonalite-up) kinematics; b) contact zone between amphibolite slivers and host tonalite gneiss. The more competent, amphibole-rich layers show boudinage perpendicular to the subvertical stretching lineation. Leucosome-filled boudin necks suggest migmatitic conditions during the development of the main  $S_{1-2}$  foliation; c) east-trending  $S_{1-2}$  foliation post-dated by north-trending  $S_3$ . Note that  $S_3$  surfaces are marked by leucosomes that show diffuse boundaries against host tonalite gneiss, suggesting in situ melting. Arrowheads point to clast-in-vein structure, with large K-feldspar porphyroclasts aligned along a  $D_{1-2}$  leucocratic layer, which likely represents a sheared pegmatite; d) amphibolite showing  $S_{1-2}$ - $S_3$  relationships in a north-trending  $F_3$  fold hinge; e)  $D_{1-2}$  isoclinal to sheath folds post-dated by  $D_3$  leucosomes; f) north-trending schlieren granite dyke post-dating  $S_3$  in host tonalite gneiss; g) detail from the dyke in (f), showing decimetre-sized clasts of layered tonalite gneiss with diffuse to sharp boundaries against host schlieren granite; h) folded amphibolite boudin within host tonalite gneiss. Leucosome-filled boudins likely developed during  $D_{1-2}$ , and were then shortened during the development of the north-trending  $S_3$ . Compare with (b)



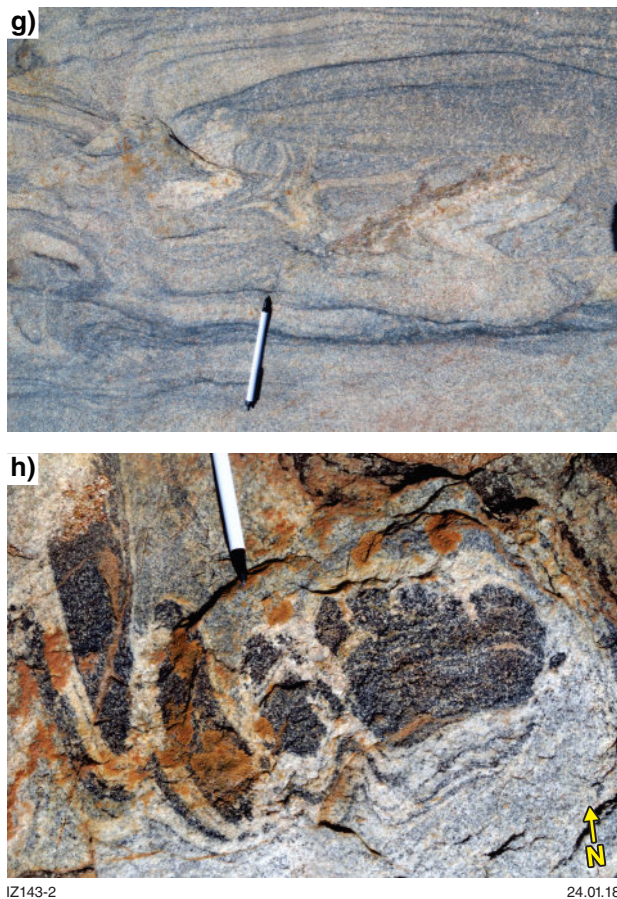


Figure 5. continued

## Granitic domain

The Kynea Tonalite is surrounded by granitic rocks (Fig. 2) that invariably retain their primary magmatic fabric and lack any significant, solid-state fabric. Magmatic foliation is highlighted by aligned euhedral feldspars and biotite flakes (Fig. 6a) that are subparallel to schlieren layering, and preferential alignment of xenoliths. Two different groups of granitic rocks are identified, based on main lithological associations, field relationships and geochemistry. Group 1 includes equigranular to porphyritic monzogranite and granodiorite that commonly contain metre-scale xenoliths of the Kynea Tonalite. Detailed mapping by Caudery (2014) provides an example of the complex geometric relationships between hectometre-scale xenoliths of the Kynea Tonalite and host granitic rocks. The magmatic foliation in these rocks shows variable orientation and a roughly concentric pattern subparallel to the contact with the Kynea Tonalite (Fig. 2; plot [ii] in Fig. 4c). These granitic rocks are chemically classified as transitional TTG (Clos et al., 2016) and have magmatic crystallization ages between 2760 and 2750 Ma (Fig. 3; see geochronology section).

Group 2 granitic rocks are distinct, peculiar, melanocratic microporphyritic granite containing large K-feldspar phenocrysts (up to 5 cm in size), embedded in a fine-grained, biotite-rich matrix (Fig. 6b). This microporphyritic

granite occurs as large dykes and masses within the coarse-grained equigranular to porphyritic, leucocratic monzogranites and granodiorites of Group 1. Group 2 rocks occur within a subcircular (in map view) pluton intruded into the southern margin of the Kynea Tonalite and Group 1 rocks (Fig. 2). A ~300 m-wide mylonitic belt, developed within Group 1 granitic rocks, is preserved along the western boundary of this younger pluton, and carries a gneissic foliation parallel to the pluton boundary (Fig. 2). Group 2 rocks are also geochemically distinct as they are classified as low-Ca granites or potassic granites (Clos et al., 2016; Champion and Sheraton, 1997; Wingate et al., 2014). They share their main chemical signature with the adjacent Seeligson Monzogranite (Fig. 3), which was dated at  $2626 \pm 6$  Ma (Wingate et al., 2014).

## Orthogneiss domain

Towards the contact with the greenstone cover, granitic rocks with magmatic fabrics are progressively replaced by orthogneiss developed at the expense of the porphyritic and equigranular rocks (Fig. 7a). Field, geochemical (Clos et al., 2016) and geochronological (section 8) data indicate that the gneissic rocks exposed along the dome margins represent the deformed equivalent of Group 1 granitic rocks exposed in the granitic domain. The gneissic foliation ( $S_G$ ) is marked by elongate quartz ribbons and biotite trails wrapping around rounded feldspar porphyroclasts (Fig. 7a,b). At the scale of the dome,  $S_G$  is subparallel to the granite–greenstone contact and dips away from the dome core, defining a broad domal structure (Fig. 7c).  $S_G$  bears a down-dip stretching lineation ( $L_G$ ), highlighted by quartz ribbons and feldspar–biotite aggregates. At the scale of the dome,  $L_G$  shows a radial orientation, that is, it consistently plunges outwards (Fig. 7c). On sections subparallel to  $L_G$  and perpendicular to  $S_G$  (i.e. close to XZ sections of the finite strain ellipsoid), kinematic indicators such as S–C and C' subfabrics and mantled feldspar porphyroclasts invariably indicate normal (i.e. greenstones-down) kinematics for the entire length of the granite–greenstone boundary (Fig. 7b). Within the orthogneiss domain, solid-state overprint progressively increases towards the granite–greenstone contact, which represents the zone of highest finite strain. We call this high-strain zone the Badja decollement.

## The greenstone domain

Along the hangingwall of the Badja decollement, the 2960–2800 Ma lower greenstone sequence is mainly represented by banded iron-formation, cherts and other sedimentary rocks, which are interlayered with mafic to ultramafic schists and gneiss. The lower greenstone sequence is unconformably overlain by the Mougooderra Formation (Watkins and Hickman, 1990). The sequences are deformed together and preserved as tight synclines. In this section, we first describe the nature of the unconformity, by outlining the salient sedimentary features exposed in three selected locations. The following section provides an outline of the structural evolution preserved in the whole greenstone cover.



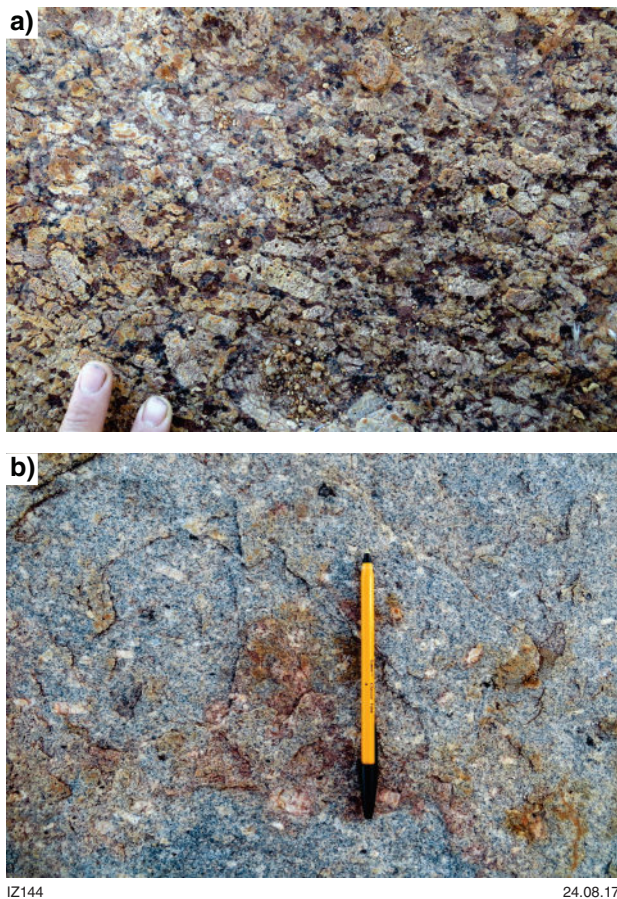


**Figure 6.** Primary magmatic features in Group 2 granites: **a)** magmatic foliation in porphyritic granite, highlighted by aligned, euhedral K-feldspar phenocrysts; **b)** magmatic foliation in microporphyritic granite. Euhedral K-feldspar phenocrysts are surrounded by a biotite-rich, fine-grained granitic matrix

## The unconformity in the greenstone sequence

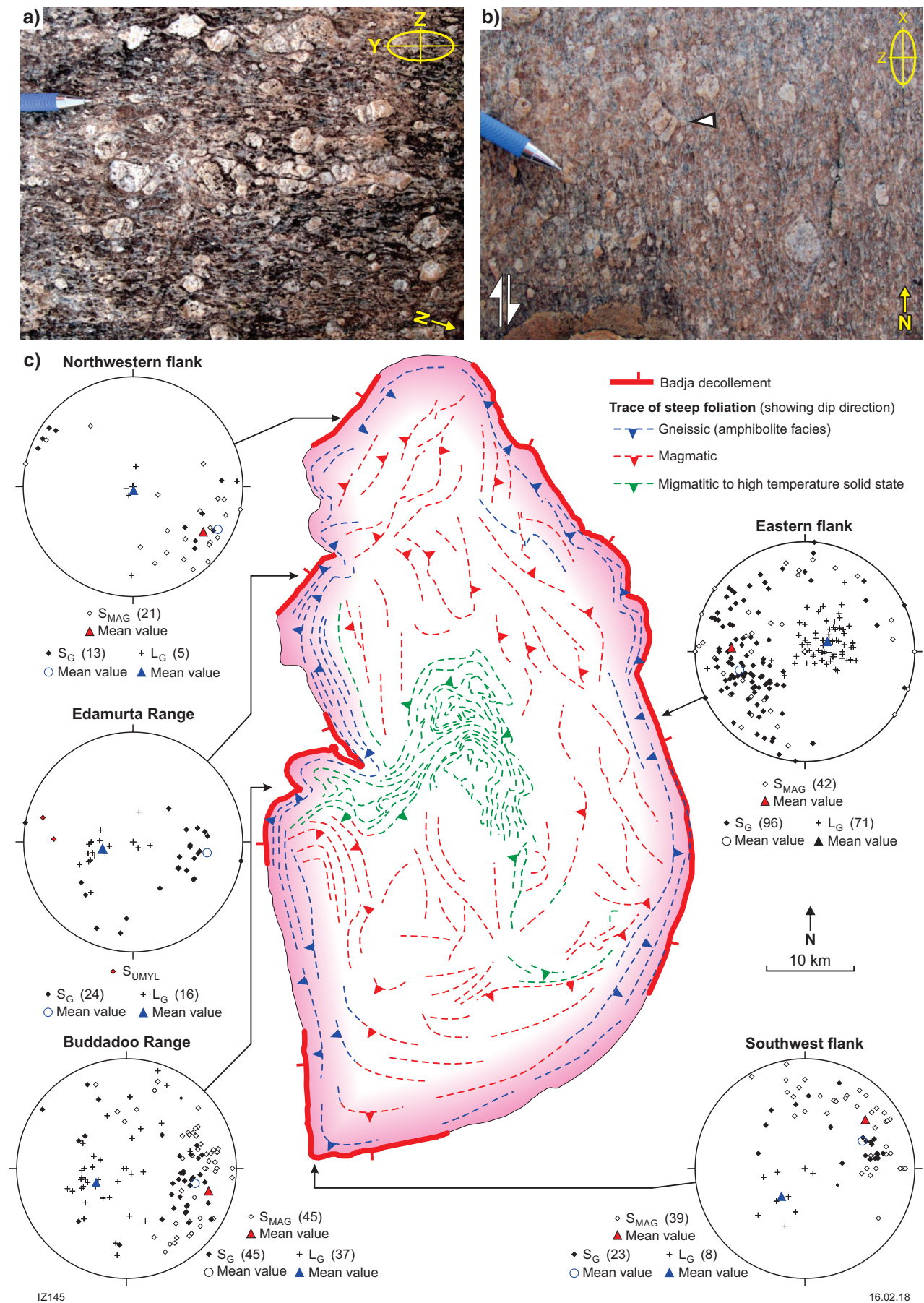
In the hangingwall of the Badja decollement, the 2960–2800 Ma greenstone sequence is unconformably overlain by an as-yet undated siliciclastic sequence represented by the Mougooderra Formation (Watkins and Hickman, 1990). This formation is up to 2000 m thick, with an overall fining-upwards sequence that includes a conglomeratic base, overlain by sandstone and shale. Overall, the sequence reflects an evolution from subaerial/shallow-marine deposition to deep-marine sedimentation (Watkins and Hickman, 1990). In the Yalgoo dome area, the Mougooderra Formation is exposed in four synclines, which are preserved along both the eastern and western flanks of the Yalgoo dome (Fig. 2). In this contribution, we are concerned with the lowermost, conglomeratic portion of this sequence, and we focus on three selected localities (Fig. 8a) to describe the main features of this unconformity. In the section preserved near Chulaar Hill (inset [1], Fig. 8a), the unconformity is exposed along the eastern limb of a steeply south-plunging, kilometre-scale syncline developed in the hangingwall of the Badja decollement. At this locality, therefore, both the unconformity and lithological contacts are subvertical to steeply east

dipping. Figure 8b illustrates the interpreted geometry of the unconformity. From east to west, this section exposes the transition from foliated metachert (I), to a cataclastic foliated metachert belonging to the Polelle Group (II), followed by a fining-upwards sedimentary sequence that includes a monogenic chert conglomerate (III and IV) gradually evolving into pebbly sandstone containing large chert clasts (V), followed by pebbly sandstone containing sporadic, smaller chert clasts (VI).

Along the western flank of the Yalgoo dome, in the Gullewa greenstone belt (inset [2], Fig. 8a), the Mougooderra Formation is preserved as a synformal keel, surrounded by older greenstone sequences dominated by mafic volcanic rocks interlayered with chert and banded iron-formation. The north–south section exposed near Brandy Hill shows the transition, within the Mougooderra Formation, from a foliated metachert to a monogenic chert conglomerate, in turn overlain by pebbly sandstone containing chert clasts. Volumetrically dominant sandstone layers fine upwards. This sedimentary sequence is therefore similar to the one observed at Chulaar Hill. At Brandy Hill, the sedimentary sequence fines upwards towards the north so that the northern portion of the Mougooderra Formation mainly includes siltstones and mudstones. In this area, the conglomeratic base of the Mougooderra Formation is approximately east trending, that is, subparallel to the northern margin of the undated Mellenbye dome (inset [2], Fig. 8a). The conglomeratic portion reaches its maximum thickness at its eastern end where it is ~500 m thick. Over the whole region, the conglomerate is distinctively clast supported and commonly contains little or no matrix (Fig. 8c), indicative of deposition in a high-energy sedimentary environment. Chert clasts are dominantly angular along the unconformity, while they become progressively more rounded and smaller up section, where the conglomerate grades into pebbly sandstones (Fig. 8d).

The third unconformity locality is along strike from the Chulaar Hill section (Fig. 8a). In the Mulloo Hill area, greenstones are exposed in the footwall of the Mulloo thrust, an amphibolite-facies shear zone that developed during the syntectonic emplacement of the Lakeside pluton at c. 2700 Ma (Zibra et al., 2014a). The greenstone sequence here is strongly deformed and shows a transition from foliated amphibolite to a peculiar conglomerate containing mainly amphibolite clasts, together with subordinate granite, granophyre and banded iron-formation clasts, embedded within an amphibole-rich matrix (Fig. 8e). The composition of the matrix gradually changes from amphibolitic in the east (i.e. the stratigraphic base of the conglomerate), to quartzofeldspathic towards the west.

**Figure 7.** (page 11) Tectonic foliation in orthogneiss along the Badja decollement: **a)** gneissic foliation developed at the expense of porphyritic granite. View at high angle from the steeply plunging stretching lineation; **b)** subvertical exposure of porphyritic gneiss. Sigma-shaped K-feldspar porphyroclasts (arrowhead) indicate dome-up, normal kinematics; **c)** equal-angle projection plots (lower hemisphere) for each exposed domain of the Badja decollement. Number of measurements is reported in brackets.  $S_G$  defines an overall domal geometry, while  $L_G$  consistently show a radial, outwards-plunging arrangement. The thick red lines along the Badja decollement indicate the area from which the structural data are plotted in each diagram





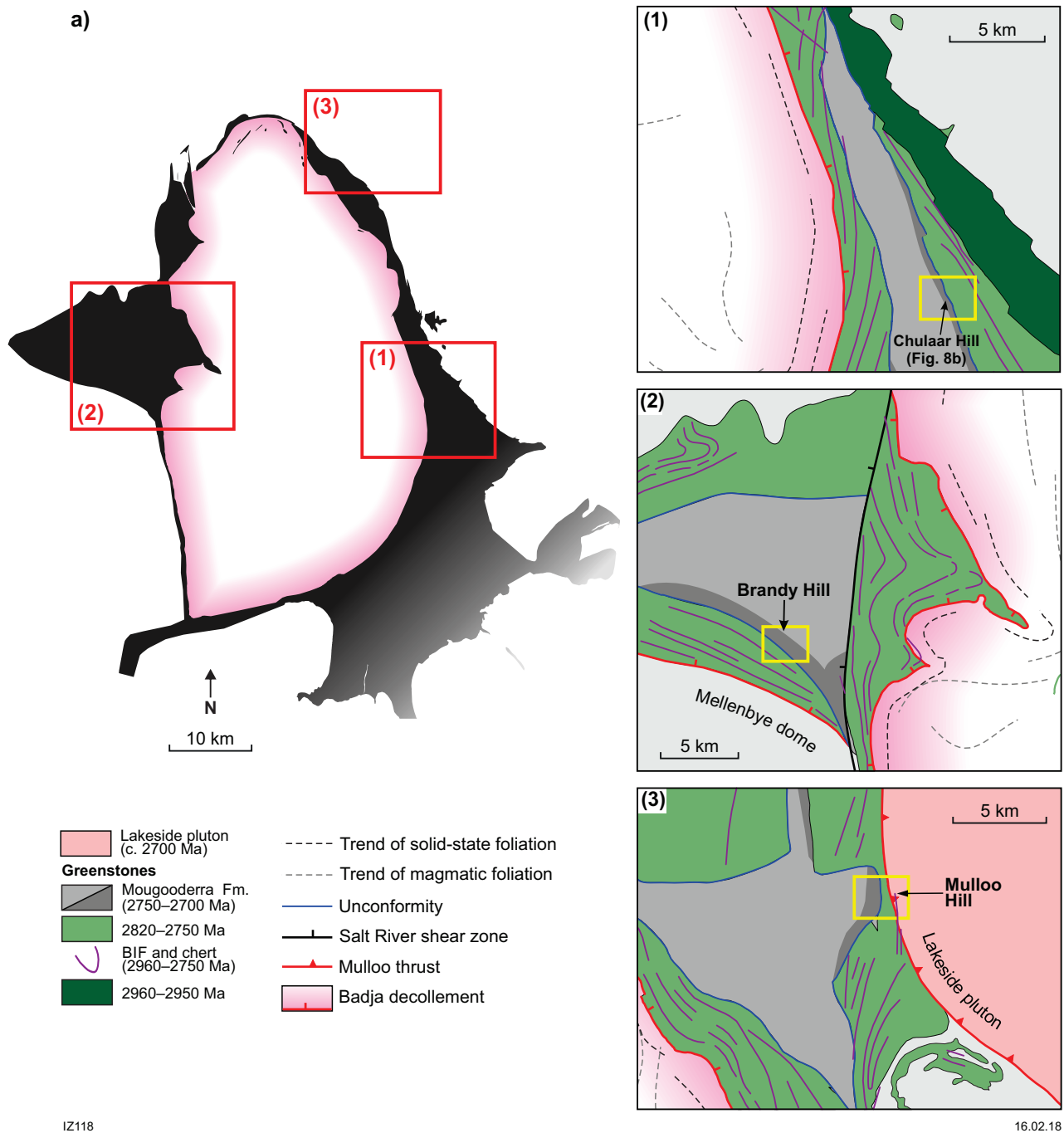


**Figure 8.** Spatial distribution and chief outcrop-scale features of the unconformity preserved within the greenstone cover: a) geological map of the three selected localities examined in this work; b) interpreted geometry of the unconformity exposed at Chulaar Hill, based on key observations. On the right, photographs I–VI show the key features of each stratigraphic layer: I) foliated metachert lacking evidence of brittle deformation features; II) heterogeneous cataclastic deformation in foliated metachert; note that the pre-cataclasite fabric is well preserved on the right-hand side of the outcrop; III) coarse-grained, monogenic chert conglomerate, here affected by a moderate solid-state foliation; IV) fining-upwards in monogenic chert conglomerate; V) exposed contact between a decimetre-sized chert clast and the sandstone matrix; VI) detail from pebbly sandstone containing centimetre- to millimetre-sized chert clasts; c) monogenic and clast-supported chert conglomerate near Brandy Hill; d) transition from chert conglomerate (right) to pebbly sandstone containing rounded chert clasts; e) sheared conglomerate at Mulloo Hill. Granite clasts (centre) are contained in a melanocratic, amphibole-rich matrix

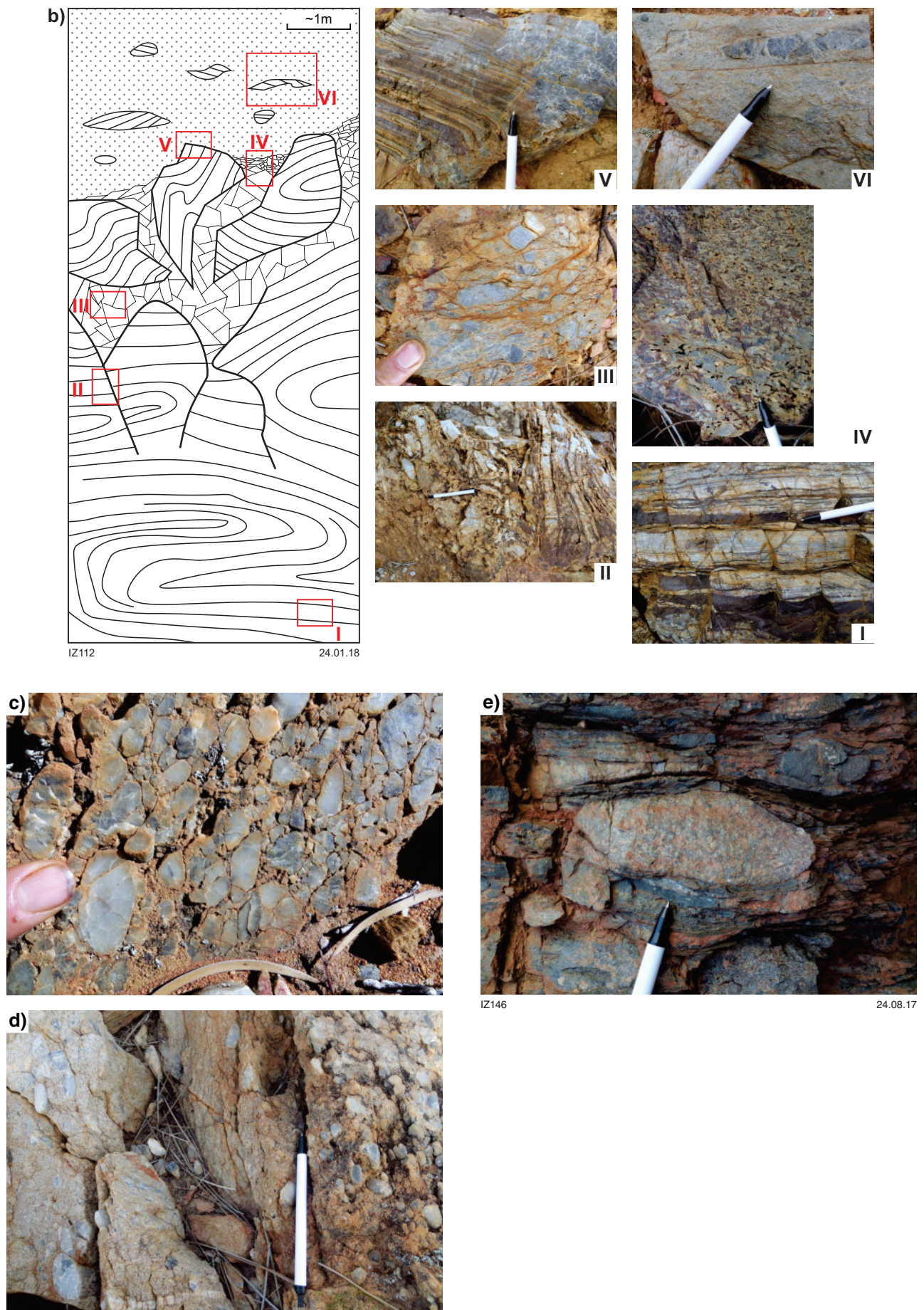


Figure 8. continued



This conglomerate sequence has a minimum thickness of 250 m. The average size of the clasts is ~50 cm near the base of the conglomerate, and it gradually decreases towards the west, where the conglomerate grades into poorly exposed metasandstones.

## Superposed structures in the greenstone cover

The strain distribution in the greenstone cover mirrors that observed in the orthogneiss domain, with the highest strain domains occurring along the Badja decollement. Here, greenstones recorded four distinct folding events that are best visible in the multilayered metasedimentary rocks such as banded iron-formation and chert. The D1 event produced a prominent transposition fabric ( $S_1$ , Fig. 9a) representing the dominant fabric in the whole dome. F1 folds developed during this stage include isoclinal and sheath folds (Fig. 9b) with steeply plunging axes ( $A_1$ ), subparallel to  $L_G$  in the orthogneiss domain, and axial planar foliation ( $S_1$ ) subparallel to the Badja decollement. The D1 fabric is associated with a major recrystallization event.  $S_1$  represents a prominent transposition fabric (Fig. 9b) and represents the dominant fabric in the whole dome. F1 folds are best developed in the layered banded iron-formation and cherts, where they show steep fold axes, parallel to stretching lineation ( $L_1$ ) in greenstone lithologies, and parallel to  $L_G$  in the underlying orthogneiss. Shear-sense determinations are more difficult in the greenstone cover, due to the generally fine-grained rock types. However, S–C and C' subfabrics are locally visible in coarse-grained amphibolite and strongly foliated schistose lithologies, and sigmoidal clasts occur locally in highly deformed breccia layers (Fig. 9c). All the fabrics indicate dome-up kinematics, which is consistent with what is observed in the orthogneiss domain.

Early folds are refolded by tight to isoclinal folds that are parallel to  $F_2$ , which is essentially coaxial and coplanar with  $F_1$ , and are associated with a spaced crenulation cleavage (Fig. 9d,e).  $F_2$  folds are common, but not as abundant as  $F_1$  folds. They can be distinguished from  $F_1$  folds because of the different fold style and, in those cases where  $A_2$  developed at an angle from  $A_1$ , because of the folded, prominent stretching lineation  $L_1$ . However, given that  $A_1$ ,  $L_1$  and  $A_2$  are nearly parallel to each other, unambiguous distinction between  $F_1$  and  $F_2$  can only be done when superposed structures occur (Fig. 9d,e).  $F_3$  folds are coplanar with  $F_1$  and  $F_2$  folds but they have subhorizontal fold axes (Fig. 9f,g).  $L_1$  folding around  $A_3$  axes is easily detectable (Fig. 9h), given that  $A_3$  are commonly at high angle to both  $A_1$  and  $L_1$ .  $F_3$  folds might correspond to the cascading folds commonly observed in mantled domes (fig. 7 in Sullivan, 2013).  $F_4$  fold generation includes a group of structures that occur only locally, and are not necessarily coeval at the scale of the Yalgoo dome. They are represented by parallel and disharmonic open folds, showing steep axial planes (AP) whose traces are commonly orthogonal to the Badja decollement.  $AP_4$  are therefore at high angles from  $AP_1$ – $AP_3$  surfaces. An example of these late folds is below under 'Badja decollement', which examines the spatial distribution of the various types of tectonites.

High-strain  $F_1$  folds are only present at a distance of <500 m from the Badja decollement. Farther away from

this high-strain zone, the oldest folds are comparable, in terms of folding style and orientation, to the  $F_2$  folds described above. These folds are associated with a moderately to well-developed, steeply plunging stretching lineation that is subparallel to the fold axes. It is unclear how these 'F<sub>2</sub>-like' folds from the lower-strain domains correlate with the  $F_1$ – $F_4$  evolution of the high-strain domains close to the Badja decollement. However, from field data, we observe that: i) there is a prominent decrease in strain in the greenstone cover with increasing distance from the Badja decollement; ii)  $F_1$ – $F_2$  folds in the high-strain domains are subparallel to each other, and subparallel to the 'F<sub>2</sub>-like' folds in the lower-strain domains; iii) the stretching lineation in the lower strain domains is not folded by 'F<sub>2</sub>-like' folds, suggesting they may be coeval. Therefore, it is possible that the development of the 'F<sub>2</sub>-like' folds might have encompassed the development of the  $F_1$  and  $F_2$  generations in the decollement. However, it is also possible that deformation propagated outwards. In this case, the oldest fabric preserved in the high-strain domains would predate 'F<sub>2</sub>-like' folds of the lower-strain domains.

The Mougooderra Formation occurs at a minimum distance of 1500 m from the Badja decollement, within relatively low-strain domains of the greenstone cover. This formation preserves 'F<sub>2</sub>-like' folds (Fig. 9i) and a steeply plunging stretching lineation, but lacks sheath folds. Because of the ambiguity in correlating structures between high- and low-strain domains, as discussed above, it is unclear whether the unconformity post-dates part of the structural evolution preserved in the high-strain domains.

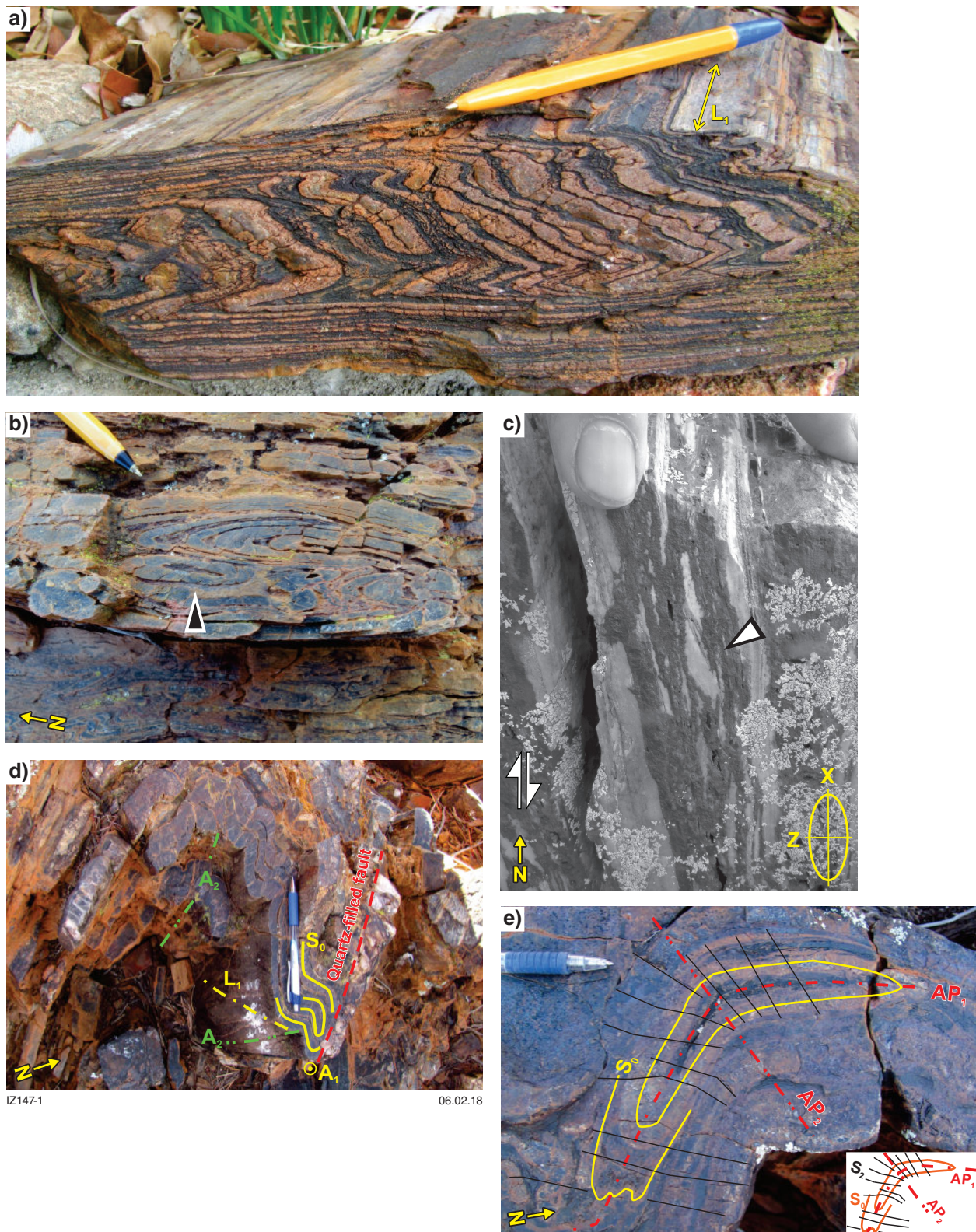
## Geometry of the main structural elements in the greenstone cover

Figure 10 summarizes the orientation of the major structures examined within each domain of the greenstone cover. Along the eastern flank of the dome,  $S_0$ ,  $S_{1-2}$  and  $F_1$ – $F_2$  fold axial surfaces trend mainly north-northwest, that is, subparallel to the trend of the Badja decollement. In the southeastern area, this high-strain zone is typically poorly exposed, and so only a smaller number of structural data are available. Along the eastern flank of the dome,  $S_0$ ,  $S_{1-2}$  and  $F_1$ – $F_2$  fold axial surfaces are steeply dipping, both to the northeast and to the southwest, in agreement with the occurrence of a dome-scale, tight syncline (Fig. 2).  $A_1$ – $A_2$  fold axes, subparallel to  $L_1$ , consistently plunge steeply to the east, close to the mean orientation of  $L_G$  in the adjacent orthogneiss (Fig. 10).

In the southwestern domain of the dome, both planar and linear fabrics are subparallel to the fabric in the structurally underlying orthogneiss (Fig. 10). Along the western flank of the dome, three distinct structural domains can be identified (Mellenbye dome margin, Buddadoo Range and Edamurta Range, Fig. 10). The main structures of the Mellenbye dome margin will be examined below under 'Outline of the structures flanking the Yalgoo dome'.

Along the eastern margin of the Gullewa greenstone belt, in the Buddadoo Range, the Badja decollement defines two arcuate structures, which are associated with the development of two east-trending synclinal greenstone keels (Fig. 2). Here, the main tectonic fabric in both greenstones and the footwall orthogneiss is parallel to the local trend of the Badja decollement and invariably





**Figure 9.** Superposed structures in the greenstone cover: a) transposed bedding ( $S_1$ ) in highly deformed banded iron-formation a few hundred metres above the Badja decollement (sample not in place); b) small-scale  $F_1$  isoclinal and sheath folds (arrowhead) in banded iron-formation; c) highly deformed, monogenic chert breccia, exposed a few metres away from the Badja decollement. Sigmoidal chert clasts indicate dome-up kinematics; d)  $F_2$  folds superposed on  $F_1$ . Type 3 fold interference pattern of Ramsay (1967); e)  $F_1$  sheath fold refolded by  $F_2$  fold in banded iron-formation. Note that  $S_2$  occurs here as a spaced cleavage; f) subvertical exposure showing  $F_3$  fold with subhorizontal axis in chert, refolding  $F_{1-2}$  isoclinal folds. The inset at lower left illustrates how the  $A_1$ – $A_2$  fold axes are folded around the  $A_3$  axes; g) upright  $F_3$  folds in chert, refolding isoclinal folds ( $F_{1-2}$ , highlighted by the yellow line); h) upright  $F_3$  folds in ultramafic schists, refolding a prominent mineral lineation marked by aligned amphibole; i) subvertical, ‘ $F_2$ -like’ folds at the Chulaar Hill unconformity locality. The fold deforms the sedimentary contact between cataclastic chert (dark grey/red) and overlying pebbly sandstone (pale grey/green)



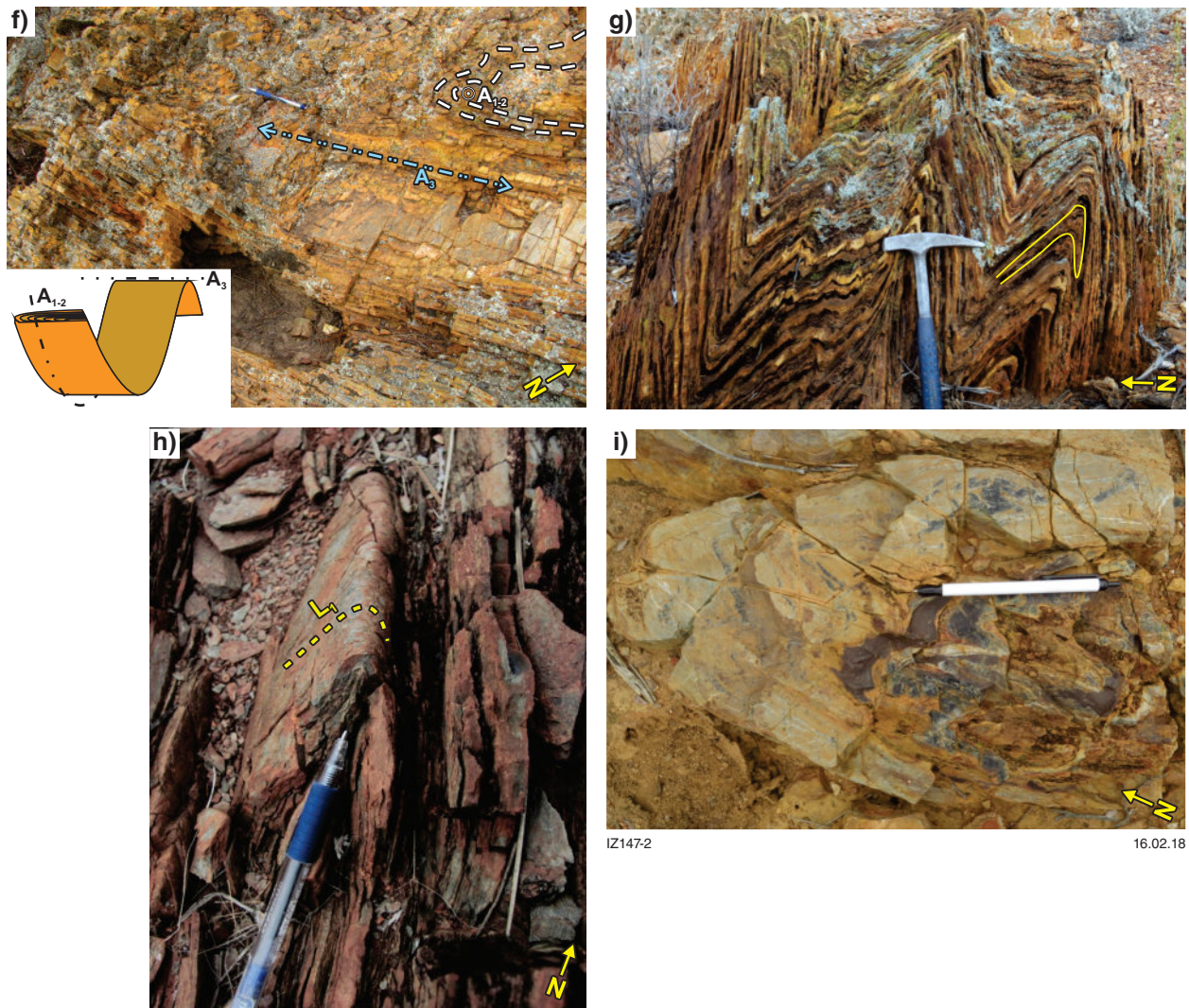


Figure 9. continued

dips towards the greenstones (Fig. 10). The structural framework of this domain will be examined further in the next section.

Along the Edamurta greenstone belt (Fig. 2), the orientation of the main planar and linear structural elements is analogous to that observed in the eastern and southwestern domains. The main foliation is northeast trending (parallel to the trend of the Badja decollement, Fig. 2) and steeply dipping to the northwest or the southeast. Stretching lineations and  $A_1$ – $A_2$  fold axes plunge steeply towards the west (Fig. 10). This domain also preserves a north-trending, steeply dipping crenulation cleavage that is examined in the next section.

Finally, along the northwestern margin of the dome, the trend of the main planar fabric is again subparallel to the trend of the Badja decollement. However, this domain differs in showing a planar fabric that dips towards the dome, in both greenstones and orthogneiss (Fig. 10). Furthermore, this domain also differs by showing a distinctive oblique attitude of the stretching lineation ( $L_1$ ), in contrast with their down-dip attitude in all the other sectors of the Badja decollement.

## The Yalgoo dome area: summary of geometry and kinematics

### The dome-forming fabric

The mesoscale fabrics described above for each lithostructural domain share some first-order characteristics (compare Fig. 7c and Fig. 10). Both magmatic and gneissic foliations in granitic rocks ( $S_{MAG}$  and  $S_G$ , respectively) are subparallel to the granite–greenstone lithological contact, coinciding with the Badja decollement.  $S_{MAG}$  and  $S_G$  are invariably outwards dipping (Fig. 7c), defining a first-order domal structure. A similar geometry is preserved in the greenstone domain, where the trace of all planar structures (transposed bedding,  $S_{1-2}$  and fold axial surfaces) is subparallel to the trace of the Badja decollement. However, equal-angle projection plots show that, particularly along the eastern flank of the Yalgoo dome, these planar structures are both outwardly and inwardly dipping (Fig. 10).



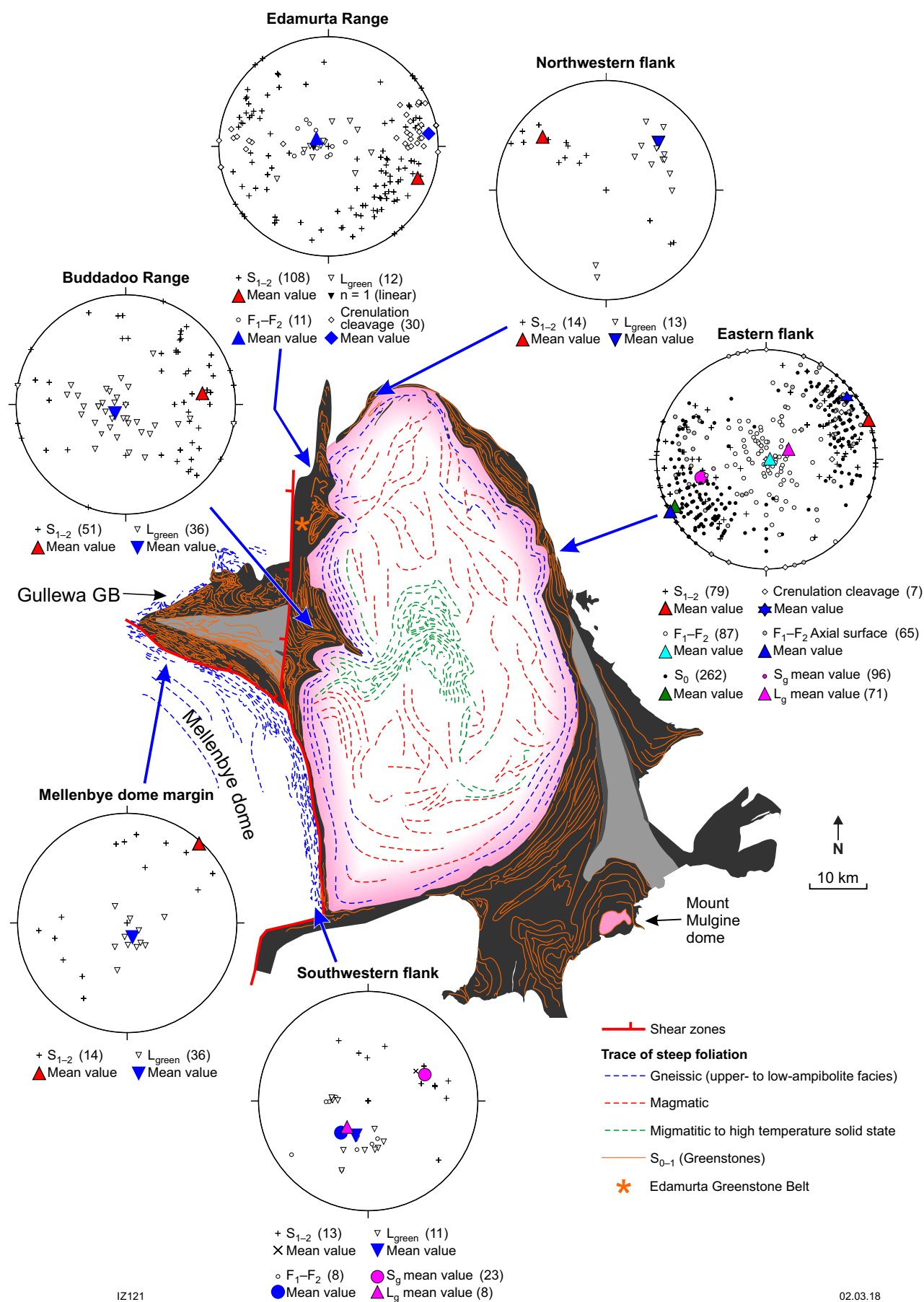


Figure 10. Equal-angle projection plots (lower hemisphere) for each structural domain identified within the greenstone cover, in the hangingwall of the Badja decollement. Number of measurements reported in brackets

Given that  $F_1$ – $F_2$  fold axial surfaces are also both outwardly and inwardly dipping ('eastern flank' plot, Fig. 10), it is likely that these patterns can be attributed to the upright  $F_3$  folds (Fig. 9e), whose axial surfaces are subparallel to the Badja decollement.

At the scale of the Yalgoo dome, the stretching lineation in granitic gneiss ( $L_G$ ) shows a radial pattern and consistently plunges outwards (Fig. 7c). In the overlying greenstones, both the stretching lineation and the  $A_1$ – $A_2$  fold axes are subparallel to  $L_G$ . Along the eastern flank of the dome, the vertical flattening induced by the  $F_3$  folds implies that linear structures in the greenstones tends to be subvertical, clustering near the centre of the equal angle plots.

In summary, the Badja decollement represents a high-strain zone that developed along the lithological contact between the granite–migmatite core and the volcano-sedimentary greenstone cover. The main fabric in both the footwall and the hangingwall of the Badja decollement is represented by a domal (outwards-dipping), concentric planar fabric and a radial, (outwards-plunging) linear fabric. Along this structure, kinematic indicators (Fig. 7b) invariably indicate normal movement, reflecting downwards (and outwards) displacement of the greenstone cover with respect to the granite–migmatite core. Such main composite fabric, which shows comparable characteristics for the entire extent of the Yalgoo dome, is therefore genetically related to the emplacement of the granite–migmatite core into the supracrustal sequence. We therefore refer to such fabric as the 'dome-forming fabric'. It is worth highlighting the composite nature of this fabric: layered metasedimentary rocks in the greenstone cover show three main generations of coplanar superposed folds, whose axial surfaces are in turn coplanar with the single, prominent gneissic foliation ( $S_G$ ) present in the structurally underlying orthogneiss.

## Outline of finite strain distribution

This section briefly examines the strain distribution among the main types of tectonite in relation to their structural position within the Yalgoo dome. Given that strain cannot be easily quantified in the case of magmatically foliated rocks (Cruden, 1990), the granitic domain (described above, Fig. 6a,b) will not be examined here.

## Kynea Tonalite

Rocks in the migmatitic core mostly show a steeply dipping foliation with a subvertical stretching and mineral lineation (Fig. 4c). The common subhorizontal exposures offer a natural section close to the YZ section of the finite strain ellipsoid (FSE). Here, most outcrops show that the development of the main  $D_{1-2}$  fabric was associated with an extension component along the Y axis of the FSE (Fig. 5b,c). Therefore, at the current exposure level, the finite strain associated with the  $D_{1-2}$  fabric likely reflects general flattening marked by a main subvertical extension vector (approximately subparallel to  $L_1$ ) and a subordinate extension parallel to the Y axis. The development of  $D_3$  and  $D_4$  fabrics was again associated with a subvertical stretching lineation ([iii] in Fig. 4c), but without a subordinate stretching component in the horizontal plane, likely reflecting (near) plane strain conditions.

## Badja decollement

Along the Badja decollement, the dominant type of tectonite varies systematically as a function of the geometry of the high-strain zone. We identify two end-member settings: i) planar segments, where the decollement shows a planar to gently convex geometry; ii) synformal keels, where the decollement defines strongly arcuate patterns, with narrow greenstone keels pointing towards the core of the dome. Planar segments represent more than 80% of the Badja decollement. On the common subhorizontal exposures (i.e. at high angle to the steeply plunging  $L_G$ ), these domains invariably show a subhorizontal extension component parallel to the Y axis of the FSE (Fig. 7a). Orthogneiss in these domains therefore contains SL tectonites that developed in the flattening field (two extension directions).

Six distinct synformal keels were identified (Fig. 11). These keels show more complex structures than the planar segments of the Badja decollement. Such complexity can be unravelled by examining both orthogneiss and greenstone domains. All the mapped keels qualitatively share some first-order structural features. We illustrate here the case of the Gnows Nest keel (Fig. 12), in the north-eastern flank of the Yalgoo dome, the best exposed greenstone keel. Here, the trace of the Badja decollement deviates from the average northwest trend of the eastern flank, and displays a concave–convex pattern defined by north- and east-trending segments (Fig. 12a). A similar geometry was described along the margin of a mantled gneiss dome in Finland ('boss and dimple' geometry; Brun et al., 1981).

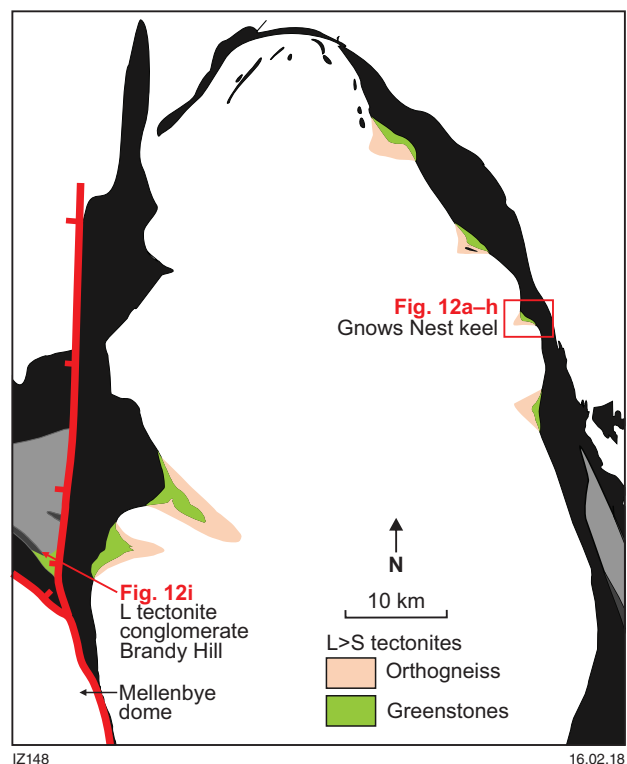


**Figure 11.** Simplified geological sketch map of the northern portion of the Yalgoo dome, showing distribution of  $L>S$  to  $L$  tectonites in both orthogneiss and overlying greenstones

Along each portion of Gnows Nest keel, planar fabrics, such as  $S_G$  in orthogneisses, and the transposed bedding and axial planes of  $F_{1-2}$  folds in greenstones, remain subparallel to the Badja decollement (Fig. 12a). Here,  $F_1$  isoclinal to sheath folds represent the dominant structures in the greenstones (Fig. 12a,b). In terms of linear fabric,  $L_G$  is steeply plunging and commonly at a high angle to the trace of the Badja decollement while, in the structurally overlying greenstones,  $A_1$  axes (subparallel to the stretching lineation) are commonly steeply plunging but show variable orientations (Fig. 12a). Notably, the symmetry of  $F_1$  folds (S and Z symmetry, Fig. 12a,b) shows a systematic spatial distribution with respect to the greenstone keel. A similar spatial distribution of fold symmetry was described by Brun et al. (1981; fig. 9b). This main fabric is overprinted by poorly to moderately pervasive, steeply dipping, spaced crenulation cleavage associated with the development of open, parallel and subvertical folds ( $S_4$ , Fig. 12b,c). Notably, the high-angle crenulation cleavage is visible in synformal keel domains only.

Field data indicate that orthogneiss and greenstones show a distinct, but in both cases systematic, spatial distribution of finite strain. In the footwall of the Badja decollement, orthogneiss shows a transition from SL tectonite (along the near-planar segments of the shear zone, Fig. 7a,b) towards  $L>S$  to L tectonite in the keel areas (Fig. 12b, d–f). The transition between end-member tectonite types occurs gradually at the kilometre scale. In greenstones, L tectonites are restricted to the hinge area of plurimetric  $F_1$  folds (Fig. 12g,h), while fold limbs are characterized by SL tectonites. In these cases, the transition between end-member tectonite types occurs quite abruptly at the metre scale. A similar strain distribution between compositionally homogeneous and heterogeneous rocks (orthogneiss and greenstones, respectively), is described in Sullivan (2013). Overprinting relationships indicate that the east-trending crenulation cleavage (Fig. 12c) post-dates the development of L tectonites in both orthogneiss and greenstones. It is notable that the constrictional fabric and a crenulation cleavage at a high angle to the Badja decollement are invariably and exclusively spatially associated with the greenstone keels (Fig. 11).

Along the western flank of the Yalgoo dome,  $L>S$  and L tectonites are developed in chert conglomerate within a greenstone keel pinched between the Yalgoo and the Mellenbye domes (Figs 11, 12i). Therefore, the development of L tectonites could reflect the occurrence of constrictional strain within a high-strain triple point zone between the two rising domes, as proposed by Bouhallier et al. (1995).

## Outline of the structures flanking the Yalgoo dome

The main structural features in the granite–greenstone systems that surround the Yalgoo dome provide first-order constraints on the tectono-magmatic evolution of the study area. There are two main granitic plutons along the western flank of the dome (Fig. 2). The northern flank of the Gullewa greenstone belt is intruded by the hornblende-bearing Cagacaroon Syenogranite, whose emplacement was dated at  $2747 \pm 3$  Ma (Champion and Cassidy, 2002). This pluton shows a prominent, east-trending gneissic

foliation, which is subparallel to the lithological contact with greenstones, and highlighted by recrystallized trails of hornblende, biotite, quartz and feldspar. The foliation is parallel to the long axes of stretched mafic microgranular enclaves and preserves a steeply plunging stretching lineation that, on subhorizontal exposures, is manifested by the preferential steep orientation of the c-axis of K-feldspar porphyroclasts (Fig. 13a). Within adjacent greenstones, banded iron-formation shows isoclinal to sheath folds with east-trending axial planes and steeply plunging axes, and mafic gneiss shows a prominent east-trending foliation, locally associated with subvertical sheath folds (Fig. 13b).

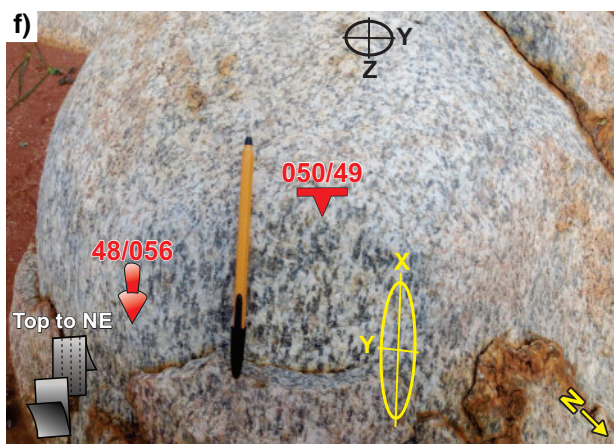
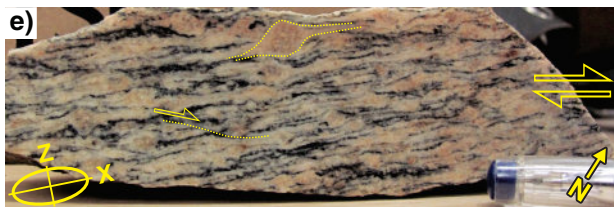
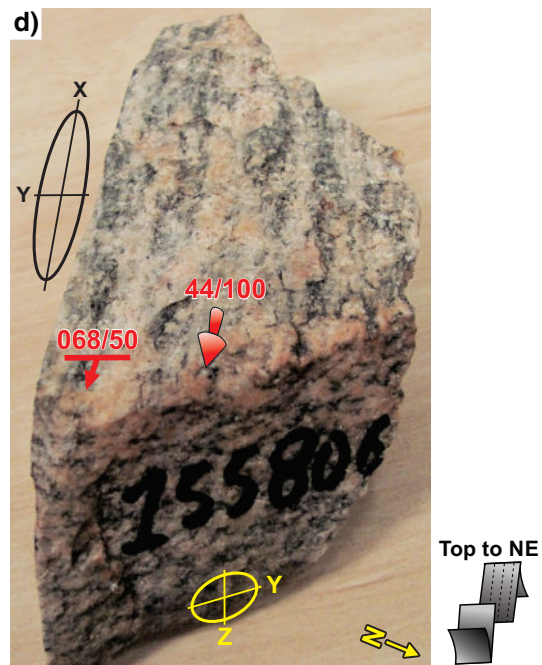
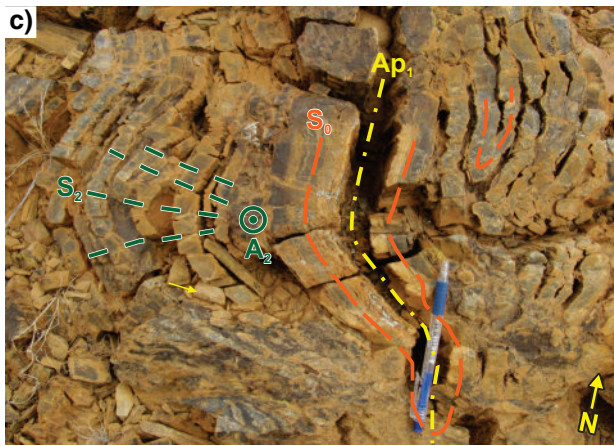
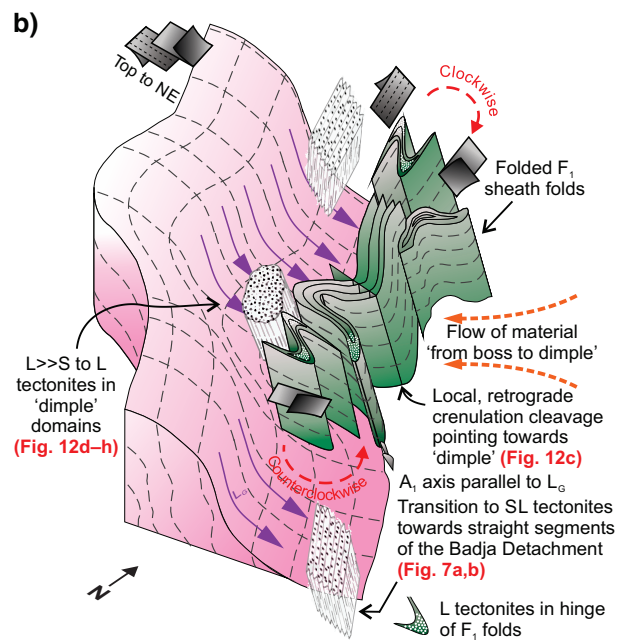
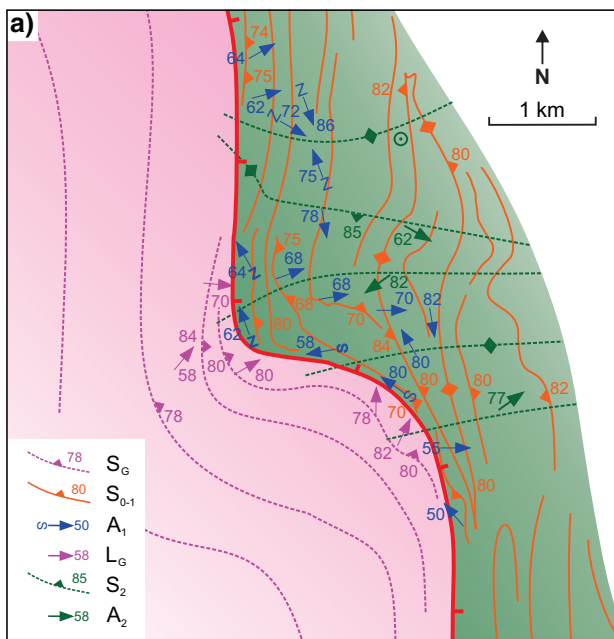
The southern flank of the Gullewa greenstone belt is occupied by the poorly exposed Mellenbye dome (Fig. 2). Here, the main tectonic fabric ( $S_1$ ?) is southeast trending, subparallel to the lithological contact with greenstones, and is both northeast and southwest dipping (Fig. 10). This is consistent with the occurrence of tight mesoscale folds with southeast-trending axial traces. This fabric is associated with a steeply plunging stretching lineation (Figs 10, 12i) and is comparable, both in terms of style and intensity, to the  $F_1$  fabric exposed along the Badja decollement, and to the fabric in the Cagacaroon Syenogranite. Along XZ sections of the finite strain ellipsoid, kinematic indicators such as S–C and C' subfabrics, and rotated clasts in siliciclastic deposits, invariably indicate greenstone-down movement. It is therefore likely that the main fabric exposed along the southern margin of the Gullewa greenstone belt developed during the emplacement of the undated Mellenbye dome (Fig. 2). The latter is largely unexposed in the area and so the main fabric in the greenstones cannot be compared with that of the structurally underlying orthogneiss. However, geophysical data suggest that the Mellenbye dome includes a prominent southeast- to south-trending planar fabric that is subparallel to the southwest margin of the Yalgoo dome (Figs 2, 10).

A third domal structure along the southeastern flank of the Yalgoo dome, the Mt Mulgine dome (Figs 2, 13c), has a small gneissic core. It is exposed over an area of  $3 \times 2$  km in map view (with an east-trending long axis), and has a gently outwards-dipping gneissic foliation that is associated with radial, outwards-plunging stretching lineations (Fig. 13c). Lithological contacts in the overlying greenstone cover have a concentric pattern (subparallel to the gneiss–greenstone boundary) and consistently dip away from the gneissic core, defining a kilometre-scale domal structure. Like the Yalgoo dome, the Mulgine dome has a high-strain zone along the gneiss–greenstone boundary and strain markedly decreases away from this boundary in the greenstone cover. Microstructures (see below) indicate that this fabric developed in the high-quartz field, at temperatures close to the granite solidus. The crystallization of the granitic precursor of the gneiss exposed in the core was dated at c. 2756 Ma (Cassidy et al., 2002).

## Regional tectonic fabric

The main groups of fabrics described above in the Yalgoo dome and adjacent granite–greenstone systems show features that vary systematically as a function of their structural position. For example, they can be concentric or radial. The structures are overprinted by a weakly to moderately pervasive tectonic fabric that is





IZ149-1

06.02.18



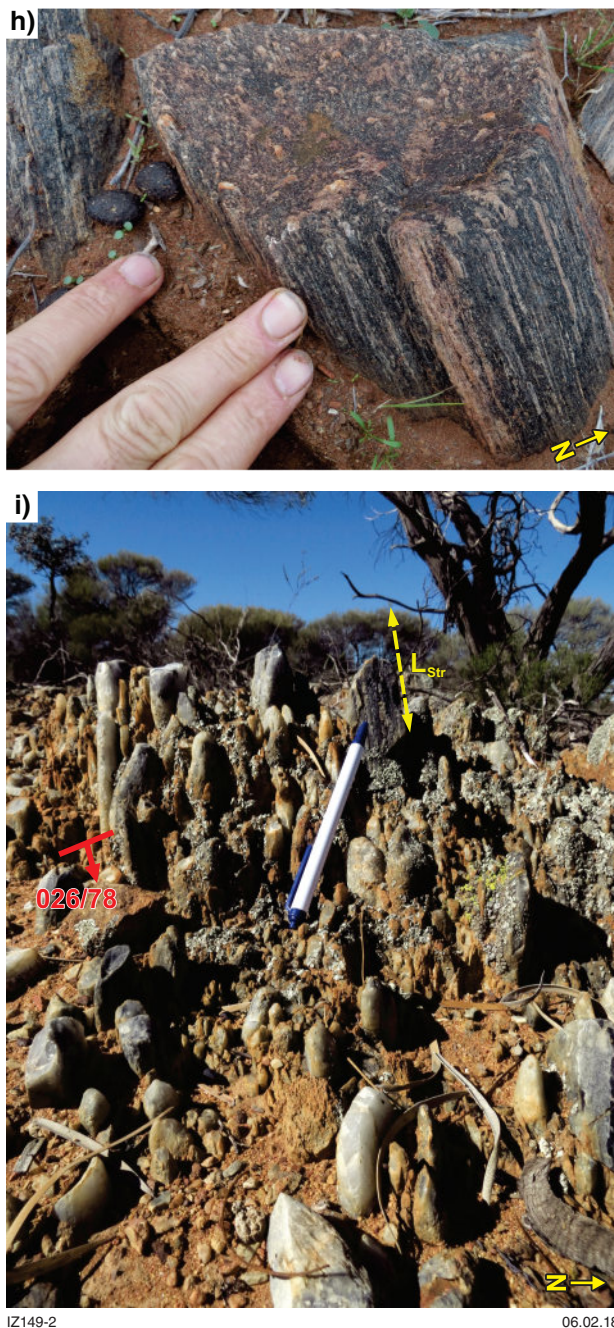


**Figure 12.** (pages 20, 21) Gnows Nest keel: a) geological map showing main structural elements; b) three-dimensional diagram summarizing the first-order geometry and structures; c)  $F_1$  isoclinal folds refolded by local  $F_2$  folds. Note the spaced  $S_2$  cleavage and the prominent intersection lineation that defines the subvertical  $A_2$  axis; d–f) orthogneiss in the footwall of the Badja decollement: d) oriented hand sample 155806, L>S tectonite from porphyritic gneiss. Note the prominent  $L_G$  visible on the foliation-parallel surface; e) same hand sample as in (d), cut parallel to  $L_G$ . Sigma-type mantled K-feldspar porphyroclasts and C' shear bands define the top-to-northeast (dome-up) kinematics; f) boulder offering a three-dimensional view of L tectonite developed in tonalite gneiss. The flat, top surface of the boulder shows a weakly developed planar fabric. In contrast, the steep sides of the boulder expose the prominent stretching lineation highlighted by aligned biotite flakes and plagioclase recrystallized aggregates; g) L tectonite in amphibolite, seen from above. The figure shows the hinge area of a plurimetric  $F_1$  fold, where L tectonites occur. In contrast, the limbs of these folds contain SL to LS tectonites; h) detail from an  $F_1$  hinge zone showing L tectonite in metagabbro; i) LS tectonite in metaconglomerate exposed near Brandy Hill

heterogeneously developed throughout the study area (Fig. 14), but is invariably north trending and subvertical to steeply east dipping. This younger fabric traverses the region without any systematic geometrical relationships with the older 'dome-forming fabric'. Moreover, the younger fabric is roughly subparallel to the large-scale, north-trending structural grain that is typical throughout the Youanmi Terrane (Fig. 1), and is subparallel to the Mulloo thrust (Fig. 2), a large-scale structure that was active during

the emplacement of the Lakeside pluton, at c. 2700 Ma (Zibra et al., 2014a). The younger north-trending fabric is thus characterized as the 'regional tectonic fabric'. In the study area, the regional foliation ( $S_R$ ) is mainly developed along the western flank of the Yalgoo dome, in an area centred along the Salt River shear zone (Fig. 14). Here,  $S_R$  appears as spaced crenulation cleavage that is typically selectively developed in less competent lithologies, such as ultramafic and metasedimentary schists (Fig. 14b), and in well-foliated/layered rocks, where  $S_R$  is axial planar to metre-scale, disharmonic parallel and kink folds with steeply plunging axes (Fig. 14c,d). Along the western flank of the Yalgoo dome,  $S_R$  is associated with north-trending, steeply dipping high-strain zones (Fig. 15a). These shear zones have a steeply plunging, prominent stretching lineation and invariably show reverse kinematics (top-to-west, Fig. 15b). Within the orthogneiss, steeply east-dipping ultramylonites are characterized by extreme grain size reduction compared with the host gneissic foliation  $S_G$  (Fig. 15c). Along the western flank of the Yalgoo dome, in the Edamurta Range, the west-dipping Badja decollement is locally reactivated as an east-verging thrust (Fig. 15d). Within these reverse high-strain zones, biotite is largely replaced by syntectonic chlorite, suggesting retrograde metamorphic conditions.

In the Kynea Tonalite, north- to north-northwesterly trending tectonic fabric ( $S_3$  and  $S_4$  fabrics) is subparallel to  $S_R$ , and so it is possible that these fabrics are genetically related, representing the expression of the regional stress field (see 'Discussion and conclusion').

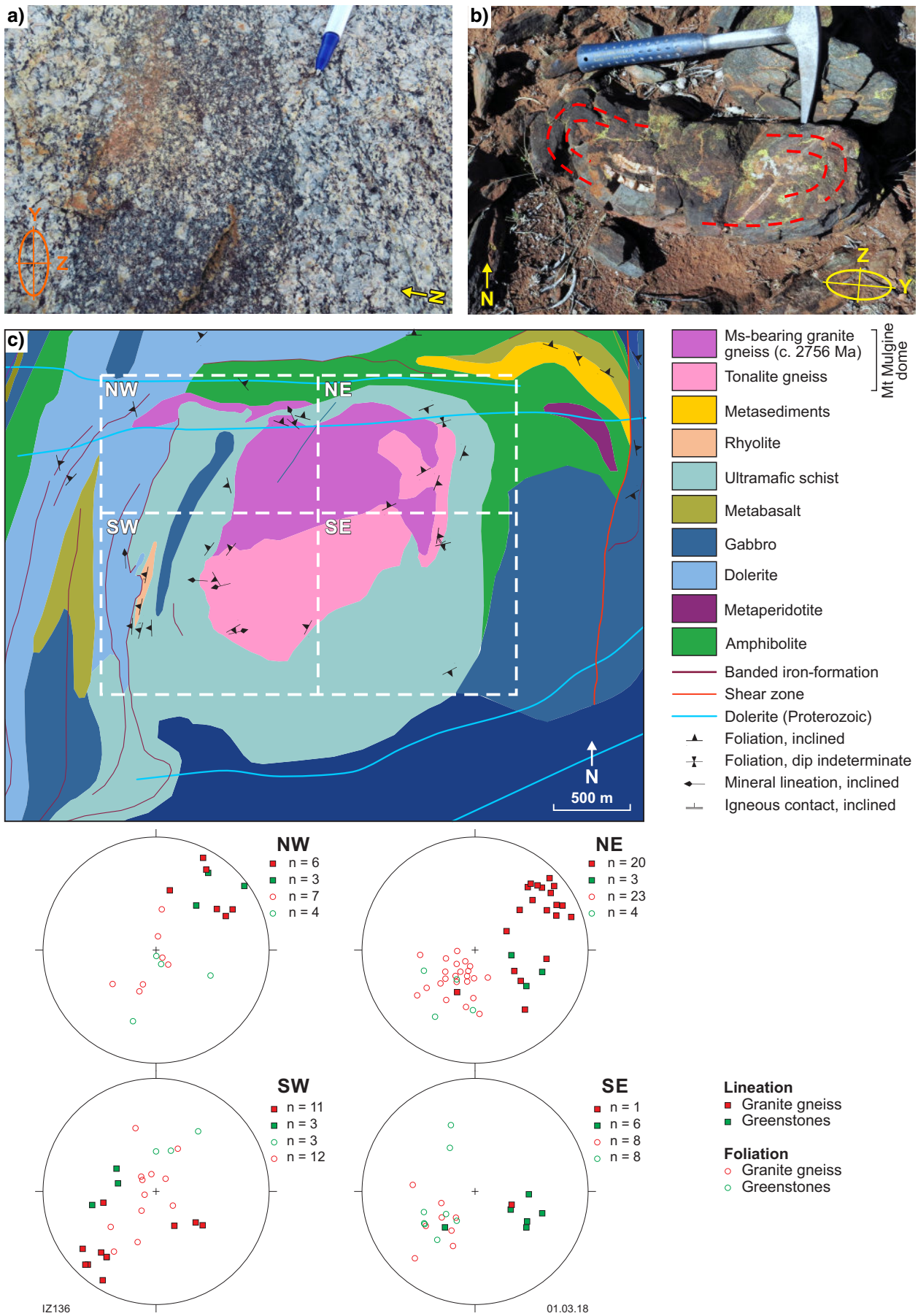


**Figure 13.** a) East-trending gneissic foliation in the Cagacaron Syenogranite, near the contact with the Gullewa greenstone belt. Note that most K-feldspar porphyroclasts offer their basal section, suggesting the occurrence of steeply plunging lineation; b) subvertical sheath fold in amphibolite near the contact with the Cagacaron Syenogranite; c) geological map of the Mount Mulgine dome. Dashed boxes identify the four structural domains. The equal-area projection plots show the distribution of gneissic foliation and stretching lineation in each of the four domains



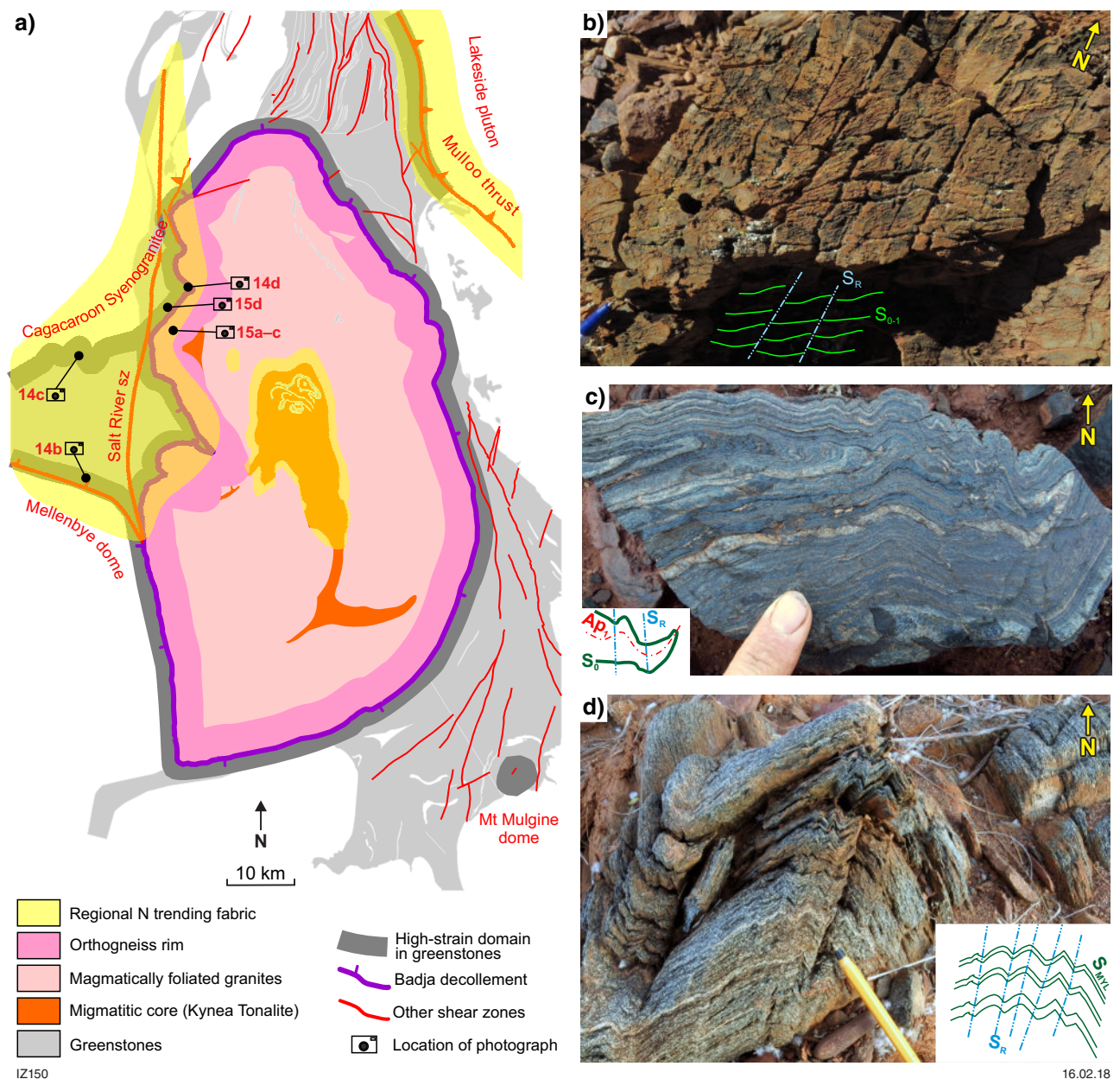


**Figure 14.** The regional tectonic fabric: a) simplified sketch map of the Yalgoo dome area showing the distribution of the north-trending tectonic foliation ( $S_R$ ), overprinting older structures and lithological contacts; b) metasandstone from the Brandy Hill area, showing north-trending spaced crenulation cleavage ( $S_R$ ) overprinting the more penetrative, east-trending  $S_{0-1}$ ; c) banded iron-formation showing east-trending isoclinal folds overprinted by folds related to north-trending  $S_R$ , near the contact with the Cagacaron Syenogranite; d) north-trending spaced crenulation cleavage ( $S_R$ ) overprinting mylonitic foliation ( $S_G$ ) in metagabbro



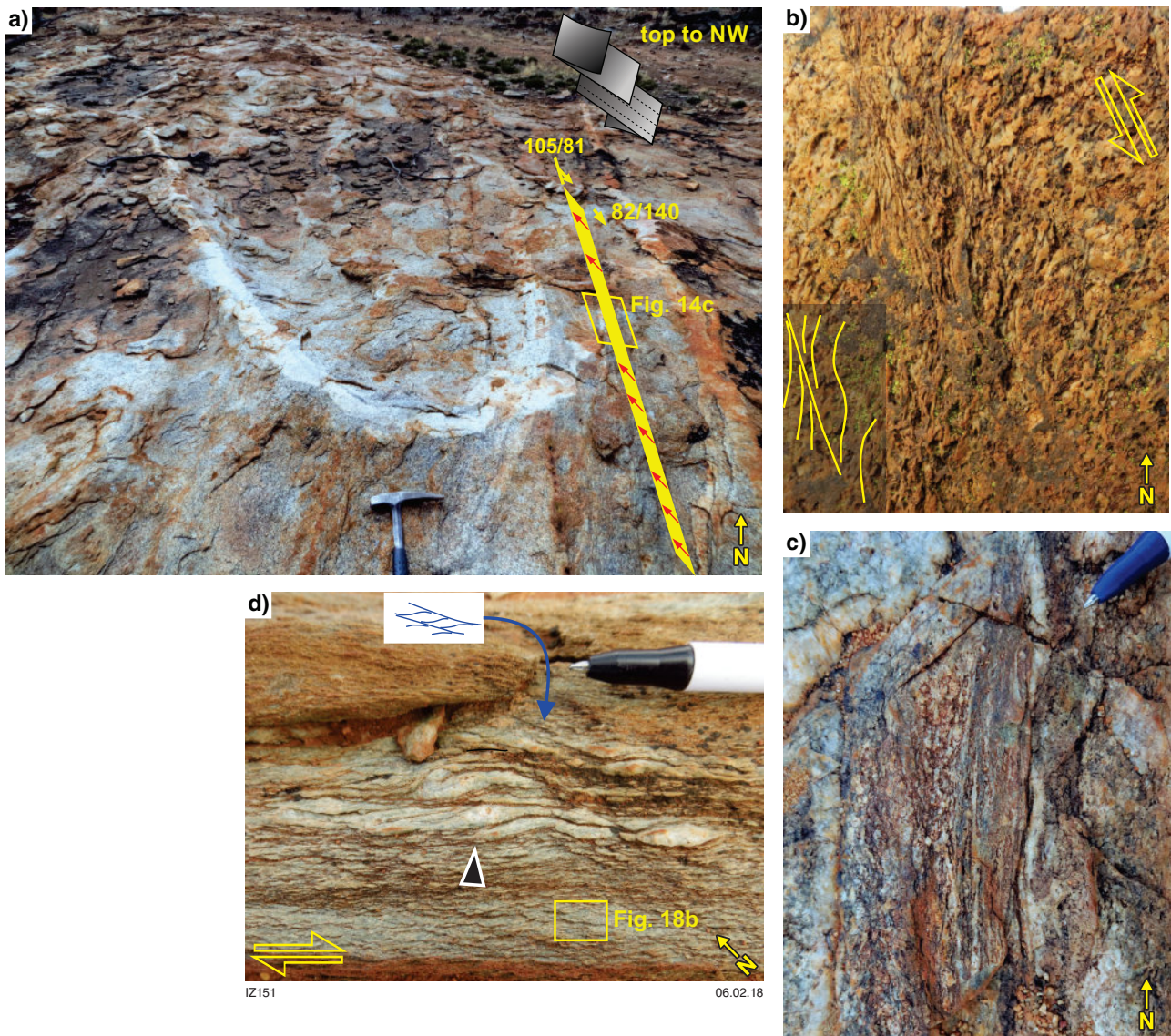


**Figure 15.** North-trending retrograde shear zones in areas of well-developed regional tectonic fabric, a–c) ultramylonite in tonalite gneiss: a) steeply east-dipping ultramylonite (highlighted by the yellow surface) post-dating  $S_6$  in host tonalite gneiss. Note the near-isoclinal fold defined by aplite vein in the footwall of the ultramylonite; b) subvertical exposure of the ultramylonite shown in (a).  $S$ – $C'$  fabric indicates east-side-up kinematics; c) detail from a) showing the pronounced grain size reduction associated with ultramylonite development; d) felsic schist from the Edamurta Range.  $S$ – $C$  fabric (arrowhead) and  $C'$  shear bands (blue arrow) indicate top-to-southeast kinematics. The corresponding microstructure is shown in Fig. 18b

## Microstructures

### Kynea Tonalite and the granitic domain

The tonalitic gneiss that forms the Kynea Tonalite is typically medium grained and contains plagioclase, quartz and biotite with minor K-feldspar, and accessory apatite, titanite and zircon. Microstructures related to  $S_{1-2}$  indicate deformation at near-solidus temperatures (Fig. 16a). Plagioclase shows widespread evidence of recrystallization, as suggested by core-and-mantle microstructure and bimodal grain size distribution. Plagioclase porphyroclasts commonly show sweeping undulose extinction, indicating deformation in the dislocation creep regime (Tullis and

Yund, 1987). Plagioclase–quartz grain boundaries are commonly cusped and lobate, indicating deformation at upper amphibolite facies conditions (Gower and Simpson, 1992). Quartz shows widespread recrystallization through grain boundary migration (Stipp et al., 2002) and chessboard subgrain boundary microstructure, indicative of deformation in the high-quartz field (Kruhl, 1996). K-feldspar occurs as narrow films coating quartz and plagioclase grain boundaries (Fig. 16b), or filling microfractures. These films likely represent evidence of residual melt during the development of the main foliation (Sawyer, 1999).  $S_3$  leucosomes have a granitic assemblage and microstructures comparable with those typical of  $S_{1-2}$ . Neither  $S_{1-2}$  nor  $S_3$  show any evidence of lower temperature solid-state overprint. Within the north-trending granitic dykes,  $S_4$  ranges from magmatic foliation to mid-amphibolite-facies gneissic foliation. In



places,  $S_4$  preserves a mylonitic fabric associated with significant grain size reduction resulting from widespread recrystallization (Fig. 16c). Microstructures suggest that  $S_4$  developed under retrograde conditions, from magmatic temperatures down to lower-amphibolite facies conditions. The domains that recorded the highest finite strain (Fig. 16c) do not show evidence of brittle deformation in feldspar, suggesting deformation temperatures  $\geq \sim 500^\circ\text{C}$  (Rosenberg, 2003).  $S_{1-2}$  in amphibolite is a continuous foliation defined by hornblende–plagioclase  $\pm$  clinopyroxene  $\pm$  quartz. Both  $D_{1-2}$  and  $D_3$  leucosomes have tonalitic compositions and include peritectic clinopyroxene, which is distinctively more coarsely grained than the matrix clinopyroxene (Fig. 16d).

Monzogranites surrounding the Kynea Tonalite mostly retain a primary magmatic fabric that locally grades into a low-strain, high-temperature gneissic fabric analogous to  $S_{1-2}$  in the tonalitic gneiss of the Kynea Tonalite. At outcrop scale, however, both end-member fabrics are classifiable as magmatic foliation, and likely reflect minor to moderate strain recorded during granite crystallization.

## Orthogneiss domain and greenstone domain

### Main gneissic fabric

In the orthogneiss domain, solid-state overprint gradually increases outwards, that is, towards the Badja decollement, where the highest finite strain is attained. Tonalitic to monzogranitic gneiss shows a gneissic foliation ( $S_G$ ) that includes elongate quartz ribbons, together with trails of recrystallized feldspar and biotite that wrap around plagioclase and K-feldspar porphyroclasts (Fig. 16e). These porphyroclasts represent former phenocrysts of magmatic origin, as indicated by concentric zoning in plagioclase and inclusions of euhedral plagioclase in K-feldspar (Fig. 16e). Both plagioclase and K-feldspar show evidence of widespread recrystallization. Aggregates of recrystallized, polygonal grains are 100–200  $\mu\text{m}$  in size (Fig. 16e) and, near the margins of porphyroclasts, they grade into subgrains of comparable size, suggesting that feldspar recrystallization probably results from dominant subgrain rotation (Rosenberg, 2003). In K-feldspar porphyroclasts, myrmekites only occur along faces subparallel to the gneissic foliation (arrowhead, Fig. 16e), suggesting that they are strain induced (Simpson and Wintsch, 1989). Both biotite and epidote are stable along the gneissic foliation.

The microstructures described above are common along most of the Badja decollement and post-date a higher temperature gneissic microfabric, which is described below.

Microstructures in the greenstone cover vary as a function of lithology. Near the Badja decollement, mafic gneiss is typically medium grained (average grain size up to 1 mm) granoblastic, and contains a hornblende–plagioclase  $\pm$  epidote assemblage. Microscale folds in banded iron-formation typically show a continuous axial-planar foliation marked by aligned quartz, magnetite and amphibole ( $S_2$ ; arrowhead in Fig. 16f), suggesting amphibolite facies conditions.  $S_2$  refolds the primary

bedding ( $S_0$ ), which contains elongate amphibole aggregates (Fig. 16f), suggesting that the folded surface represents a composite  $S_1$ – $S_2$  foliation.

Away from the Badja decollement, in mafic schists, actinolite replaces hornblende and the average grain size is generally  $<1$  mm. Similarly, banded iron-formation typically shows granoblastic texture near the Badja decollement, and average grain size gradually decreases away from this major high-strain zone.

### Relics of high-temperature microfabric

In the orthogneiss exposed along the southwest portion of the Badja decollement,  $S_G$  shows microstructures that differ substantially from the more common microfabric described in the previous section. In this area,  $S_G$  is marked by aligned K-feldspar and plagioclase porphyroclasts that are mantled by coarse-grained polygonal aggregates of the same phases (Fig. 17a). This microstructure likely reflects feldspar recrystallization at a high temperature (Rosenberg, 2003). Quartz forms elongate, mono- to polycrystalline, coarse-grained ribbons (up to several millimetres long, Fig. 17b). Here, individual quartz grains, of probable magmatic origin, have a chessboard subgrain boundary pattern (Fig. 17b), reflecting deformation in the high-quartz field at near-solidus temperatures (Kruhl, 1996). Microfractures in feldspar are filled by quartz that is in optical continuity with the matrix quartz, likely reflecting melt-present microfracturing (Zibra et al., 2012). Quartz–plagioclase grain boundaries are strongly cusped to lobate (arrowheads, Fig. 17c), reflecting deformation at high temperature (Gower and Simpson, 1992). Microstructures comparable to those preserved within the southwest domain are also locally preserved along the internal portion of the Badja decollement.

### The Mt Mulgine dome and the regional tectonic fabric

The gneissic foliation in the granitic gneiss exposed in the core of the Mt Mulgine dome is defined by coarse-grained polycrystalline quartz ribbons that are interleaved with mica flakes and recrystallized plagioclase and K-feldspar (Fig. 18a). Recrystallized feldspars are 100–400  $\mu\text{m}$  in size, and quartz–feldspar grain boundaries are markedly lobate (Fig. 18a), indicating that foliation developed at a high temperature (Gower and Simpson, 1992; Passchier and Trouw, 2005).

In the Mt Mulgine dome, the regional tectonic foliation ( $S_R$ ) is a poorly to moderately developed, retrograde crenulation cleavage.  $S_R$  is present in fine-grained schists, such as in the metasedimentary sequence exposed in the Edamurta Range (Fig. 10). Here,  $S_G$  in garnet–mica schists is defined by a biotite–muscovite–plagioclase–quartz assemblage that wraps around pre-tectonic garnet porphyroblasts. The development of  $S_R$  spaced crenulation cleavage was associated with biotite retrogression into chlorite, and with brittle deformation in garnet (Fig. 18b). The main syntectonic assemblage within the localized reverse shear zones reactivating the Badja decollement (Fig. 15d) includes chlorite, albite and quartz (Fig. 18c), suggesting that these younger shear zones developed at low-greenschist facies conditions.



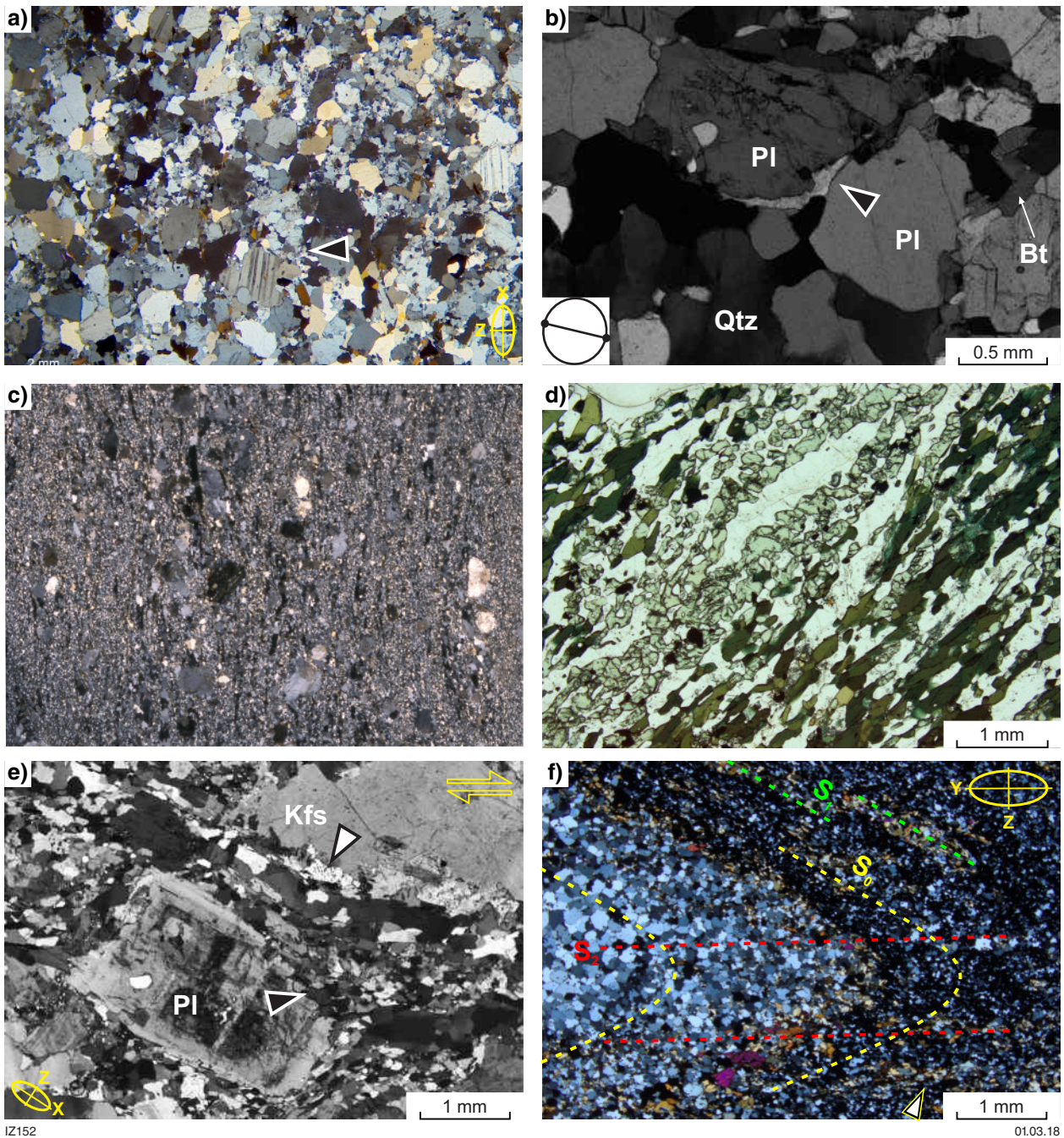
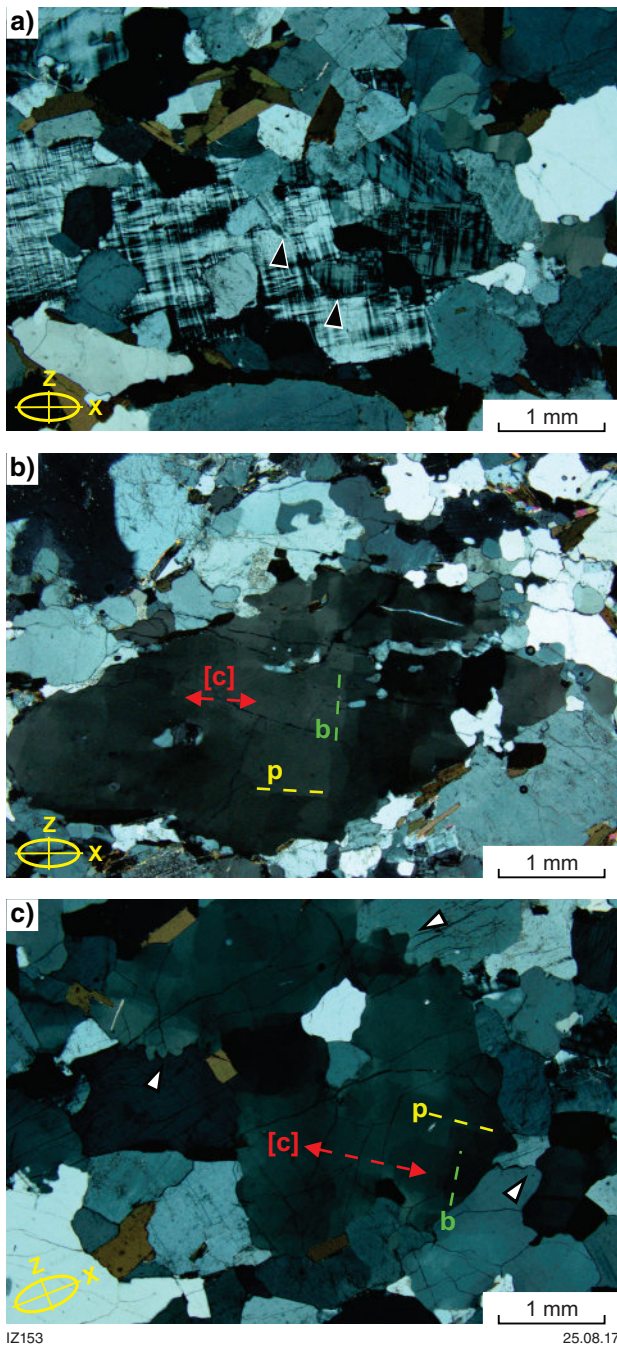


**Figure 16.** Typical microstructure of  $S_{1-2}$  from tonalite gneiss (Kynea Tonalite) and from the Orthogneiss Domain. All micrographs were taken with crossed polars, unless specified otherwise: a) high-temperature microstructure in migmatitic tonalite. Arrowhead points to an aggregate of deeply sutured plagioclase porphyroblasts, suggesting recrystallization at high temperature; b) thin film of K-feldspar at high angle from  $S_{1-2}$  in tonalite gneiss; c) mylonitic foliation ( $S_4$ ) from a sheared, north-trending dyke of porphyritic granite. Extreme grain size reduction likely occurred by syntectonic recrystallization. Feldspar porphyroclasts show sweeping undulose extinction, indicative of dislocation creep processes; d) detail of a millimetre-sized leucosome in amphibolite. Leucosome contains clinopyroxene–plagioclase–quartz assemblage. Host amphibolite also contains fine-grained clinopyroxene. Plane-polarized light; e) high-strain porphyritic gneiss from the orthogneiss domain. Both feldspars show core-and-mantle microstructures, and K-feldspar shows strain-induced myrmekites (white arrowhead) developed along crystal faces parallel to  $S_0$ . Black arrowhead points to coarse-grained recrystallized plagioclase aggregates, near the margins of a plagioclase porphyroclast; f) detail from the hinge zone of millimetre-sized fold in metamorphic banded iron-formation. The folded bedding ( $S_0$ ) contains elongate amphibole aggregates, suggesting that it represents a composite  $S_{0-1}$  surface. A younger axial planar fabric ( $S_2$ ) is locally marked by aligned amphibole aggregates. The thin section was prepared at a high-angle from the stretching lineation (i.e. it is nearly parallel to the Y–Z section of the finite strain ellipsoid), accounting for the lack of shape fabric in quartz aggregates

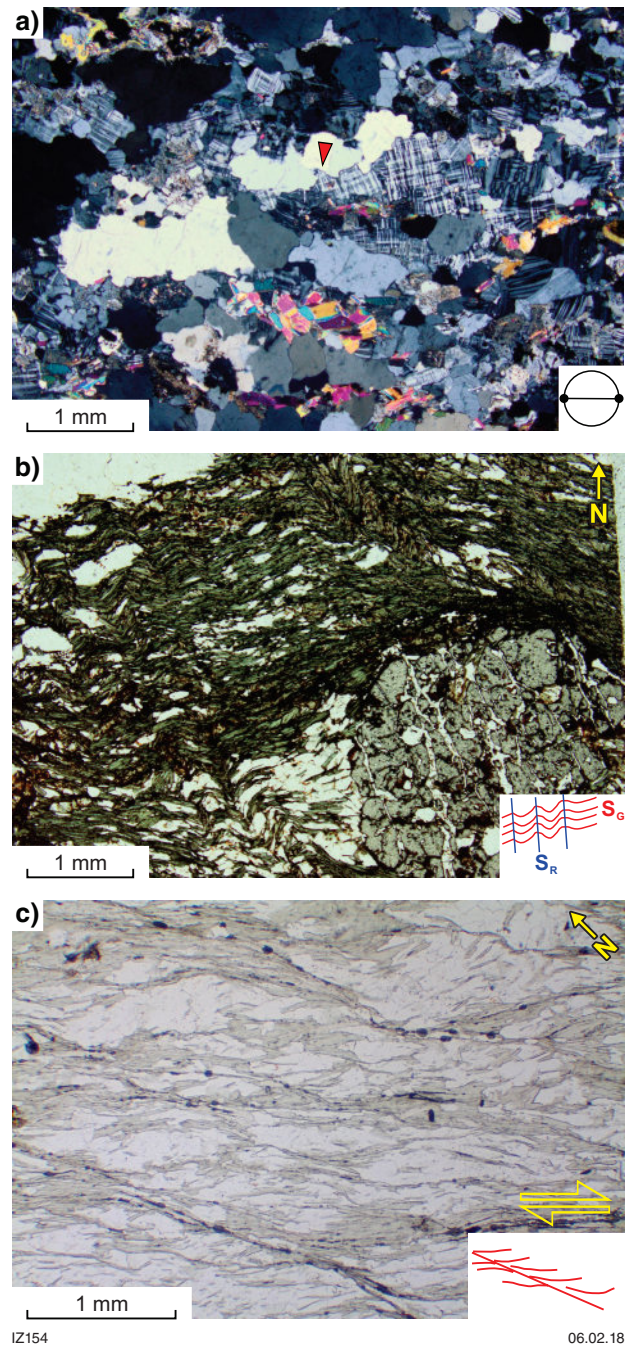




IZ153

25.08.17

**Figure 17.** Relics of high-temperature microfabric preserved in  $S_6$ : a) coarse-grained polygonal K-feldspar aggregates (arrowhead) mantling a K-feldspar porphyroblast; b) chessboard subgrain boundary pattern in quartz porphyroblast, defined by a combination of basis-parallel ('b') and prism-parallel ('p') subgrain. The red line indicates the trace of the quartz c-axis; c) strongly cusped-lobate quartz-plagioclase grain boundaries (some examples are indicated by the white arrowheads) in tonalite gneiss sampled along the southwest margin of the orthogneiss domain



IZ154

06.02.18

**Figure 18.** Typical microstructures from the regional tectonic fabric ( $S_6$ ): a) high-temperature foliation in granitic gneiss from the core of the Mount Mulgine dome. The foliation is marked by elongate and coarse-grained recrystallized aggregates of quartz, plagioclase and K-feldspar, together with aggregates of muscovite flakes. Red arrowhead points to a representative example of a coarsely cusped-lobate quartz-plagioclase grain boundary; b) garnet micaschist from Edamurta Range.  $S_6$  crenulation produced disharmonic kink folds in the chlorite-rich matrix. In contrast,  $S_6$  in garnet is manifested as 'fracture cleavage'. This overprints an early foliation that developed a strain shadow around the garnet that folded the  $S_6$ ; c) microstructure from the felsic schist in Fig. 15d. It contains chlorite-quartz-albite syntectonic assemblage.  $S/C'$  fabric defines top-to-southeast kinematics, supporting mesoscale observation

## Quartz Crystallographic Preferred Orientation (CPO)

In order to constrain the deformation temperature, type of strain and bulk flow, and prevailing shear sense in the main structural domains, we determined the quartz Crystallographic Preferred Orientation (CPO) in six samples from the Kynea Tonalite and from the granitic domain, 16 samples from the orthogneiss domain, four samples from the greenstone cover, and two samples representative of the Cagacaron Syenogranite and the Mt Mulgine dome (Fig. 19a). All samples were scanned with an automated fabric analyser microscope (Paternell et al., 2010), and the CPO was determined using the FAME (Fabric Analyser Microstructure Evaluation) software (Hammes and Paternell, 2016).

Five samples from the Kynea Tonalite (GSWA samples 155827, 155879, 155880, 155884 and 209689) show near-X maxima associated with secondary near-Z maxima, indicative of dominant prism  $\langle c \rangle$ -slip in cooperation with subordinate basal  $\langle a \rangle$  slip (Fig. 19b). This represents the typical fabric developed during non-coaxial shearing at near-solidus temperatures (Mainprice et al., 1986; Stipp et al., 2002). GSWA sample 155883 differs in showing main near-Z maxima. Given that this sample preserves a high-temperature microfabric, near-Z maxima likely reflects the existence of a domainal fabric, as commonly observed in rocks deformed at high temperatures (Zibra et al., 2010). In all samples, external symmetry indicates upwards displacement of the migmatitic core with respect to the surrounding granites. Quartz CPO fabrics from the granitic domain are generally weak (Fig. 19b). However, except for GSWA samples 155867 and 155869, four samples show diffuse to well-developed maxima in the near-X position, in agreement with the preserved high-temperature magmatic fabrics in these samples.

Most samples from the orthogneiss domain show well-defined to diffuse near-Z maxima (e.g. GSWA samples 155871, 210275, 210276 and 212730) that indicate dominant basal  $\langle a \rangle$  slip (Fig. 19b). Some samples show additional maxima in near-Y and intermediate positions (e.g. GSWA samples 155806, 155822, 210297), developing a crossed girdle fabric (Lister, 1977), which indicates that prism and rhomb  $\langle a \rangle$  slip cooperated in producing the observed fabric. An incipient to well-developed crossed girdle fabric is also apparent in the four greenstone samples collected in the hangingwall of the Badja decollement (Fig. 19a). As indicated by the observed microstructures, these fabrics suggest that the main foliation along the Badja decollement developed at mid- to lower-amphibolite facies conditions (Passchier and Trouw, 2005). The CPO of the three samples collected in the southwestern area show moderately to well-developed near-X maxima, whose external symmetry is consistent with the normal kinematics observed along the Badja decollement. This CPO fabric is consistent with the observed microstructure, indicating that, in this portion of the Badja decollement, the gneissic foliation developed at near-solidus temperatures, and mostly under melt-present conditions (Fig. 17a–c). GSWA sample 155876, which is representative of the gneissic foliation exposed in the core of the Mt Mulgine dome, shows a weakly developed near-X maximum that, in agreement with the observed microstructures (Fig. 18a), indicates fabric development

at a high temperature, in the high-quartz field. GSWA sample 210292 from the Cagacaron Syenogranite shows a weak quartz CPO fabric, with some maxima scattered in the near-Z position and additional, very weak maxima in the near-X position. Microstructures from this sample are characterized by fully plastic deformation in feldspar, with the development of strain-induced myrmekites and coarse-grained recrystallized quartz aggregates, which suggests foliation development at mid-amphibolite facies conditions (Simpson and Wintsch, 1989). The weak quartz CPO fabric may result from the occurrence of millimetre- to centimetre-sized K-feldspar and hornblende porphyroclasts, which likely induced grain-scale strain perturbations during foliation development.

## Geochronology

In this section, we present new geochronology data for samples from each of the lithostructural domains identified above. Data are provided in Table 1, and illustrated in Figure 20.

### Analytical methods

Zircons were separated using standard magnetic and density techniques. The zircons, together with zircon reference materials (BR266 and OGC), were cast in epoxy mounts and polished to expose the interiors of the crystals. Each mount was characterized with transmitted light, reflected light, and cathodoluminescence (CL) images. U–Th–Pb ratios and absolute abundances were determined relative to the BR266 standard zircon (559 Ma, 903 ppm  $^{238}\text{U}$ ) (Stern, 2001), analyses of which were interspersed with those of unknown zircons. Accuracy of  $^{207}\text{Pb}^*/^{206}\text{Pb}^*$  ratios ( $\text{Pb}^* = \text{radiogenic Pb}$ ) was monitored during each session by analysis of the 3465 Ma OGC zircon standard (OG1; Stern et al., 2009). Measured compositions were corrected for common Pb using non-radiogenic  $^{204}\text{Pb}$  and contemporaneous Pb compositions according to the terrestrial Pb evolution model of Stacey and Kramers (1975). Mean ages are quoted with 95% uncertainties ( $t_{95}/\text{MSWD}$ ; Ludwig, 2003) and the value of the mean square of weighted deviates (MSWD).

### Geochronology results

#### GSWA 209689: metatonalite

GSWA sample 209689 is a medium-grained metatonalite, consisting of about 40% plagioclase, 35% quartz, 10% biotite, 5% K-feldspar and accessory titanite, apatite, epidote and zircon. The foliation is defined by aligned biotite flakes and moderately stretched quartz ribbons. Quartz and plagioclase show cusped–lobate grain boundaries, and synmagmatic microfractures are locally visible, indicating melt-present deformation.

Zircons from this sample are colourless to dark brown, and mainly subhedral. The crystals are up to 400  $\mu\text{m}$  long, and elongate, with aspect ratios up to 8:1. In cathodoluminescence (CL) images, concentric zoning is ubiquitous. Many crystals contain high-uranium,



metamict zones and low-uranium outer zones. Twenty-three analyses obtained from 18 zircons are concordant to strongly discordant (Fig. 20a). Seven analyses >14% discordant or indicating high common Pb are considered not to be geologically significant. The remaining 16 analyses can be divided into two groups. Fifteen analyses of 15 zircons yield a discordia regression with intercepts at  $2960 \pm 10$  Ma and c. 500 Ma (MSWD = 1.04). The upper intercept date of  $2960 \pm 10$  Ma for the 15 analyses in Group I is interpreted as the magmatic crystallization age of the tonalite. One analysis yields a  $^{207}\text{Pb}^*/^{206}\text{Pb}^*$  date of  $2857 \pm 30$  (1 $\sigma$ ) Ma, interpreted to reflect ancient loss of radiogenic Pb.

### GSWA 214324: metamonzogranite dyke

This sample was collected from a coarse-grained, gneissic monzogranite dyke intruded into metatonalite (GSWA 209689). The sample consists of about 30% plagioclase, 30% K-feldspar, 30% quartz, 5% biotite, and accessory opaque minerals, apatite and zircon. Metamorphic foliation is defined by elongate quartz ribbons wrapped around feldspar porphyroclasts, which are up to 10 mm in size. Microstructures suggest that the foliation developed under mid-amphibolite facies conditions.

Zircons isolated from this sample are colourless to dark brown, and subhedral to euhedral. The crystals are up to 450  $\mu\text{m}$  long, and elongate, with aspect ratios up to 8:1. In CL images, concentric zoning is ubiquitous. Many crystals contain high-uranium, metamict zones, and some crystals appear to contain older cores. Eighteen analyses of 18 zircons are concordant to strongly discordant (Fig. 20b). Four analyses >5% discordant were discarded. The remaining 14 analyses can be divided into two groups. Thirteen analyses yield a weighted mean  $^{207}\text{Pb}^*/^{206}\text{Pb}^*$  date of  $2705 \pm 6$  Ma (MSWD = 0.60), interpreted as the magmatic crystallization age of the monzogranite dyke. One analysis of a zircon core yields a  $^{207}\text{Pb}^*/^{206}\text{Pb}^*$  date of  $2943 \pm 9$  Ma (1 $\sigma$ ), which is similar to the crystallization age of the host metatonalite (GSWA 209689). This is in agreement with field and geochemical evidence (Clos, Zibra and Weinberg, 2016), indicating that the dyke assimilated portions of the host metatonalite.

### GSWA 214315: metamonzogranite dyke

The sample is from a monzogranite dyke (Fig. 5f) that is intruded into metatonalite (GSWA 209689), and contains biotite-rich schlieren and inclusions of tonalite. The rock mostly retains a primary magmatic fabric, and consists of about 30% plagioclase, 30% K-feldspar, 30% quartz, 5% biotite, and accessory apatite and zircon. The tonalite xenoliths are compositionally and microstructurally comparable to those of sample GSWA 209689, which is representative of the host metatonalite.

Zircons from this sample are colourless to dark brown and subhedral to euhedral. Concentric zoning is ubiquitous, and many crystals contain high-uranium metamict zones. Eighteen analyses of 18 zircons are concordant to moderately discordant (Fig. 20c). Seventeen analyses yield a weighted mean  $^{207}\text{Pb}^*/^{206}\text{Pb}^*$  date of  $2700 \pm 7$  Ma

(MSWD = 1.8), interpreted as the igneous crystallization age of the dyke. One analysis of a zircon core yields a  $^{207}\text{Pb}^*/^{206}\text{Pb}^*$  date of  $2958 \pm 20$  Ma (1 $\sigma$ ), which is similar to the crystallization age of the host metatonalite (GSWA 209689).

### GSWA 155858: metamonzogranite

This monzogranite consists of about 40% plagioclase, 30% quartz, 25% K-feldspar, 5% biotite and chlorite, and accessory apatite and zircon. Primary grains are well preserved. Microstructures, such as high-temperature recrystallization in quartz and synmagmatic microfractures, suggest melt-present deformation, likely reflecting syn-emplacement shearing.

Zircons from this sample are colourless to dark brown, and mainly subhedral. The crystals are up to 400  $\mu\text{m}$  long, and elongate, with aspect ratios up to 6:1. Concentric zoning is ubiquitous; and many crystals are dominated by high-uranium, metamict zones. Only five zircons were analysed successfully, owing to very high common-Pb contents. The analyses are slightly discordant (Fig. 20d), and yield a weighted mean  $^{207}\text{Pb}^*/^{206}\text{Pb}^*$  date of  $2752 \pm 13$  Ma (MSWD = 1.3), interpreted as the magmatic crystallization age of the monzogranite.

### GSWA 214101: monzogranite gneiss

The sample is a coarse-grained monzogranite gneiss, consisting of about 30% plagioclase, 30% quartz, 30% K-feldspar, 5% biotite, and accessory opaque minerals, apatite, epidote and zircon. K-feldspar porphyroclasts are up to 2 cm in size and wrapped by elongate trails of biotite and quartz ribbons, defining the metamorphic foliation. Strain-induced myrmekites commonly occur along K-feldspar margins parallel to the foliation. Microstructures indicate that the fabric developed under mid- to low-amphibolite facies conditions.

The zircons are colourless to dark brown, and subhedral to euhedral. The crystals are up to 400  $\mu\text{m}$  long, and elongate, with aspect ratios up to 4:1. Concentric zoning is ubiquitous, and many crystals contain high-uranium, metamict zones. Thirteen analyses of 13 zircons are concordant to strongly discordant (Fig. 20e). One analysis >5% discordant was discarded. Twelve analyses yield a discordia regression, with intercepts at  $2763 \pm 6$  Ma and c. 650 Ma (MSWD = 1.1). The upper intercept of  $2763 \pm 6$  Ma is interpreted as the magmatic crystallization age of the monzogranite protolith.

### GSWA 214138: granodiorite gneiss

The sample is a granodiorite gneiss, consisting of about 40% plagioclase, 35% quartz, 10% K-feldspar, 5% biotite, and accessory opaque minerals, apatite, epidote and zircon. Plagioclase porphyroclasts are up to 1 cm in size and wrapped by elongate trails of biotite and quartz ribbons, defining the metamorphic foliation. Microstructures indicate that fabric developed under mid- to low-amphibolite facies conditions.

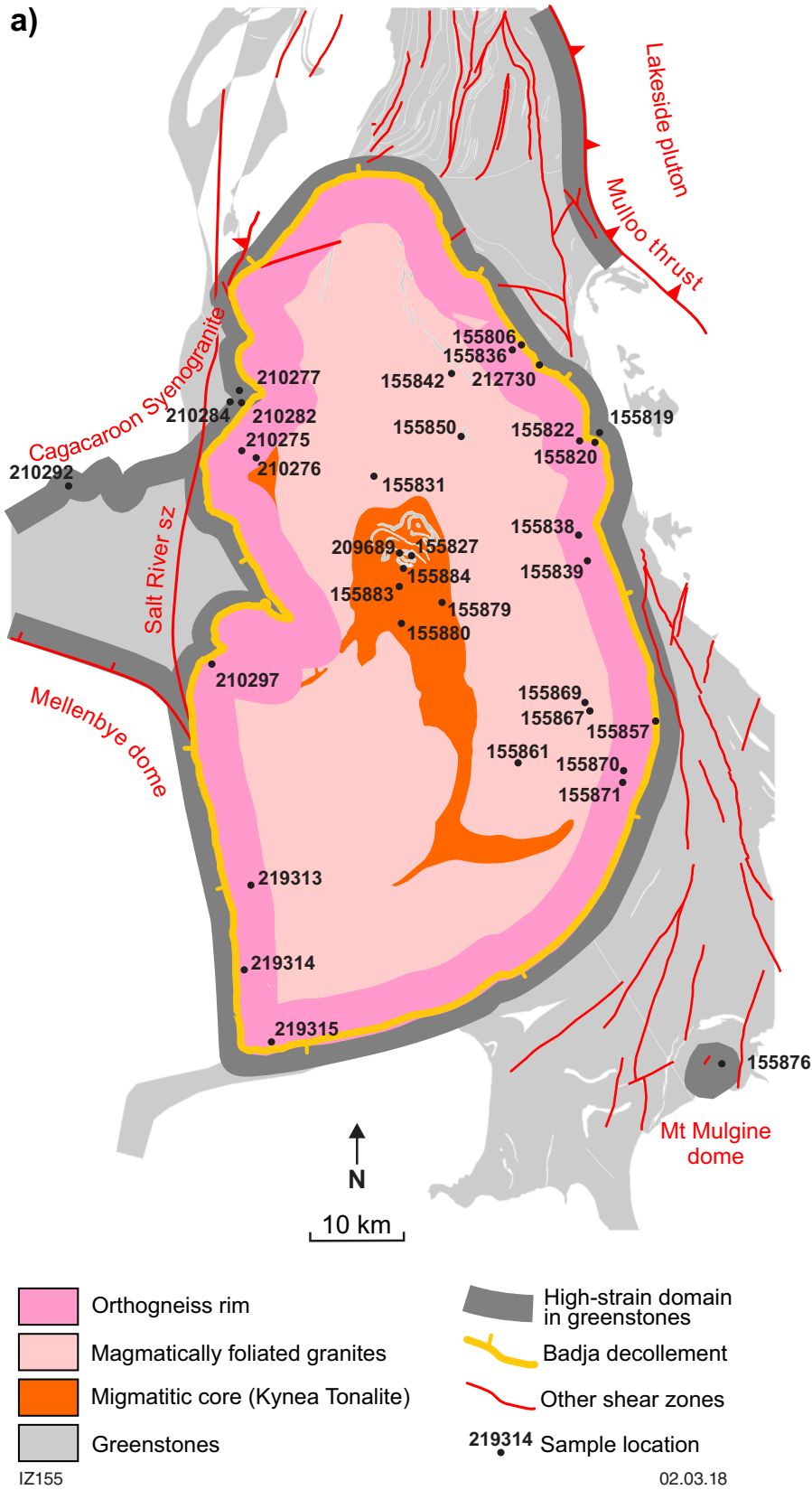


Figure 19. a) Simplified sketch map of the study area showing location of the samples selected for quartz CPO investigation; b) summary of quartz CPO data from the domains identified in the Yalgoo dome area. For each equal area stereographic projection (lower hemisphere, 1% of search area). Shear plane and sense of shear are indicated for samples showing fabric clear external symmetry

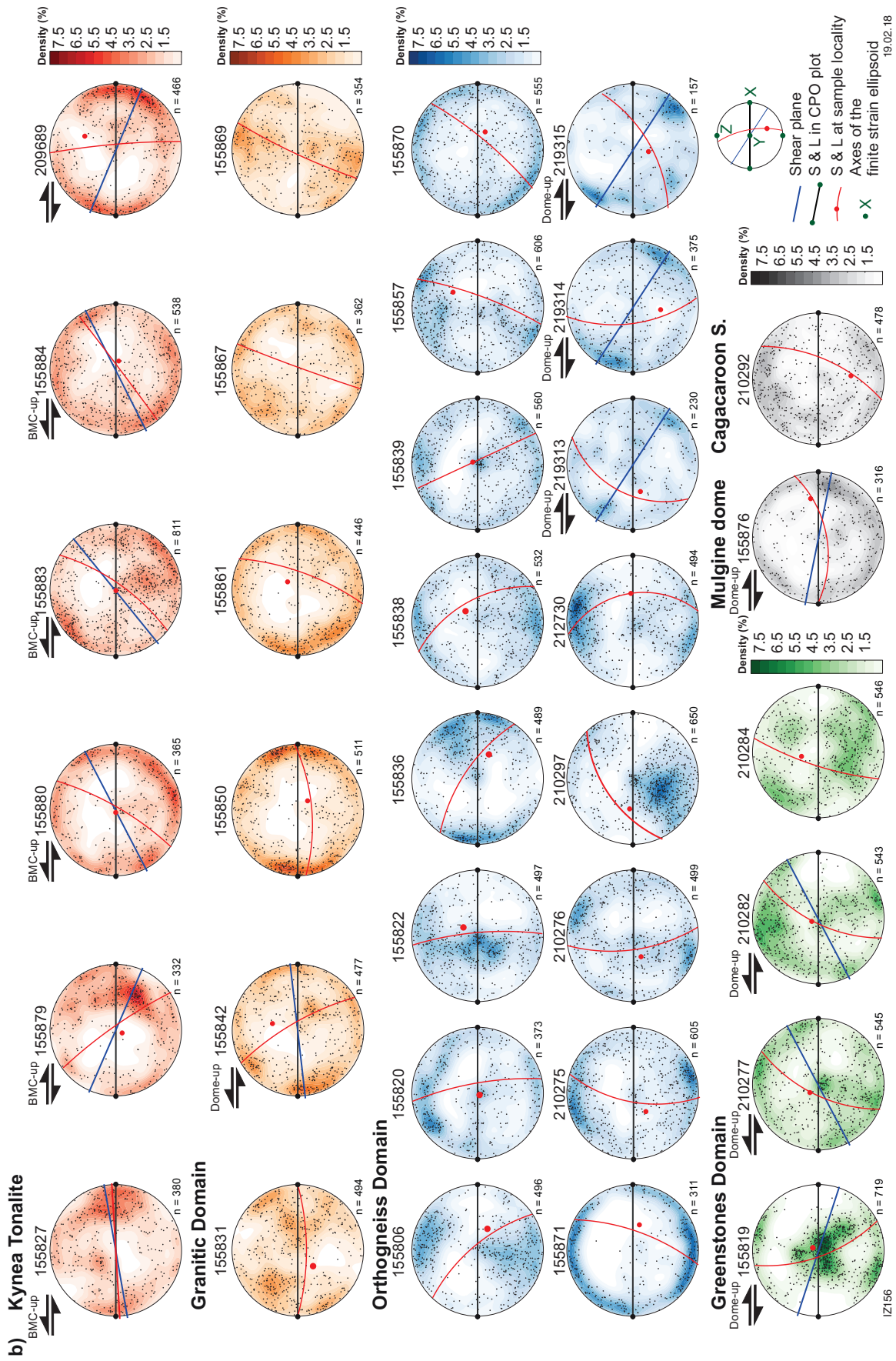


Figure 19. continued

Table 1. Ion microprobe analytical results for zircons from geochronology samples

Group ID	Spot no.	Grain. spot	$^{238}\text{U}$ (ppm)	$^{232}\text{Th}$ (ppm)	$\frac{^{232}\text{Th}}{^{238}\text{U}}$	$f_{204}$ (%)	$^{238}\text{U}/^{206}\text{Pb} \pm 1\sigma$	$^{207}\text{Pb}/^{206}\text{Pb} \pm 1\sigma$	$^{238}\text{U}/^{206}\text{Pb}^* \pm 1\sigma$	$^{207}\text{Pb}^*/^{206}\text{Pb}^* \pm 1\sigma$	$^{238}\text{U}/^{206}\text{Pb}^*$ date (Ma) $\pm 1\sigma$	$^{207}\text{Pb}^*/^{206}\text{Pb}^*$ date (Ma) $\pm 1\sigma$	Disc. (%)
<b>GSWA 209689: metatonalite</b>													
I	6	4.1	14	2	0.12	0.449	2.115 0.086	0.21135	0.01584	0.20735 0.01608	2487	2885 126	13.8
I	19	14.1	340	121	0.37	0.363	1.990 0.029	0.21494	0.00093	0.21171 0.00108	2617	2919 8	10.3
I	23	18.1	110	51	0.48	-0.042	1.968 0.294	0.21189	0.00174	0.21226 0.00176	2650	2923 13	9.3
I	10	6.2	194	114	0.61	0.096	1.793 0.026	0.21410	0.00100	0.21324 0.00104	2855	2930 8	2.6
I	20	15.1	213	105	0.51	0.698	1.877 0.030	0.22048	0.00448	0.21428 0.00461	2737	2938 35	6.8
I	4	2.2	529	9	0.02	0.534	1.912 0.022	0.21925	0.00072	0.21451 0.00090	2700	2940 7	8.2
I	1	1.1	84	49	0.60	0.469	1.922 0.035	0.21903	0.00683	0.21487 0.00693	2690	2943 52	8.6
I	15	10.1	161	81	0.52	0.294	2.012 0.033	0.21756	0.00121	0.21495 0.00135	2595	2943 10	11.8
I	3	2.1	88	52	0.61	0.065	1.813 0.033	0.21609	0.00142	0.21551 0.00146	2831	2947 11	4.0
I	18	13.1	154	72	0.48	0.196	1.769 0.030	0.21757	0.00120	0.21583 0.00129	2884	2950 10	2.2
I	16	11.1	127	71	0.58	0.094	1.732 0.030	0.21704	0.00126	0.21620 0.00130	2936	2953 10	0.6
I	22	17.1	143	93	0.68	0.061	1.745 0.031	0.21722	0.00124	0.21668 0.00127	2919	2956 9	1.3
I	13	9.1	62	30	0.50	0.326	1.775 0.037	0.21960	0.00177	0.21671 0.00200	2873	2956 15	2.8
I	21	16.1	140	105	0.77	0.341	1.796 0.032	0.22050	0.00128	0.21747 0.00144	2845	2962 11	3.9
I	11	7.1	184	143	0.80	0.147	1.733 0.025	0.21968	0.00100	0.21838 0.00106	2934	2969 8	1.2
P	5	3.1	16	1	0.05	0.144	1.766 0.071	0.20515	0.00351	0.20386 0.00374	2890	2857 30	-1.1
D	14	3.2	4	2	0.43	21.056	6.114 0.432	0.30716	0.01037	0.12242 0.04721	783	1992 686	60.7
D	17	12.1	317	175	0.57	0.489	5.551 9.572	0.17660	0.13405	0.17223 0.13509	1063	2579 1310	58.8
D	2	1.2	32	4	0.12	4.044	7.442 0.202	0.22380	0.00421	0.18774 0.00914	782	2722 80	71.3
D	8	5.1	34	10	0.30	20.110	3.717 0.096	0.38391	0.00415	0.20533 0.01604	1255	2869 127	56.3
D	12	8.1	152	77	0.52	2.805	2.424 0.036	0.23377	0.00130	0.20883 0.00250	2173	2896 19	25.0
D	7	4.2	27	13	0.49	1.013	4.171 0.129	0.22410	0.00410	0.21511 0.00556	1373	2944 42	53.4
D	9	6.1	48	10	0.21	6.649	8.549 0.206	0.28407	0.00453	0.22520 0.01240	668	3018 88	77.9
<b>GSWA 214324: metamonzogranite dyke</b>													
I	13	13.1	73	29	0.42	0.000	1.895 0.032	0.18444	0.00561	0.18444 0.00561	2732	2693 50	-1.4
I	4	4.1	140	71	0.52	0.104	1.924 0.024	0.18570	0.00105	0.18477 0.00110	2696	2696 10	0.0
I	18	18.1	311	234	0.78	0.362	1.953 0.019	0.18808	0.00083	0.18484 0.00100	2658	2697 9	1.4
I	2	2.1	111	56	0.52	0.035	1.986 0.027	0.18519	0.00119	0.18487 0.00121	2628	2697 11	2.6
I	17	17.1	342	258	0.78	-0.007	1.918 0.019	0.18506	0.00079	0.18512 0.00080	2705	2699 7	-0.2
I	7	7.1	92	44	0.50	-0.047	1.984 0.030	0.18473	0.00135	0.18515 0.00139	2632	2700 12	2.5
I	11	11.1	120	68	0.59	0.035	1.925 0.026	0.18579	0.00119	0.18547 0.00121	2696	2702 11	0.2
I	15	15.1	135	62	0.47	0.036	1.944 0.026	0.18630	0.00121	0.18598 0.00123	2674	2707 11	1.2
I	8	8.1	166	49	0.30	-0.028	1.976 0.024	0.18599	0.00113	0.18624 0.00114	2640	2709 10	2.5
I	16	16.1	293	129	0.45	0.069	1.994 0.020	0.18693	0.00084	0.18632 0.00087	2619	2710 8	3.4



Table 1. continued

Group ID	Spot no.	Grain. spot	<sup>238</sup> U (ppm)	<sup>232</sup> Th (ppm)	<sup>232</sup> Th/ <sup>238</sup> U	f <sub>204</sub> (%)	<sup>238</sup> U/ <sup>206</sup> Pb ± 1σ	<sup>207</sup> Pb/ <sup>206</sup> Pb ± 1σ	<sup>238</sup> U/ <sup>206</sup> Pb* ± 1σ	<sup>207</sup> Pb*/ <sup>206</sup> Pb* ± 1σ	<sup>238</sup> U/ <sup>206</sup> Pb* date (Ma) ± 1σ	<sup>207</sup> Pb*/ <sup>206</sup> Pb* date (Ma) ± 1σ	Disc. (%)
I	14	14.1	111	52	0.48	-0.063	1.934 0.027	0.18590 0.00129	1.933 0.027	0.18646 0.00133	2688	2711 12	0.8
I	12	12.1	146	69	0.49	0.015	1.960 0.025	0.18730 0.00112	1.960 0.025	0.18716 0.00113	2658	2717 10	2.2
I	1	1.1	111	48	0.45	-0.109	1.959 0.026	0.18637 0.00121	1.957 0.026	0.18735 0.00127	2661	2719 11	2.1
X	5	5.1	134	67	0.52	0.134	1.654 0.022	0.21611 0.00119	1.657 0.022	0.21491 0.00125	3045	2943 9	-3.5
D	6	6.1	59	19	0.33	0.140	1.805 0.034	0.18675 0.00164	1.807 0.034	0.18550 0.00176	2839	2703 16	-5.0
D	9	9.1	95	41	0.44	0.267	2.273 0.033	0.18855 0.00139	2.279 0.033	0.18616 0.00157	2345	2709 14	13.4
D	3	3.1	103	41	0.41	0.158	2.391 0.033	0.18856 0.00136	2.395 0.033	0.18714 0.00147	2250	2717 13	17.2
D	10	10.1	46	28	0.63	0.390	1.926 0.038	0.21546 0.00203	1.934 0.039	0.21198 0.00235	2687	2921 18	8.0
GSWA 214315: metamonzogranite dyke													
I	18	18.1	202	107	0.55	0.068	1.945 0.022	0.18306 0.00098	1.946 0.022	0.18245 0.00101	2673	2675 9	0.1
I	7	7.1	108	53	0.50	0.123	2.025 0.029	0.18382 0.00126	2.028 0.029	0.18272 0.00134	2584	2678 12	3.5
I	12	12.1	134	71	0.54	0.141	1.991 0.025	0.18494 0.00113	1.994 0.025	0.18368 0.00120	2620	2686 11	2.5
I	14	14.1	223	205	0.95	0.099	2.118 0.023	0.18461 0.00097	2.120 0.023	0.18372 0.00101	2491	2687 9	7.3
I	15	15.1	254	187	0.76	0.067	1.963 0.020	0.18468 0.00086	1.965 0.020	0.18409 0.00089	2652	2690 8	1.4
I	11	11.1	273	217	0.82	0.239	1.977 0.020	0.18641 0.00086	1.982 0.020	0.18427 0.00097	2634	2692 9	2.2
I	16	16.1	318	99	0.32	0.063	1.948 0.019	0.18510 0.00455	1.949 0.019	0.18454 0.00456	2670	2694 41	0.9
I	6	6.1	110	186	1.75	0.461	2.037 0.028	0.18969 0.00128	2.047 0.028	0.18556 0.00155	2584	2703 14	5.1
I	1	1.1	375	237	0.65	-0.005	1.946 0.017	0.18568 0.00072	1.946 0.017	0.18573 0.00072	2673	2705 6	1.2
I	8	8.1	71	45	0.65	0.061	2.001 0.033	0.18634 0.00153	2.002 0.033	0.18580 0.00158	2612	2705 14	3.4
I	13	13.1	152	84	0.57	0.014	1.959 0.024	0.18594 0.00107	1.959 0.024	0.18581 0.00108	2659	2705 10	1.7
I	4	4.1	186	105	0.59	0.138	1.958 0.022	0.18706 0.00099	1.961 0.022	0.18583 0.00105	2657	2706 9	1.8
I	2	2.1	198	119	0.62	0.058	1.984 0.021	0.18692 0.00092	1.986 0.021	0.18640 0.00095	2629	2711 8	3.0
I	5	5.1	185	128	0.72	0.251	2.123 0.024	0.18909 0.00101	2.129 0.024	0.18684 0.00112	2482	2715 10	8.6
I	3	3.1	294	94	0.33	0.319	1.985 0.019	0.18981 0.00084	1.991 0.020	0.18695 0.00102	2623	2716 9	3.4
I	17	17.1	122	19	0.16	-0.019	1.916 0.026	0.18690 0.00123	1.916 0.026	0.18707 0.00124	2708	2717 11	0.3
I	9	9.1	142	423	3.08	0.519	2.254 0.028	0.19189 0.00119	2.266 0.028	0.18724 0.00158	2357	2718 14	13.3
X	10	10.1	44	17	0.39	0.853	1.733 0.035	0.22456 0.00203	1.748 0.036	0.21695 0.00264	2916	2958 20	1.4
GSWA 155858: metamonzogranite													
I	1	1.1	345	92	0.27	0.345	1.976 0.024	0.19463 0.00074	1.982 0.024	0.19156 0.00090	2633	2756 8	4.5
I	2	2.1	284	134	0.49	0.934	1.913 0.024	0.19788 0.00080	1.931 0.024	0.18955 0.00119	2690	2738 10	1.8
I	3	3.1	256	240	0.97	0.345	1.915 0.025	0.19575 0.00083	1.922 0.025	0.19267 0.00101	2701	2765 9	2.3
I	4	4.1	63	31	0.51	0.871	1.928 0.041	0.19889 0.00179	1.945 0.042	0.19112 0.00246	2674	2752 21	2.8
I	5	5.1	319	187	0.60	0.245	1.918 0.024	0.19257 0.00078	1.923 0.024	0.19039 0.00087	2700	2746 8	1.7

Table 1. continued

Group ID	Spot no.	Grain. spot	$^{238}\text{U}$ (ppm)	$^{232}\text{Th}$ (ppm)	$\frac{^{232}\text{Th}}{^{238}\text{U}}$	$f_{204}$ (%)	$^{238}\text{U}/^{206}\text{Pb} \pm 1\sigma$	$^{207}\text{Pb}/^{206}\text{Pb} \pm 1\sigma$	$^{238}\text{U}/^{206}\text{Pb}^* \pm 1\sigma$	$^{207}\text{Pb}^*/^{206}\text{Pb}^* \pm 1\sigma$	$^{238}\text{U}/^{206}\text{Pb}^* \text{ date (Ma)} \pm 1\sigma$	$^{207}\text{Pb}^*/^{206}\text{Pb}^* \text{ date (Ma)} \pm 1\sigma$	Disc. (%)
<b>GSWA 214101: monzogranite gneiss</b>													
I	9	9.1	785	174	0.23	0.091	1.985 0.033	0.19136 0.00046	1.987 0.033	0.19055 0.00048	2628	2747 4	4.3
I	5	5.1	492	91	0.19	0.126	1.894 0.032	0.19203 0.00066	1.896 0.032	0.19090 0.00070	2730	2750 6	0.7
I	6	6.1	524	198	0.39	0.029	1.888 0.031	0.19147 0.00050	1.889 0.031	0.19121 0.00051	2739	2753 4	0.5
I	12	12.1	799	107	0.14	0.015	1.876 0.031	0.19154 0.00047	1.876 0.031	0.19140 0.00047	2754	2754 4	0.0
I	2	2.1	495	105	0.22	0.049	1.895 0.031	0.19206 0.00053	1.896 0.031	0.19162 0.00054	2731	2756 5	0.9
I	11	11.1	535	97	0.19	0.099	1.936 0.033	0.19259 0.00055	1.938 0.033	0.19170 0.00059	2682	2757 5	2.7
I	3	3.1	391	61	0.16	0.041	1.982 0.035	0.19217 0.00060	1.983 0.035	0.19180 0.00062	2632	2758 5	4.6
I	1	1.1	539	95	0.18	0.020	1.911 0.053	0.19233 0.00051	1.912 0.053	0.19216 0.00051	2712	2761 4	1.7
I	10	10.1	389	61	0.16	0.015	1.953 0.034	0.19231 0.00064	1.954 0.034	0.19218 0.00065	2665	2761 6	3.5
I	13	13.1	678	100	0.15	-0.029	1.853 0.031	0.19203 0.00052	1.853 0.031	0.19229 0.00053	2782	2762 4	-0.7
I	4	4.1	676	129	0.20	0.017	1.827 0.061	0.19271 0.00047	1.827 0.061	0.19256 0.00047	2814	2764 4	-1.8
I	8	8.1	786	222	0.29	0.047	1.839 0.031	0.19412 0.00044	1.840 0.031	0.19370 0.00045	2798	2774 4	-0.9
D	7	7.1	1528	1700	1.15	0.074	2.746 0.044	0.15247 0.00029	2.748 0.044	0.15181 0.00032	2000	2366 4	15.5
<b>GSWA 214138: granodiorite gneiss</b>													
I	11	1.2	272	96	0.36	0.374	1.898 0.034	0.19504 0.00079	1.905 0.034	0.19170 0.00097	2720	2757 8	1.3
I	2	2.1	527	92	0.18	0.108	1.882 0.031	0.19291 0.00053	1.884 0.031	0.19195 0.00055	2745	2759 5	0.5
I	8	7.1	231	251	1.12	0.069	1.882 0.033	0.19288 0.00082	1.883 0.033	0.19226 0.00085	2746	2762 7	0.6
I	3	3.1	235	81	0.36	0.131	1.900 0.033	0.19348 0.00078	1.902 0.033	0.19231 0.00083	2724	2762 7	1.4
I	10	9.1	321	111	0.36	0.181	1.930 0.034	0.19410 0.00071	1.934 0.034	0.19248 0.00078	2687	2763 7	2.8
I	6	5.1	281	109	0.40	0.264	1.926 0.033	0.19483 0.00073	1.931 0.033	0.19248 0.00089	2690	2763 8	2.7
I	9	8.1	303	94	0.32	0.287	1.916 0.033	0.19535 0.00075	1.922 0.033	0.19279 0.00091	2700	2766 8	2.4
I	7	6.1	229	112	0.51	0.257	1.918 0.034	0.19521 0.00078	1.923 0.034	0.19292 0.00093	2700	2767 8	2.4
I	5	4.1	275	102	0.38	0.249	1.911 0.033	0.19544 0.00072	1.916 0.033	0.19322 0.00083	2707	2770 7	2.3
X	4	3.2	152	69	0.47	0.579	1.942 0.037	0.19989 0.00113	1.953 0.037	0.19473 0.00151	2665	2783 13	4.2
X	1	1.1	198	137	0.72	-0.107	1.899 0.034	0.19399 0.00084	1.897 0.034	0.19495 0.00088	2730	2784 7	2.0
<b>GSWA 214139: monzogranite gneiss</b>													
I	11	11.1	908	255	0.29	0.097	1.898 0.031	0.19078 0.00203	1.900 0.032	0.18992 0.00204	2726	2741 18	0.6
I	4	4.1	406	29	0.07	0.005	1.872 0.032	0.19146 0.00063	1.872 0.032	0.19142 0.00063	2760	2754 5	-0.2
I	1	1.1	401	92	0.24	-0.030	1.894 0.100	0.19153 0.00064	1.894 0.100	0.19180 0.00065	2733	2758 6	0.9
I	2	2.1	289	55	0.20	0.000	1.886 0.033	0.19201 0.00071	1.886 0.033	0.19201 0.00071	2743	2759 6	0.6
I	7	7.1	511	84	0.17	0.106	1.967 0.033	0.19313 0.00056	1.970 0.033	0.19219 0.00059	2647	2761 5	4.1
I	6	6.1	365	66	0.19	0.022	1.892 0.032	0.19242 0.00065	1.892 0.032	0.19223 0.00065	2735	2761 6	1.0

Table 1. continued

Group ID	Spot no.	Grain. spot	<sup>238</sup> U (ppm)	<sup>232</sup> Th (ppm)	<sup>232</sup> Th/ <sup>238</sup> U	f <sub>204</sub> (%)	<sup>238</sup> U/ <sup>206</sup> Pb ± 1σ	<sup>207</sup> Pb/ <sup>206</sup> Pb ± 1σ	<sup>238</sup> U/ <sup>206</sup> Pb* ± 1σ	<sup>207</sup> Pb*/ <sup>206</sup> Pb* ± 1σ	<sup>238</sup> U/ <sup>206</sup> Pb* date (Ma) ± 1σ	<sup>207</sup> Pb*/ <sup>206</sup> Pb* date (Ma) ± 1σ	Disc. (%)
I	10	10.1	205	112	0.56	0.184	1.998 0.037	0.19394 0.00094	2.002 0.037	0.19230 0.00102	2612 40	2762 9	5.4
I	3	3.1	329	68	0.21	0.016	1.903 0.033	0.19264 0.00065	1.904 0.033	0.19249 0.00066	2722 39	2764 6	1.5
I	9	9.1	493	93	0.20	0.036	1.895 0.032	0.19322 0.00057	1.896 0.032	0.19290 0.00058	2731 38	2767 5	1.3
I	8	8.1	743	194	0.27	0.115	1.912 0.032	0.19415 0.00046	1.914 0.032	0.19312 0.00177	2710 38	2769 15	2.1
P	12	12.1	336	78	0.24	0.012	1.975 0.034	0.18994 0.00068	1.975 0.034	0.18984 0.00068	2640 38	2741 6	3.7
P	5	5.1	812	239	0.30	0.048	1.900 0.031	0.19102 0.00042	1.901 0.031	0.19060 0.00043	2725 37	2747 4	0.8
<b>GSWA 211101: volcaniclastic metasilstone</b>													
Y	20	20.1	473	266	0.58	0.052	1.840 0.036	0.19094 0.00052	1.841 0.036	0.19048 0.00053	2797 45	2746 5	-1.8
S	3	3.1	197	90	0.47	0.072	1.943 0.040	0.19169 0.00084	1.945 0.040	0.19105 0.00087	2674 46	2751 8	2.8
S	1	1.1	196	49	0.26	0.089	1.859 0.038	0.19208 0.00320	1.860 0.038	0.19129 0.00321	2773 47	2753 28	-0.7
S	9	9.1	429	160	0.39	0.000	1.841 0.036	0.19157 0.00058	1.841 0.036	0.19157 0.00058	2797 45	2756 5	-1.5
S	33	33.1	322	137	0.44	0.114	1.900 0.037	0.19265 0.00274	1.903 0.038	0.19164 0.00275	2723 45	2756 24	1.2
S	26	26.1	338	154	0.47	0.085	1.963 0.039	0.19260 0.00058	1.965 0.039	0.19184 0.00061	2652 43	2758 5	3.8
S	19	19.1	469	231	0.51	0.074	1.866 0.037	0.19271 0.00288	1.867 0.037	0.19205 0.00288	2765 45	2760 25	-0.2
S	17	17.1	255	61	0.25	0.042	1.841 0.037	0.19260 0.00074	1.841 0.037	0.19223 0.00076	2796 46	2761 6	-1.3
S	32	32.1	389	137	0.36	0.070	1.873 0.037	0.19292 0.00052	1.874 0.037	0.19230 0.00054	2756 45	2762 5	0.2
S	28	28.1	187	54	0.30	0.022	1.912 0.039	0.19261 0.00076	1.913 0.039	0.19241 0.00077	2711 46	2763 7	1.9
S	11	11.1	332	149	0.46	0.120	1.894 0.037	0.19392 0.00061	1.896 0.037	0.19285 0.00065	2731 45	2767 5	1.3
S	22	22.1	268	188	0.72	0.017	1.867 0.037	0.19302 0.00067	1.868 0.037	0.19287 0.00067	2764 46	2767 6	0.1
S	34	34.1	299	102	0.35	0.932	1.937 0.038	0.20165 0.00305	1.956 0.039	0.19334 0.00316	2662 44	2771 27	3.9
S	13	13.1	177	85	0.50	0.094	1.928 0.039	0.19432 0.00081	1.929 0.040	0.19348 0.00084	2692 46	2772 7	2.9
S	18	18.1	361	197	0.56	0.155	1.836 0.036	0.19555 0.00064	1.839 0.036	0.19417 0.00069	2800 46	2778 6	-0.8
S	30	30.1	135	54	0.41	0.083	1.802 0.038	0.21360 0.00093	1.804 0.038	0.21287 0.00096	2843 49	2927 7	2.9
S	21	21.1	180	113	0.65	0.104	1.772 0.036	0.21389 0.00087	1.774 0.036	0.21296 0.00091	2882 48	2928 7	1.6
S	2	2.1	84	52	0.64	0.000	1.773 0.040	0.21571 0.00127	1.773 0.040	0.21571 0.00127	2883 53	2949 10	2.2
S	23	23.1	82	47	0.59	0.091	1.745 0.040	0.21710 0.00133	1.747 0.040	0.21629 0.00138	2918 55	2953 10	1.2
Z	44	16.2	96	40	0.43	0.283	2.086 0.041	0.17820 0.00158	2.092 0.041	0.17567 0.00182	2519 41	2612 17	3.6
Z	43	10.2	268	203	0.78	0.056	1.993 0.030	0.17699 0.00091	1.994 0.030	0.17649 0.00094	2621 33	2620 9	0.0
Z	10	10.1	244	175	0.74	0.030	1.908 0.039	0.17758 0.00071	1.909 0.039	0.17732 0.00073	2716 46	2628 7	-3.3
Z	16	16.1	217	112	0.53	0.170	1.949 0.040	0.17893 0.00084	1.952 0.040	0.17741 0.00092	2666 46	2629 9	-1.4
Z	12	12.1	433	537	1.28	0.096	2.070 0.040	0.17836 0.00054	2.072 0.040	0.17750 0.00057	2539 42	2630 5	3.5
Z	39	38.1	68	26	0.39	0.095	2.017 0.044	0.17886 0.00186	2.019 0.044	0.17801 0.00196	2593 47	2634 18	1.6
Z	31	31.1	72	62	0.89	0.179	2.005 0.045	0.17976 0.00125	2.009 0.045	0.17817 0.00138	2604 49	2636 13	1.2
Z	14	14.1	158	383	2.50	0.019	2.005 0.041	0.17863 0.00081	2.006 0.041	0.17847 0.00082	2608 45	2639 8	1.2



Table 1. continued

Group ID	Spot no.	Grain. spot	$^{238}\text{U}$ (ppm)	$^{232}\text{Th}$ (ppm)	$\frac{^{232}\text{Th}}{^{238}\text{U}}$	$f_{204}$ (%)	$^{238}\text{U}/^{206}\text{Pb} \pm 1\sigma$	$^{207}\text{Pb}/^{206}\text{Pb} \pm 1\sigma$	$^{238}\text{U}/^{206}\text{Pb}^* \pm 1\sigma$	$^{207}\text{Pb}^*/^{206}\text{Pb}^* \pm 1\sigma$	$^{238}\text{U}/^{206}\text{Pb}^*$ date (Ma) $\pm 1\sigma$	$^{207}\text{Pb}^*/^{206}\text{Pb}^*$ date (Ma) $\pm 1\sigma$	Disc. (%)
Z	6	6.1	276	232	0.87	0.101	2.002 0.040	0.18333 0.00068	2.004 0.040	0.18243 0.00072	2610 44	2675 6	2.4
Z	45	7.2	257	280	1.13	0.063	1.981 0.031	0.18344 0.00097	1.983 0.031	0.18289 0.00100	2632 35	2679 9	1.7
Z	25	25.1	31	36	1.19	-0.143	2.042 0.055	0.18264 0.00187	2.039 0.055	0.18391 0.00200	2573 58	2688 18	4.3
Z	41	40.1	171	177	1.07	0.054	1.941 0.033	0.18480 0.00116	1.942 0.033	0.18431 0.00120	2678 37	2692 11	0.5
Z	7	7.1	138	143	1.07	-0.049	1.946 0.041	0.18427 0.00095	1.945 0.041	0.18471 0.00097	2674 47	2696 9	0.8
Z	8	8.1	298	94	0.33	0.006	1.931 0.038	0.18520 0.00064	1.931 0.038	0.18515 0.00065	2690 45	2700 6	0.4
Z	35	35.1	85	66	0.80	0.120	1.892 0.040	0.18631 0.00174	1.895 0.040	0.18524 0.00185	2732 47	2700 17	-1.2
Z	40	39.1	318	501	1.63	0.067	2.002 0.030	0.18693 0.00086	2.004 0.030	0.18633 0.00089	2610 32	2710 8	3.7
Z	24	24.1	159	326	2.11	0.433	1.953 0.041	0.19076 0.00097	1.962 0.041	0.18690 0.00123	2656 46	2715 11	2.2
D	38	37.1	710	343	0.50	0.148	2.798 0.038	0.17209 0.00062	2.802 0.038	0.17077 0.00068	1967 23	2565 7	23.3
D	42	12.2	632	811	1.33	0.224	2.341 0.032	0.17807 0.00069	2.347 0.032	0.17607 0.00079	2288 27	2616 7	12.5
D	36	14.2	192	375	2.02	0.217	2.168 0.036	0.18047 0.00114	2.172 0.036	0.17853 0.00127	2441 34	2639 12	7.5
D	27	27.1	672	459	0.70	0.072	2.089 0.040	0.18426 0.00039	2.090 0.040	0.18362 0.00041	2520 41	2686 4	6.2
D	37	36.1	261	121	0.48	0.155	2.459 0.038	0.18576 0.00105	2.462 0.038	0.18438 0.00113	2197 29	2693 10	18.4
D	4	4.1	218	213	1.01	0.195	2.121 0.043	0.18704 0.00078	2.125 0.043	0.18529 0.00086	2486 43	2701 8	7.9
D	5	5.1	339	889	2.71	0.196	2.229 0.044	0.19079 0.00065	2.233 0.044	0.18905 0.00075	2386 40	2734 7	12.7
D	15	15.1	723	368	0.53	-0.066	1.632 0.139	0.19155 0.00104	1.631 0.139	0.19214 0.00107	3083 225	2761 9	-11.7
D	29	29.1	178	61	0.36	0.271	1.980 0.040	0.19567 0.00081	1.985 0.041	0.19326 0.00095	2630 45	2770 8	5.1

## NOTES:

1. Group ID: I, magmatic zircon; X, xenocrystic zircon; P, radiogenic-Pb loss; Y, youngest detrital zircon; S, older detrital zircons; Z, possible hydrothermal zircon; D, discarded data (discordant or high common Pb)
2. Spot no.: order in which the analyses were obtained
3. Grain spot: the first number is the grain number; the second number is the number of the spot on that grain
4.  $f_{204}$ : proportion of common  $^{206}\text{Pb}$  in measured  $^{206}\text{Pb}$ , determined using measured  $^{206}\text{Pb}/^{206}\text{Pb}$  and contemporaneous common Pb composition (Stacey and Kramers, 1975)
5. Pb\* indicates radiogenic Pb (i.e. corrected for common Pb)
6. Disc. is apparent discordance, as  $D (\%) = 100 \times ([^{207}\text{Pb}/^{206}\text{Pb}^* \text{ date}] - [^{207}\text{Pb}/^{206}\text{Pb}^* \text{ date}]) / [^{207}\text{Pb}/^{206}\text{Pb}^* \text{ date}]$

Table 2. Geochronology samples and results

Sample ID	Rock type	Rock unit	Easting (m)	Northing (m)	1:100 000 Map sheet	Emplacement age (Ma)	Inheritance age (Ma)	Tectonic position (c.f. section 3)
209689	metatallite	Bunnawarra Suite	467506	6823586	BADJA	2960 $\pm$ 10		3.1
214324	metamonzogranite dyke	Big Bell Suite				2705 $\pm$ 6	2943 $\pm$ 9	3.1
214315	metamonzogranite dyke	Big Bell Suite				2700 $\pm$ 7	2958 $\pm$ 20	3.1
155858	metamonzogranite	Rothsay Suite			BADJA	2752 $\pm$ 13		3.2
214101	monzogranite gneiss	Rothsay Suite				2763 $\pm$ 6		3.3
214138	granodiorite gneiss	Rothsay Suite				2763 $\pm$ 5	2784 $\pm$ 13	3.3
214139	monzogranite gneiss	Rothsay Suite				2761 $\pm$ 4		3.3
211101	volcaniclastic metasilstone	Mougouderra Formation			YALGOO	*2758 $\pm$ 4		3.4 (above unconformity)

NOTES: Location coordinates refer to UTM Zone 50. Age uncertainties are 95% confidence intervals. \* maximum age of deposition

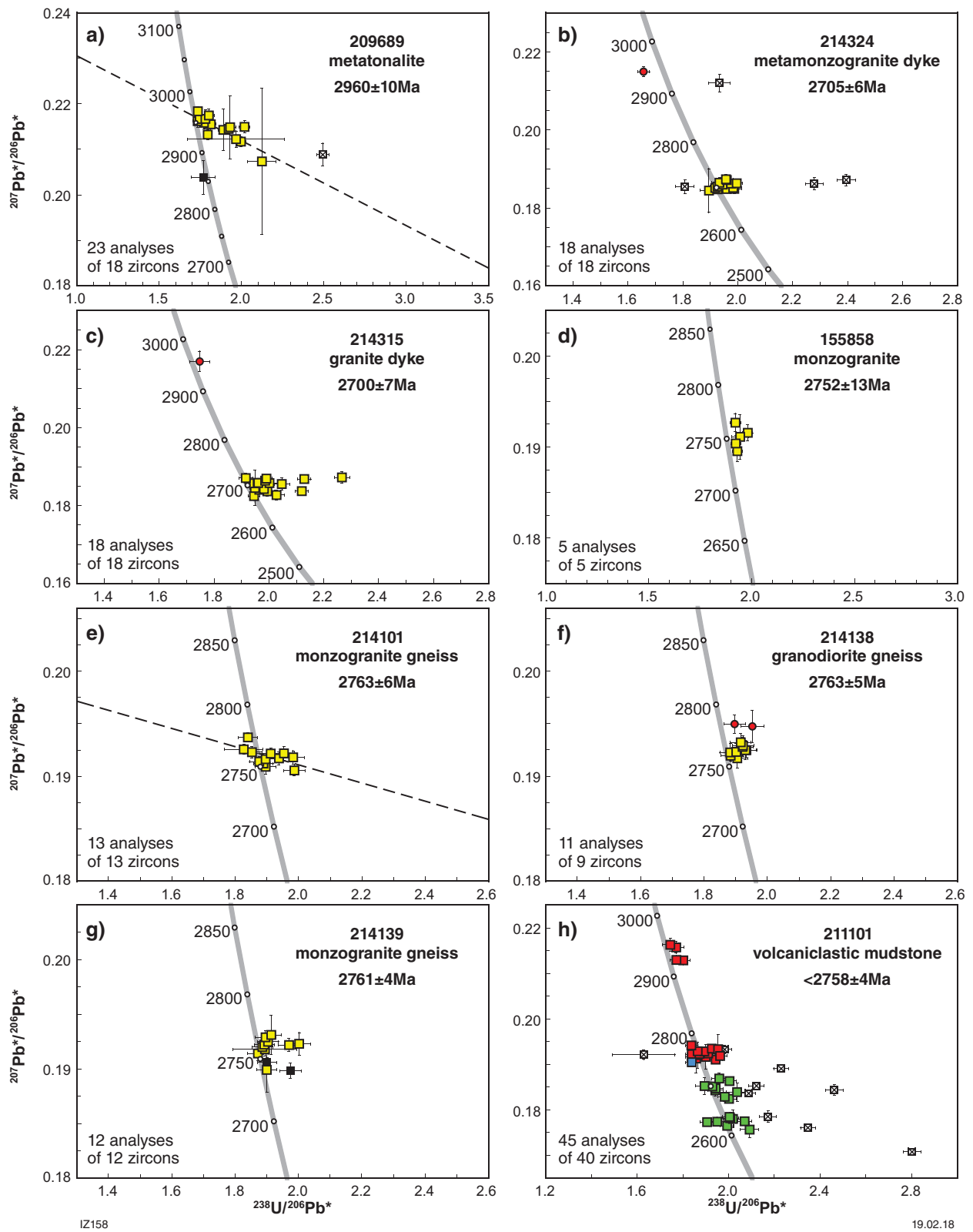


**Figure 20.** U–Pb analytical data for zircons from Yalgoo dome samples. Yellow squares indicate Group I (magmatic zircons); red circles indicate Group X (xenocrystic zircons); black squares indicate Group P (radiogenic-Pb loss); blue square indicates Group Y (youngest detrital zircon); red squares indicate Group S (older detrital zircons); green squares indicate Group Z (possible hydrothermal zircons); crossed squares indicate Group D (discordance >5%). In a) and e), some highly discordant data in Group D are not shown; dashed lines indicate regressions through data in Group I. The date indicated in (h) is a maximum age of sediment deposition of the Mougooderra Formation, lying immediately above the unconformity of the Yalgoo dome (see Fig. 3 for sample location)



Zircons from this sample are colourless to dark brown, and subhedral to euhedral. The crystals are up to 400  $\mu\text{m}$  long, and elongate, with aspect ratios up to 5:1. Concentric zoning is ubiquitous, many crystals contain high-uranium, metamict zones, and some appear to contain older cores. Eleven analyses of nine zircons are concordant to slightly discordant (Fig. 20f). Nine analyses yield a weighted mean  $^{207}\text{Pb}^*/^{206}\text{Pb}^*$  date of  $2763 \pm 5$  Ma (MSWD = 0.34), interpreted as the magmatic crystallization age of the granodiorite protolith. Two analyses of two zircon cores (Table 1), yield a weighted mean  $^{207}\text{Pb}^*/^{206}\text{Pb}^*$  date of  $2784 \pm 13$  Ma (MSWD = 0.02), interpreted as the age of an inherited component.

### GSWA 214139: monzogranite gneiss

This sample of coarse-grained, porphyritic monzogranite gneiss consists of about 30% plagioclase, 30% quartz, 30% K-feldspar, 5% biotite, and accessory opaque minerals, epidote, apatite and zircon. K-feldspar porphyroclasts are up to 2 cm in size and wrapped by elongate trails of biotite and quartz ribbons, defining the metamorphic foliation. Strain-induced myrmekites commonly occur along K-feldspar margins parallel to the foliation. Microstructures indicate that the main fabric developed under mid- to low-amphibolite facies conditions.

Zircons from this sample are colourless to dark brown, and subhedral to euhedral. The crystals are up to 500  $\mu\text{m}$  long, and elongate, with aspect ratios up to 5:1. Concentric zoning is ubiquitous, and many crystals contain high-uranium, metamict zones. Twelve analyses of 12 zircons are concordant to slightly discordant (Fig. 20g). Ten analyses yield a weighted mean  $^{207}\text{Pb}^*/^{206}\text{Pb}^*$  date of  $2761 \pm 4$  Ma (MSWD = 0.57), interpreted as the magmatic crystallization age of the monzogranite protolith. Two analyses yield  $^{207}\text{Pb}^*/^{206}\text{Pb}^*$  dates ( $1\sigma$ ) of  $2741 \pm 6$  and  $2747 \pm 4$  Ma, interpreted to reflect minor ancient loss of radiogenic Pb.

### GSWA 211101: volcaniclastic metasilstone

The sample is a volcaniclastic mudstone, consisting of about 90% quartzofeldspathic groundmass, 2–3% plagioclase, 2–3% secondary sericite and muscovite, 2% quartz, 2% iron oxide minerals, 1% chlorite, and accessory hematite, limonite and zircon. The quartzofeldspathic material varies from microcrystalline to 0.1 mm in grain size, and is interpreted as originally mud or silt. Within this fine-grained material, crystals and fragments of plagioclase are up to 1 mm long; some are single crystals whereas others form small aggregates. Primary quartz is up to 0.5 mm across. Secondary sericite and coarser grained muscovite, together with patches and lenses of granoblastic quartz (0.05 to 0.2 mm in size) and a smaller amount of chlorite–smectite, are associated with plagioclase aggregates and are typically iron-stained by orange–brown hematite and limonite.

Zircons from this sample are colourless to dark brown, and mainly subhedral to euhedral. The crystals are up to 300  $\mu\text{m}$  long, and equant to elongate, with aspect ratios up to 4:1. In CL images, concentric zoning is ubiquitous, and many crystals contain high-uranium, metamict domains.

Some anhedral crystals are highly luminescent in CL images. Forty-five analyses of 40 zircons are concordant to strongly discordant (Fig. 20h). Nine analyses >5% discordant were discarded. Nineteen analyses yield  $^{207}\text{Pb}^*/^{206}\text{Pb}^*$  dates of 2953–2751 Ma. These analyses have moderate Th/U ratios (0.3 – 0.7), and were located in normally luminescent crystals. The youngest analysis indicates a  $^{207}\text{Pb}^*/^{206}\text{Pb}^*$  date of  $2746 \pm 5$  Ma ( $1\sigma$ ), which represents a maximum age of deposition for the volcaniclastic mudstone. A more conservative estimate of the maximum depositional age can be based on the weighted mean  $^{207}\text{Pb}^*/^{206}\text{Pb}^*$  date of  $2758 \pm 4$  Ma (MSWD = 1.15) for the 11 youngest analyses, values very close to those representing the main magmatic event in the Yalgoo dome reflected in samples in Fig. 20a,c–g.

Seventeen analyses, located mainly in highly luminescent crystals with highly variable Th/U ratios (0.3 – 2.5), yield  $^{207}\text{Pb}^*/^{206}\text{Pb}^*$  dates of 2715–2612 Ma. These dates are significantly younger than is expected for this rock based on geological mapping observations (i.e. the Mougooderra Formation is deformed in the footwall of the c. 2700 Ma Mulloo thrust [Figs 2, 3, 8]), and include age components at c. 2700, 2679 and 2629 Ma, tentatively interpreted as the ages of hydrothermal events.

## Discussion and conclusion

The Kynea Tonalite shows a prominent planar fabric ( $S_{1-2}$ ) of variable orientation (i] in Fig. 4c) that, at least in part, developed under migmatitic conditions (Fig. 5b). Deformation at a high temperature is also suggested by microstructures and quartz CPO fabric (Figs 16a, 19b).  $S_{1-2}$  bears a prominent, subvertical stretching and mineral lineation that is subparallel to the axis of isoclinal and sheath folds, which are visible from the map to the outcrop scale (Figs 4b, 5e, respectively; see also Fenwick, 2014). Therefore, the  $D_{1-2}$  event reflects the subvertical flow of the Kynea Tonalite.  $S_{1-2}$  is post-dated by two distinct, north-trending and more localized sets of structures ( $D_3$  and  $D_4$  events).  $D_3$  was associated with the development of north-trending leucosomes (Fig. 5c) that are axial planar to subvertical  $F_3$  folds.  $S_3$  is cut at a low angle by north-trending and steeply east-dipping granite dykes (Fig. 5f) that were in turn reactivated as reverse shear zones. Therefore, both the  $D_3$  and  $D_4$  events likely reflect periods of subhorizontal east–west shortening. The time frame of the tectono-magmatic evolution of the Kynea Tonalite is only partially constrained.  $S_{1-2}$  and  $S_3$  developed between c. 2960 Ma, the time of tonalite crystallization (GSWA sample 209689, Fig. 20a) and c. 2700 Ma, age of the north-trending granitic dykes (GSWA sample 214324, Fig. 20b). The c. 2700 Ma age also represents the maximum age for the  $D_4$  shearing event, which is localized in the granitic dykes.

The evolution of the Kynea Tonalite in the core of the dome needs to be reconciled with structural and geochronological data preserved in Group 1 granitic rocks and in the overlying greenstone cover. Both magmatic and gneissic foliations in the Group 1 granitic rocks ( $S_{\text{MAG}}$  and  $S_{\text{G}}$ , respectively) are subparallel to the elliptical dome margin and are most intense at the granite–greenstone lithological contact (i.e. subparallel to the Badja decollement; Fig. 7c). A similar geometry is also preserved in the greenstone cover (taking into account the effect of the  $F_3$  folds;

Figs 9f, 10). Domal planar fabrics are associated with radial and outwards-plunging linear structures ( $A_1$ – $A_2$  fold axes in greenstones,  $L_G$  in both orthogneiss and greenstones; Figs 7c, 10). Given that the Badja decollement is a high-strain zone with top-outwards sense of shear, it is likely that this structure allowed the emplacement of the granite–migmatite dome into the greenstone cover.

Mesostructures and microstructures indicate that the Badja decollement contains a mainly mid-amphibolite to greenschist retrograde gneissic fabric. However, microstructures and quartz CPO data show that this structure locally retains relics of an older microfabric, developed at near-solidus temperature. This indicates that the onset of shearing along the Badja decollement, and therefore the development of the ‘dome-forming fabric’ occurred during the emplacement of Group 1 granitic rocks, in the 2765–2750 Ma time span (four dated samples, Fig. 20d–g).

The greenstone cover includes at least one unconformity, which is preserved along both the eastern and the western flanks of the Yalgoo dome (Fig. 8a). Outcrop-scale features indicate that the early stages of development of the unconformity reflect uplift, erosion and in situ reworking of the older greenstone sequence (Fig. 8b). Notably, the inferred maximum depositional age of the Mougooderra Formation, which lies above the unconformity (c. 2758 Ma; GSWA sample 211101, Fig. 20h), overlaps with the emplacement age of Group 1 rocks. Furthermore, geochronological data (Figs 20, 21) show that both the age and the Th/U ratios of the main populations of detrital zircons in the metasedimentary GSWA sample 211101 match with the age and the Th/U ratios of the main zircon populations preserved in the c. 2950 Ma metatonalite of the Kynea Tonalite (Bunnawarra Suite) and in the 2760–2750 Ma granitic rocks (Rothsay Suite). These data suggest that the detrital component of the Mougooderra Formation might have been sourced from the rising dome. Overall, these data point to a direct causal relationship between: i) emplacement of Group 1 granitic rocks; ii) uplift during doming and subsequent tilting of the greenstone cover; and iii) erosion of the lower greenstone succession that started with local reworking (Fig. 8b). Given that the Mougooderra Formation is pervasively deformed together with the older greenstone sequence (Fig. 9i), it is likely that the unconformity developed during the early stages of doming.

Structural analysis is a fundamental tool for unravelling the tectonic evolution of gneiss domes (e.g. Brun et al., 1981). Our large structural dataset (1395 foliation and 478 lineation measurements for the Yalgoo dome: Figs 4c, 7c, 10), combined with microstructural data, indicate that doming, associated with outward flow of supracrustal material through normal movement, was accompanied by the emplacement of large volumes of granitic magma at 2765–2750 Ma. The radial pattern of linear structures suggests that, at the scale of the Yalgoo dome, the finite strain pattern was produced by diapiric granite emplacement, with negligible background regional stress field (Yin, 2004). In contrast, magmatic domes formed by interaction between a local stress field (i.e. buoyancy of the dome rocks) and a regional stress field invariably show a unidirectional orientation of lineation (Kruckenberg et al., 2011; Yin, 2004). In the case of the Yalgoo dome, the >8 km-thick, high-density greenstone cover, overlying

felsic and possibly partially molten material probably generated a strong gravitational instability that might have triggered diapirism in conjunction with greenstone sagduction (Francois et al., 2014). The 2765–2750 Ma time span in the Youanmi Terrane is characterized by the emplacement of mafic–ultramafic lava flows interlayered with banded iron-formation (Van Kranendonk et al., 2013), which suggests a period of tectonic quiescence (Zibra et al., 2017).

The subvertical flow recorded by the Kynea Tonalite in the core of the dome ( $D_{1-2}$  stage, Fig. 4c) probably coincided with the 2765–2750 Ma doming stage. Both conceptual models and analogue simulations of rising diapirs indicate that these structures are characterized by upward flow through the middle of the dome, followed by downward flow along the external margins (Cruden, 1990; François et al., 2014; Talbot and Jackson, 1987).

The distribution of different types of tectonites suggests that finite strain varies systematically throughout the Yalgoo dome (Fig. 11), as expected in case of diapir-driven tectonic evolution with peak shearing at the margin of the dome (Cruden, 1990; Weinberg and Podladchikov, 1995; Sullivan, 2013).

The dome-forming fabric in the Yalgoo dome is locally overprinted by a discordant, north-trending foliation that shows a relatively uniform trend over the whole study area. We therefore consider this younger fabric as the expression of the regional tectonic overprint. This is parallel to the prominent north-trending Mulloo thrust (Fig. 14a), the only other significant north-trending feature in the area, which was active during the emplacement of the Lakeside pluton at c. 2700 Ma (Zibra et al., 2014a). This age also corresponds to the maximum age of the  $D_4$  shearing event recorded by the Kynea Tonalite. Thus, the c. 2700 Ma date probably represents the age of the regional tectonic fabric ( $D_3$  and  $D_4$  events), which developed at near-solidus temperatures in the lowermost structural level now exposed in the area (the core of the Yalgoo dome, Fig. 5c) and at low-greenschist conditions within the supracrustal cover sequence (Fig. 18a,b).

Myers and Watkins (1985), based on the 500–1000 m diameter sheath folds in the Kynea Tonalite in the core of the dome, proposed that the Yalgoo dome resulted from a north-trending folding event superposed on an older east-trending, folding event. The data presented in this work indicate that this interpretation is unlikely for the following reasons:

Their model requires the superposition of two generations of upright folds. However, most of the fold-related structures mapped during this work, or deducible from map analysis, show steeply plunging axes (Figs 4c, 7c, 10).

Therefore, the ‘circular structures’ cannot represent dome-and-basin patterns generated by superposed folds, as proposed by Myers and Watkins (1985), as they are post-dated by the north-trending fabric that supposedly generated them. In fact, Fenwick (2014) demonstrated that the circular map pattern results from subvertical sheath folds ( $F_{1-2}$  folds), which are also visible at outcrop scale (Fig. 5e).

The distribution of planar and linear structures and the finite strain patterns at the scale of the Yalgoo dome fit well with

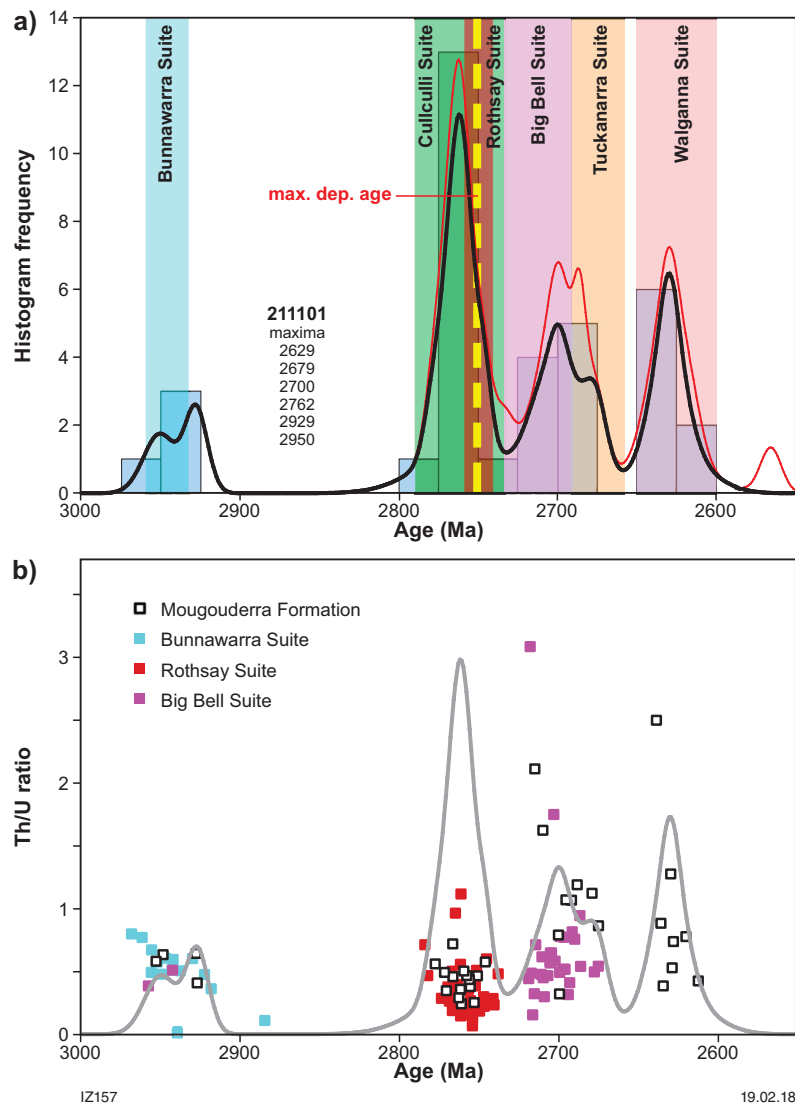


Figure 21. a) Probability density diagram and histogram for sample 211101: volcanoclastic mudstone, Wadgingarra Hill shown in Fig. 20h. Thick curve, maxima values, and frequency histogram (bin width 25 Ma) include only data with discordance <5% (36 analyses of 33 zircons). Thin curve includes all data (45 analyses of 40 zircons); b) Th/U ratio vs age (Ma) for zircons from Mougouderra Formation and Bunnawarra Suite, Rothsay Suite and Big Bell Suite. The grey curve represents the probability density curve from GSWA sample 211101 (corresponding to the black curve shown in Fig. 21a)



a model of diapiric emplacement during doming and cannot be explained by a model of superposed folding events.

An east-trending fabric was mapped during this work. However, this fabric is a local feature and is spatially associated with kilometre-scale greenstone keels (Figs 11, 12). Moreover, the east-trending fabric is demonstrably late and weakly pervasive ( $S_2$  in Fig. 12c) so it does not represent the oldest fabric in the area, as proposed by Myers and Watkins (1985).

The study area preserves a regional-scale, north-trending tectonic fabric (Fig. 14a). However, this fabric post-dates all the dome-forming structures in the area (Figs 14, 15). Therefore, it could not have been responsible for doming, as proposed by Myers and Watkins (1985).

Plutons flanking the Yalgoo dome show a similar, first-order structural architecture. The Mellenbye and the Mt Mulgine domes, and the Cagacaron Syenogranite, show a main tectonic fabric subparallel to the granite–greenstone contact (Fig. 10). The Mellenbye dome shows a first-order domal geometry and the overlying greenstones of the Gullewa greenstone belt show a southeast-trending pervasive tectonic fabric subparallel to dome margins (Fig. 10). However, given that the Mellenbye dome is currently undated, the temporal relationships between its structures and those associated with the adjacent domes are currently unclear.

Despite the lack of systematic structural data from these plutons, geological mapping, complemented by geophysical data, suggests that they show a first-order domal structure. The core of the Mt Mulgine dome preserves a subhorizontal, high-temperature fabric, as indicated by microstructural and quartz CPO data (Figs 13c, 18a, 19b; GSWA sample 155876). This planar fabric is subparallel to the main foliation in host greenstones, which show an outwards-dipping, concentric pattern (Fig. 10). The east-trending contact between the Cagacaron Syenogranite and host greenstones coincides with a pervasive tectonic foliation, associated with steeply plunging direction of tectonic transport (Fig. 13a,b). Both the Mt Mulgine dome and the Cagacaron Syenogranite have crystallization ages that overlap with the age of crystallization of the Yalgoo dome (Figs 3, 20). Therefore, it is likely that the structural framework of the study area resulted primarily from the interference between roughly coeval diapirs.

The significance of the aspect ratio (~2) of the Yalgoo dome is unclear. If the dome developed via a gravitational instability under zero far-field deviatoric stress, then one would expect a dome with a circular section in map view. In this scenario, the present-day aspect ratio could be interpreted as a result of the subsequent east–west shortening event. In this case, one would expect the occurrence of a well-developed, regional north-trending fabric, in apparent contradiction with our field observations (Figs 14, 15). It is possible that the intensity of the regional tectonic fabric is underestimated, particularly in those domains in which the dome-forming fabric is north trending. Alternatively, at least part of the aspect ratio of the Yalgoo dome might represent a primary feature developed during dome emplacement, and could either reflect syn-emplacement north–south extension or east–west shortening.

## Caveats and future studies

This study provides fundamental structural constraints on the evolution of this region. However, these data need to be integrated with data from other Earth Science disciplines. In particular, the time frame of the tectonic evolution described here is only partly constrained. The age of  $D_{1,2}$  and  $D_3$  migmatitic events recorded by the Kynea Tonalite are poorly constrained. Also, geochemical data (Clos et al., 2016) indicate that the Yalgoo dome includes a wide variety of granitic rocks. The emplacement age of these different granite suites should be investigated systematically. Age constraints on the major shearing event along the Badja decollement could be improved by obtaining mica or amphibole cooling ages (e.g. Ar/Ar geochronology). Owing to the difficulty of measuring magmatic lineations, the kinematics of the magmatically foliated granite domains is poorly constrained. AMS studies (e.g. Kruckenberg et al., 2011) focused on these domains would provide important constraints on the tectono-magmatic evolution of the study area. Finally, no metamorphic data are available for the study area and therefore, at present, the amount of vertical displacement related to diapiric activity cannot be estimated.

## Acknowledgements

Formal reviews from Roberto Weinberg and Patrice Rey substantially improved the quality of this paper. The staff of the GSWA laboratory prepared the samples for geochronology; their accurate work is greatly acknowledged. T Zama, P Vota, S Lazar and D Twist provided invaluable support during fieldwork.

## References

- Bouhallier, H, Chardon, D and Choukroune, P 1995, Strain patterns in Archean dome-and-basin structures: The Dharwar craton (Karnataka, South India): *Earth and Planetary Science Letters*, v. 135, no. 1–4, p. 57–75.
- Brun, JP, Gapais, D and Le Theoff, B 1981, The mantled gneiss domes of Kuopio (Finland): Interfering diapirs: *Tectonophysics*, v. 74, no. 3, p. 283–304.
- Cassidy, KF 2006, Geological evolution of the Eastern Yilgarn Craton (EYC), and terrane, domain and fault nomenclature, in *3D Geological Models of the Eastern Yilgarn Craton — Y2 Final Report pmd\*CRC* edited by RS Blewett and AP Hitchman: Geoscience Australia, Record 2006/04, p. 1–19.
- Cassidy, K, Champion, D, McNaughton, N, Fletcher, I, Whitaker, A, Bastrakova, I and Budd, A 2002, Characterisation and metallogenic significance of Archaean granitoids of the Yilgarn Craton, Western Australia: Minerals and Research Institute of Western Australia (MERIWA) Report 222.
- Caudery, JN 2014, Structural evolution of the Yalgoo Dome, Yilgarn Craton, Western Australia: Geological Survey of Western Australia, Record 2014/4, 89p.
- Champion, DC and Cassidy, KF 2002, Granites of the northern Murchison Province: their distribution, age, geochemistry, petrogenesis, relationship with mineralisation, and implications for tectonic environment, in *The characterisation and metallogenic significance of Archaean granitoids of the Yilgarn Craton* edited by KF Cassidy, DC Champion, NJ McNaughton, IR Fletcher, AJ Whitaker, IV Bastrakova and A Budd: Minerals and Energy Research Institute of Western Australia (MERIWA), Project no. M281/AMIRA Project no. 482 (unpublished report no. 222), p. 1–54.

- Champion, DC and Sheraton, JW 1997, Geochemistry and Nd isotope systematics of Archaean granites of the Eastern Goldfields, Yilgarn Craton, Australia: Implications for crustal growth processes: *Precambrian Research*, v. 83, p. 109–132.
- Chen, SF, Riganti, A, Wyche, S, Greenfield, JE and Nelson, DR 2003, Lithostratigraphy and tectonic evolution of contrasting greenstone successions in the central Yilgarn Craton, Western Australia: *Precambrian Research*, v. 127, p. 249–266.
- Clos, F, Zibra, I and Weinberg, RF 2016, 300 Ma of magmatism in the Archean Yalgoo Dome (poster): Geological Survey of Western Australia; GSWA Open Day 2016, Fremantle, Western Australia, 26 February 2016.
- Cruden, AR 1988, Deformation around a rising diapir modeled by creeping flow past a sphere: *Tectonics*, v. 7, no. 5, p. 1091–1101.
- Cruden, AR 1990, Flow and fabric development during the diapiric rise of magma: *The Journal of Geology*, p. 681–698.
- Drummond, BJ, Goleby, BR and Swager, CP 2000, Crustal signature of Late Archean tectonic episodes in the Yilgarn Craton, Western Australia: Evidence from deep seismic sounding: *Tectonophysics*, v. 329, p. 193–221.
- Fenwick, MJ 2014, Structural evolution of the Yalgoo Dome, Yilgarn Craton, Western Australia: a core perspective: Geological Survey of Western Australia, Record 2014/16, 93p.
- Foley, BJ 1997, Reassessment of Archaean tectonics in the Yalgoo District, Murchison Province, Western Australia: Monash University, Melbourne, Australia, BSc thesis, 86p (unpublished).
- François, C, Philippot, P, Rey, P and Rubatto, D 2014, Burial and exhumation during Archean sagduction in the east Pilbara granite-greenstone terrane: *Earth and Planetary Science Letters*, v. 396, p. 235–251.
- Gower, RJW and Simpson, C 1992, Phase boundary mobility in naturally deformed, high-grade quartzofeldspathic rocks: Evidence for diffusional creep: *Journal of Structural Geology*, v. 14, no. 3, p. 301–313.
- Hammes, DM and Peternell, M 2016, FAME: Software for analysing rock microstructures, *Computers and Geosciences*, v. 90, 24–33.
- Ivanic, TJ, Li, J, Meng, Y, Guo, L, Yu, J, Chen, SF, Wyche, S and Zibra, I 2015, Yalgoo, WA Sheet 2241: Geological Survey of Western Australia, 1:100 000 Geological Series.
- Kruckenberger, SC, Vanderhaeghe, O, Ferré, EC, Teyssier, C and Whitney, DL 2011, Flow of partially molten crust and the internal dynamics of a migmatite dome, Naxos, Greece: *Tectonics*, v. 30, no. 3.
- Kruhl, JH 1996, Prism- and basal-plane parallel subgrain boundaries in quartz: A microstructural geothermobarometer: *Journal of Metamorphic Geology*, v. 14, no. 5, p. 581–589.
- Lister, GS 1977, Discussion: crossed-girdle c-axis fabrics in quartzites plastically deformed by plane strain and progressive simple shear: *Tectonophysics*, v. 39 no. 1–3, p. 51–54.
- Ludwig, KR 2003, Isoplot 3.00: a geochronological toolkit for Microsoft Excel: Berkeley Geochronology Centre, Special Publication 4, 70p.
- Mainprice, D, Bouchez, JL, Blumenfeld, P and Tubià, JM 1986, Dominant c slip in naturally deformed quartz: implications for dramatic plastic softening at high temperature: *Geology*, v. 14, no. 10, p. 819–822.
- Morris, PA, Riganti, A and Chen, SF 2007, Evaluating the provenance of Archean sedimentary rocks of the Diemals Formation (central Yilgarn Craton) using whole-rock chemistry and precise U–Pb zircon chronology: *Australian Journal of Earth Sciences*, v. 54, no. 8, p. 1123–1136, doi:10.1080/08120090701615758.
- Myers, JS and Watkins, KP 1985, Origin of granite–greenstone patterns, Yilgarn Block, Western Australia: *Geology*, v. 13, p. 778–780.
- Passchier, CW and Trouw, RAJ 2005, *Microtectonics*, 2nd ed., Springer, Berlin.
- Peternell, M, Hasalová, P, Wilson, C, Piazzolo, S and Schulmann, K 2010, Evaluating quartz crystallographic preferred orientations and the role of deformation partitioning using EBSD and fabric analyser techniques: *Journal of Structural Geology*, v. 32, no. 6, p. 803–817.
- Ramberg, H 1972, Theoretical models of density stratification and diapirism in the Earth: *Journal of Geophysical Research*, v. 77, no. 5, p. 877–889.
- Ramsay, JG 1967, *Folding and fracturing of rocks*: McGraw-Hill International, New York, USA, 568p.
- Ramsay, JG and Huber, MI 1987, *The techniques of modern structural geology, Volume 2: Folds and fractures*: Academic Press, London, UK, 392p.
- Rosenberg, CL 2003, Deformation and recrystallization of plagioclase along a temperature gradient: An example from the Bergell tonalite: *Journal of Structural Geology*, v. 25, no. 3, p. 389–408.
- Sawyer, EW 1999, Criteria for the recognition of partial melting: *Physics and Chemistry of the Earth, Part A: Solid Earth and Geodesy*, v. 24, no. 3, p. 269–279.
- Simpson, C and Wintsch, RP 1989, Evidence for deformation-induced K-feldspar replacement by myrmekite: *Journal of Metamorphic Geology*, v. 7, no. 2, p. 261–275.
- Stacey, JS and Kramers, JD 1975, Approximation of terrestrial lead isotope evolution by a two-stage model: *Earth and Planetary Science Letters*, v. 26, p. 207–221.
- Stern, RA 2001, A new isotopic and trace-element standard for the ion microprobe: preliminary thermal ionization mass spectrometry (TIMS) U–Pb and electron microprobe data: Geological Survey of Canada, Report 2001-F1, 11p.
- Stern, RA, Bodorkos, S, Kamo, SL, Hickman, AH and Corfu, F 2009, Measurement of SIMS instrumental mass fractionation of Pb isotopes during zircon dating: *Geostandards and Geoanalytical Research*, v. 33, p. 145–168.
- Stipp, M, Stünitz, H, Heilbronner, R and Schmid, SM 2002, The eastern Tonale fault zone: a 'natural laboratory' for crystal plastic deformation of quartz over a temperature range from 250 to 700°C: *Journal of Structural Geology*, v. 24, p. 1861–1884.
- Sullivan, WA 2013, L tectonites: *Journal of Structural Geology*, v. 50, p. 161–175.
- Talbot, CJ and Jackson, MPA 1987, Internal kinematics of salt diapirs: *AAPG Bulletin* v. 71, no. 9, p. 1068–1093.
- Tomkins, AE 2015, Tectonite type: their formation and significance, map production, field relationships and petrography: Geological Survey of Western Australia, Record 2015/4, 113p.
- Tullis, J and Yund, RA 1987, Transition from cataclastic flow to dislocation creep of feldspar: mechanisms and microstructures: *Geology*, v. 15, no. 7, p. 606–609.
- Van Kranendonk, MJ, Collins, WJ, Hickman, AH and Pawley, MJ 2004, Critical tests of vertical vs horizontal tectonic models for the Archean East Pilbara Granite–Greenstone Terrane, Pilbara Craton, Western Australia: *Precambrian Research*, v. 131, p. 173–211.
- Van Kranendonk, MJ, Ivanic, TJ, Wingate, MTD, Kirkland, CL and Wyche, S 2013, Long-lived, autochthonous development of the Archean Murchison Domain, and implications for Yilgarn Craton tectonics: *Precambrian Research*, v. 229, p. 49–92.
- Vearncombe, JR 1998, Shear zones, fault networks, and Archaean gold: *Geology*, v. 26, no. 9, p. 855–858, doi:10.1130/0091-7613(1998)026<0855:SZFNAA>2.3.CO;2.
- Watkins, KP and Hickman, AH 1990, Geological evolution and mineralization of the Murchison Province, Western Australia: Geological Survey of Western Australia, Bulletin 137, 267p.
- Weinberg, RF and Podladchikov, YY 1995, The rise of solid-state diapirs: *Journal of Structural Geology*, v. 17, no. 8, p. 1183–1195.

- Whitney, DL, Teyssier, C and Vanderhaeghe, O 2004, Gneiss domes and crustal flow, *in* Gneiss Domes in Orogeny *edited by* DL Whitney, C Teyssier and CS Siddoway: Geological Society of America 380, p. 15–33.
- Wiedenbeck, M and Watkins, KP 1993, A timescale for granitoid emplacement in the Archean Murchison Province, Western Australia, by single zircon geochronology: *Precambrian Research*, v. 61, p. 1–26.
- Wilde, SA, Middleton, MF and Evans, BJ 1996, Terrane accretion in the southwestern Yilgarn Craton: evidence from a deep seismic crustal profile: *Precambrian Research*, v. 78, p. 179–196.
- Wingate, MTD, Kirkland, CL and Ivanic, TJ 2014, 207630: porphyritic monzogranite, Garden Pool Well; Geochronology Record 1215: Geological Survey of Western Australia, 4p.
- Wingate, MTD, Kirkland, CL and Zibra, I 2015, 155879: granodiorite gneiss, Toben Bore; Geochronology Record 1245: Geological Survey of Western Australia, 4p.
- Wyche, S, Fiorentini, M, Miller, JL and McCuaig, TC 2012, Geology and controls on mineralisation in the Eastern Goldfields region, Yilgarn Craton, Western Australia: *Episodes*, v. 35, no. 1, p. 273–282.
- Yin, A 2004, Gneiss domes and gneiss dome systems: *Geological Society of America Special Papers*, v. 380, p. 1–14.
- Zibra, I, Clos, F, Weinberg, RF and Peternell, M 2017, The c. 2730 Ma onset of the Neoproterozoic Yilgarn orogeny: *Tectonics*, doi:org/10.1002/2017TC004562.
- Zibra, I, Gessner, K, Smithies, RH and Peternell, M 2014a, On shearing, magmatism and regional deformation in Neoproterozoic granite–greenstone systems: Insights from the Yilgarn Craton: *Journal of Structural Geology*, v. 67, p. 253–267.
- Zibra, I, Kruhl, J and Braga, R 2010, Late Palaeozoic deformation of post-Variscan lower crust: shear zone widening due to strain localization during retrograde shearing, *International Journal of Earth Sciences*, v. 99, p. 973–991.
- Zibra, I, Kruhl, JH, Montanini, A and Tribuzio, R 2012, Shearing of magma along a high-grade shear zone: Evolution of microstructures during the transition from magmatic to solid-state flow: *Journal of Structural Geology*, v. 37, p. 150–160.
- Zibra, I, Smithies, RH, Wingate, MTD and Kirkland, CL 2014b, Incremental pluton emplacement during inclined transpression: *Tectonophysics*, v. 623, p. 100–122, doi:10.1016/j.tecto.2014.03.020.